Surface temperature and the dynamics of H2 on Cu(111)
Smits, B.

Citation

Smits, B. (2023, July 4). *Surface temperature and the dynamics of H2 on Cu(111)*. Retrieved from https://hdl.handle.net/1887/3628423

Version:	Publisher's Version
License:	[Licence agreement concerning inclusion of doctoral thesis in the Institutional Repository of the University of Leiden](#)
Downloaded from:	https://hdl.handle.net/1887/3628423

Note: To cite this publication please use the final published version (if applicable).

Surface temperature and the dynamics of H$_2$ on Cu(111)

Proefschrift

ter verkrijging van
de graad van doctor aan de Universiteit Leiden,
op gezag van rector magnificus prof.dr.ir. H. Bijl,
volgens besluit van het college voor promoties
te verdedigen op dinsdag 4 juli 2023
klokke 11:15 uur

door

Bauke Smits
geboren te Zuidland
in 1994

Promotor: Prof.dr. G.-J. Kroes

Co-promotor: Dr. M.F. Somers

Promotiecommissie:

Prof.dr. M. Ubbink

Prof.dr. S.A. Bonnet

Prof.em.dr. M.C. van Hemert

Dr. A.L.M. Lamberts

Prof.dr. G.N. Alexandrowicz   (Swansea University)

Prof.dr. D.A. Auerbach   (Max Planck Institute for Biophysical Chemistry)

Contents

Chapter **1**

Introduction

1.1 Heterogeneous catalysis

Through their modification of reaction pathways, catalysts are one of the cornerstones of life as we know it and are found in many shapes and sizes[1]. Be it in outer space, where we might find the origins of complex molecules on grains of dust[2], or inside a living cell, where complex organic structures push energetically unfavourable reactions towards products that sustain life[3]. Humanity has similarly employed catalysis and bends it to its own use through its widespread applications in industrial processes[4]. For example with steam reforming we are able to use methane and water to produce the hydrogen molecule, a process which under normal conditions is highly endothermic, i.e., costs a large amount of energy. This hydrogen can then be employed in the Haber-Bosch process, where it reacts with the inert nitrogen molecule to produce the very useful ammonia molecule[5]. We have also found ways of directly harvesting the energy out of these generated hydrogen molecules, converting the hydrogen back to water. Again catalysts are employed to aid in harvesting of the released energy for a large variety of applications[6]. What these applications all have in common is that while the reactant molecules are gaseous, or perhaps liquid, the catalysts are often (metallic) solids. This subtype of catalysis - heterogeneous catalysis, where the catalyst and the reactants exist in different phases of matter - is associated with the main topic of this thesis.

Chemical reactions generally occur in several elementary "steps", even on the catalyst. One of these steps is often the slowest, due to unfavourable energetics or sterical effects. The breaking of the very stable N_2 triple bond is, for example, seen as the limiting step in the Haber-Bosch process[7–9]. Such a

rate-limiting step is then particularly interesting for optimisation, as it would allow for a speed up of the entire reaction process. Similarly, by fine-tuning the catalyst and its environment, we would be able to more selectively produce one kind of product from a multi-step reaction process. On industrial scales, the focus would not just be on those catalysts that can most efficiently produce the desired product, but also on their stability, ease of production, and general economic costs associated with them.

In the field of theoretical surface science, in particular the subfield of heterogeneous catalysis, we aim to describe these rate-limiting elementary reaction steps to the best possible level using state-of-the-art theoretical methods. However, industrial catalysts are often complex structures of (metallic) nanoparticles, with many different sizes and crystal facets available, deposited on or in some form of supporting framework, and with a mix of molecules available that associate with the catalyst[10]. Therefore simplifications are often made, focussing on single crystal facets of the metallic catalyst, assuming (ultra-)low pressure of the reactant, or even assuming perfect, immobile surface slabs as a catalyst to describe single reactions as detailed as possible[11]. Likewise in this thesis, calculations are performed only for single (H_2) molecules reacting with a single crystal Cu(111) surface slab.

Metals as catalysts

As atoms cluster together to form solids their electronic orbitals will overlap and their electronic energy levels delocalise over the material. This forms bands of energy levels, either filled or empty, across the different energy levels, which are separated by "band gaps" where no energy levels exists. The Fermi-level, the (hypothetical) highest energy orbital still occupied by an electron, is found somewhere along this collection of bands and band gaps[12]. Everything below this Fermi-level in energy will mostly be filled with electrons, while everything above this level will be mostly empty energy levels.

Semi-conductors and insulators have Fermi-levels between two electronic bands, the lower energy valence band and the higher energy conduction band, which are separated by what is commonly known as *the* band gap[13]. In contrast metals form a special case of solids with a Fermi-level that is situated somewhere inside one of these electronic bands, completely lacking this band gap[12]. This makes metals excellent catalysts, as they can easily donate electrons out of, or accept electrons into, their electronic band structure with hardly any energetic cost involved.[14]

1.2 Hydrogen scattering from metal surfaces

The smallest, simplest, and easiest molecule to model for a gas-surface reaction is the hydrogen molecule (H_2). It consists of two protons and two electrons, which together form a relatively energetic single molecular bond. One, or both, of the atoms can also be substituted by the heavier deuterium (D) isotope, for which the nucleus consists of both a proton and a neutron. Outside its use as a lifting gas, coolant and especially as an energy carrier, H_2 is also an important reagent in many industrial and biological processes. The hydrogen molecule is also a key reagent in hydrogenation reactions performed in the petrochemical industry, in the synthesis of key industrial chemicals like methanol, and in the many biological processes of the living cell[15–18].

Although the basic mechanisms of the dissociative chemisorption of H_2 from metal surfaces have already been known for almost a century[19], the exact mechanisms governing selectivity, efficiency or even optimal catalytic particle design are still an open question today[20, 21]. Generally, experimental work is focused on most accurately describing the dissociation or scattering of the hydrogen molecules from single crystal surfaces under ultra-high vacuum (UHV) using either molecular beams (MB)[22–32] or through the inversion of the associative desorption experiments[28, 29, 33–37]. By carefully defining the MB, experimentalists are able to tune the distributions of the rotational and vibrational states of the H_2 inside the beam. The incidence energy normal to the surface can be adjusted by changing the angle of incidence of the beam and varying the nozzle temperature of the beam. Other MB work additionally relies on careful manipulation of the molecule using magnetic fields to obtain state-selective scattering probabilities, through a molecular spin-echo approach[23, 24]. Finally, by combining the associative desorption of H_2 with state-selective detection techniques, such as resonance-enhanced multi-photon ionisation (REMPI) and time-of-flight detection methods, experimentalists are able to investigate the relative dissociation rates of different rovibrational states at different incidence energies.

All these experimental results provide a treasure trove for the theoretician, who much prefers scattering from single well defined initial states to benchmark state-of-the-art theoretical methods. The tool that lies at the base of most theoretical approaches is density functional theory (DFT), which is used to solve the electronic part of the Schrödinger equation (See section 2.1.1). The results obtained from these DFT calculations provide the energy landscape, or potential energy surface (PES), brought about by the electrons of the system. This can in turn be used to investigate the motion of the nuclei over time. Here the exchange-correlation (XC)-density functional (DF) plays the vital role as
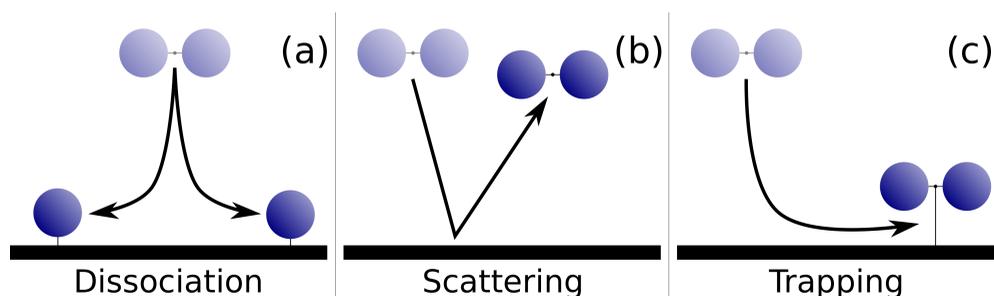
FIGURE 1.1:   Most common outcomes for hydrogen interacting with a (metal) catalyst surface. (a) The molecular bond breaks and the molecule dissociates; (b) the molecule gets reflected away from the surface, with or without changes to its rovibrational energy and/or its parallel momentum; (c) the molecule sticks to the surface, but does not dissociate.

the unknown piece of an otherwise exact description of the electronic system. As this perfect XC-DF is unknown, it is left to the scientific community to find the most accurate description available. While many different techniques with varying computational costs exist to achieve the best approximation to this perfect XC-DF, I would like to highlight one approach which will be important in the future chapters of this work: the specific reaction parameter (SRP) approach to DFT[38, 39]. Here usually a linear combination of two XC-DFs is made, one overestimating and one underestimating an experimental observable, by fitting to the optimal fraction of the two DFs (see section 2.1.1). With this semi-empirical approach, accurate descriptions of some aspects of the system of interest can be achieved without applying very complicated XC-DFs.

Basics of hydrogen scattering

As the hydrogen molecule approaches the catalyst surface, one of three things can happen, depending on its normal incidence energy. One likely outcome will be the dissociation of the molecule, where the molecular bond breaks as the electrons of the metal fill the anti-bonding orbitals of the molecule, which results in each atomic hydrogen getting separately chemisorbed to the surface [see Fig. 1.1(a)]. Such a reaction can either happen direct or after scattering events, in which case the molecule "bounces" a few times on the surface before dissociating. Outside of the obvious location and energetic height of the reaction barrier, the general shape of the PES is also important. For instance, changes in the energy levels of the rotational and vibrational states of the molecule resulting from changes in the H-H interaction potential near the surface would

allow for more, or less, of the molecule's internal energy to be used to surpass the reaction barriers[28, 29, 40].

Those molecules that do not react are generally scattered away from the surface, either immediately or after several "bounces", as illustrated in Fig. 1.1(b). Such an event includes not just energy exchange with the surface, which gets less and less likely as the mass mismatch between the hydrogen and the surface gets larger or the interaction time with the surface decreases, it can also result in energy exchange between the different degrees-of-freedom of the molecule itself[41]. At a quantum dynamical level, the scattering events can be rotationally, vibrationally, or rovibrationally elastic, if the rotational, vibrational, or the full rovibrational state does not change after scattering. If these states do change, the event is considered to be inelastic. Furthermore, the molecules can also be diffracted from the surface at specific angles, or diffraction orders[42], similar to X-rays or photons[43].

Finally, under some conditions it is also possible for the H_2 to get trapped on the surface without dissociating immediately [Fig. 1.1(c)]. For weak chemisorption (of H_2), this is paired with some electron transfer to the molecule's anti-bonding orbitals, but not enough to fully break the molecular bonds[44, 45]. In other cases no electron transfers occur at all, but the molecule could still experience the effects of a very weak (van der Waals) attraction to the surface, which is known as physisorption[46]. Often these trapped molecules will either dissociate as they lose energy to the surface, with or without diffusing towards better dissociation sites, or escape again from the surface. However, this dissociation process occurs over much longer time scales than is normally included in our calculations.

When investigating these systems using classical or quantum dynamical simulations, generally two important approximations are made: the Born-Oppenheimer (BO) approximation[47] and the static surface (SS) approximation. These together form what is commonly referred to as the BOSS approach[11, 39]. Furthermore, the surface is generally not only kept static, but also in its perfect crystal lattice structure.

Electron-hole pair excitations

The BO approximation is discussed in more detail in the section 2.1 of Chapter 2. It relies on the assumption that the electrons of an atom can instantaneously adjust themselves to any movement of the nucleus. In other words, one can find all the relevant energies for the system in two steps, first solving for just the electrons, with the nuclei held at different positions. The potential

energies found for these positions can then be used to construct a PES, which is subsequently used to study the dynamics of just the nuclei.

The main problem with the BO approximation is the loss of any non-adiabatic effects, most importantly the effect of electron-hole pair excitations on the system. Unfortunately going beyond the BO approximation is currently still considered very challenging, and therefore outside the scope of this work. However, progress has been made to correct for the additional effects, such as electron-hole (e-h) pair excitations, on the dissociation reactions[48–54]. In these works a fictional (electronic) friction term is introduced to model the effects of these e-h pairs, using methods such as the local density friction approximation (LDFA)[50, 51] or the more advanced orbital dependent friction (ODF) method[49, 52–55]. Previous work with both the LDFA and the ODF have shown the effects to be very small for the H_2 on Cu(111) dissociation reaction[53].

Static surface approximation

The static surface approximation is in many ways based on a similar idea as the BO approximation. Due to the very large mass mismatch between a hydrogen atom and a (metal) surface atom, the forces between the two would (almost) entirely result into changes of the momentum of the hydrogen only. Such an imbalance in the changes in momentum would be especially large when the interaction time between the hydrogen and the surface is relatively short, allowing for little time for the hydrogen to equilibrate with the surface. Thus by assuming the surface to be static, one neglects any effect of energy exchange between the surface and the hydrogen molecule. Such an energy exchange could have effects not just on the probability for dissociation, but also for the final rovibrational state in scattering events, as the H_2 will only be able to change states due to internal energy redistributions.

With the SS approximation, the surface is (usually) assumed to be in its perfect crystal lattice structure. An expansion of this approach is the sudden approximation, where the surface atoms are still kept static, but now distorted from their ideal positions. By averaging over many different distorted surfaces one can then include the effect of the moving, distorted surface on the system, assuming the interaction time is short. However, great care should be taken that this selection of distorted surfaces properly represents the configurations one would expect for the system of interest. Sudden approximations have been applied, often with great success, to many different dissociation reactions. These include not just H_2 dissociation[56–59], but also the heavier CO_2 or CH_4 reactions[60–65].

Effects of surface temperature

Another effect closely linked with the sudden approximation is that of surface temperature effects. While some motion is always present in the surface due to zero-point energies, it is greatly increased with increasing surface temperatures. As the surface temperature increases, thermal surface distortions will also gain a greater magnitude, reducing the effectiveness of the perfect crystal approximations generally used in the BOSS approach. Furthermore, the higher surface temperatures will also lead to increased thermal expansion of the surface slab, which further reduces the perfect lattice approximations. As one would expect, these thermal surface atoms displacements will also affect the H_2 reactive scattering reactions. In particular, Bonfanti *et al.* have shown how displacements of surface atoms would not just affect the dissociation barrier energetically, but also geometrically[56, 58]. Such a change of the barrier would thus not only affect the dissociation probability of H_2, but will equally affect the scattering of the hydrogen and its final rovibrational state or diffraction order.

Over the years, several different models with varying ranges of computational costs and degrees of overall accuracy, have been proposed to include surface temperature effects. For H_2 in particular, such models include the effective Hartree potential by Dutta *et al.*[66, 67], the static disorder parameter by Manson and co-workers[68] and the static corrugation model (SCM)[57, 59]. Several similar methods have also been suggested for methane dissociation. Busnengo *et al.* introduced both reactive force-field methods, as well as the static distorted surface (SDS) model, and moving surface dynamics[63, 65, 69]. Jackson *et al.* also introduced statically distorted surfaces to model surface temperature effects, as well as a single degree-of-freedom to model the surface motion itself[62, 64], and a reduced density matrix approach, where the surface is modeled as a phonon bath[70, 71]. Using perhaps more general approaches, several studies have also been performed using either ring polymer molecular dynamics[72, 73] or high-dimensional neural network potential approaches[74–77].

The SCM in particular will be at the centre of this thesis. It relies on modifying the perfect crystal lattice PES of the BOSS model to include the effect of thermally distorted surface atoms through (relatively) simple pair potentials, which are obtained from fitting to first principles data. Furthermore, by keeping the surface static, but distorted, the SCM is computationally efficient, as we will see from Chapter 4 onward. However, as of yet, it has only been applied to the H_2 dissociation from a Cu(111) surface slab. Thus while the expressions are expected to be general enough for use with other (transition

1

metal) surfaces, or diatomic molecules reacting with those, they have not been verified computationally. Neither have any parameters related to the SCM potential been determined for other systems than H_2/Cu. In addition, it also relies on accurate descriptions of the thermally distorted surface slabs to provide accurate results, which is an important topic in Chapter 3, as we will see.

1.3   Aim and scope of this thesis

As noted in the previous text, the inclusion of surface temperature effects has been a often revisited topic for surface scientists. Within this thesis I aim to further investigate these thermal effects for the well-studied reactive scattering of H_2 on Cu(111). Although this is one of the simplest systems available, theoretical models have been unable to accurately describe these surface temperature effects at a quantum dynamical level. Only recently have several models appeared that explicitly include all the degrees of freedom of just the hydrogen atoms. Using the static corrugation model (SCM), a solid theoretical database will be constructed of different experimental observables for the H_2/Cu(111) system, using both classical and state-of-the-art quantum dynamical approaches.

First in **Chapter 2**, the background of the techniques used throughout the thesis will be discussed, with a focus on quasi-classical dynamics (QCD) and the time-dependent wave packet (TDWP) approach to quantum dynamics (QD). Also outlined are the computations required to obtain several observables discussed throughout this work.

In **Chapter 3** a new approach to generate thermally distorted surface slabs for the SCM is introduced. It makes use of an embedded atom method (EAM) potential combined with molecular dynamics to generate a database of thermally distorted Cu(111) surfaces for a surface temperature of 925 K. D_2 dissociation results obtained using this EAM-SCM are compared to both those obtained from a random displacement (RD) approach based on the temperature dependent Debye-Waller factor, and previous experimental results. The validity of the EAM-SCM, and the sudden approximation, is further verified by comparing to results obtained from the EAM-based (classical) dynamic corrugation model (DCM), a modification of the SCM where surface motion is allowed during H_2 or D_2 interaction with the surface.

In **Chapter 4** the EAM-SCM, using the database of thermally distorted surfaces from the previous chapter, is implemented in a QD code based on the TDWP approach. To assess if the very small unit cell of the QD calculations is appropriate, several QCD calculations are performed where H_2 is constrained to a (1×1) unit cell, and compared to the results of the unrestricted hydrogen

molecule. To find if a smaller subset of the distorted surface database can adequately represent the full surface QCD calculations, results of only a small subset of the database are compared to results obtained from the full database. This reduction in surface slabs used is required due to the computational costs of even single surface QD simulations. Next, QD calculations for the rovibrational ground state are compared to results obtained using the QCD approach. The differences between, or agreement of, these QCD and QD results would then highlight quantum effects relevant to both dissociation and scattering probabilities for this system. Finally, by reducing the number of surface atoms included in the SCM, the effect of only displacing one, three, or five closest surface atoms is compared to distorting the entire surface.

Chapter 5 expands on this comparison, including rovibrationally excited states and different methods of binning the final rovibrational state of the QCD calculations, and how this compares to those obtained from the QD. These results, for both the BOSS and SCM approaches, are also compared to recent associative desorption experiments.

Finally **Chapter 6** will take a closer look at the level of noise one can expect for TDWP calculations, and how this could influence comparisons to the experimental results. Cuts of the PES for different thermally distorted surface slabs are investigated to better explain how the inclusion of the thermal effects affect the geometry and height of the (lowest) reaction barrier of the system. The dissociation curves of Chapter 5 are subsequently used to calculate several observables, including simulated time-of-flight spectra, and rotational and vibrational efficacies, which can be more directly compared to available experimental work. These, together with the curves of the Chapter 5, will then also provide a solid set of results to compare to future studies.

1.4 Main results

This section will cover the main results discussed in each of the chapters of the thesis.

Chapter 3: Beyond the static corrugation model

A database of thermally distorted surface slabs of Cu(111) at a modelled temperature of 925 K is constructed using molecular dynamics and a highly accurate embedded atom method (EAM) approach[78]. These distorted slabs are implemented into the static corrugation model (SCM) and used to investigate the dissociation of D_2 on a Cu(111) surface slab at a QCD level for several initial rovibrational states of the molecule. Also included for comparison are

SCM results using the random displacement (RD) approach to SCM surface construction used in older studies[57, 59].

The SCM obtained dissociation curves and simulated time-of-flight spectra show increased widths compared to BOSS results where surface temperature effects are not included. This curve broadening of the SCM results is a characteristic effect, generally ascribed to surface temperature[79]. Dynamic corrugation model (DCM) results, which explicitly include a moving surface described by an EAM potential, also have almost perfect agreement with the EAM-SCM results. This strengthens the sudden approximation, one of the cornerstones of the SCM, and shows the minimal effect energy exchange has on the dissociation of D_2 on a thermally excited Cu(111) surface.

Surface configurations obtained from the EAM molecular dynamics are found to have a much broader distribution of surface atom displacements than configurations obtained from the bulk-like RD approach. This could be an explanation for the difference in saturation values we find between results of the EAM and RD generated surface slabs, although this has not been further explored. These displacement distributions of the EAM-SCM generated surface slabs also reveal a preference for D_2 (at lower incidence energies) to react with surfaces for which the surface atoms are displaced towards the bulk. Such an effect is not present for displacements parallel to the surface, or observed at all for results obtained with the RD-SCM.

Chapter 4: Quantum dynamical surface temperature effects on the dissociative chemisorption of H_2 from Cu(111)

As Chapter 3 has established the validity of the EAM approach to SCM and the limited effect of energy exchange on the dissociation reaction of D_2 on Cu(111), the EAM-SCM is now also used in TDWP QD simulations.

H_2 dissociation probabilities obtained using the QD-EAM-SCM approach were very similar to those obtained using the QCD-EAM-SCM approach, both when considering single surfaces or as an average over 104 different surface slabs. QD-BOSS and QCD-BOSS dissociation curves also agreed well with each other, although the QD results had clear fluctuations, attributed to imperfections of the PES.

Rovibrationally elastic scattering probabilities, however, show a clear disagreement between QD and QCD obtained results, in particular for the EAM-SCM results. Comparisons between the QD and QCD scattering probabilities for individual distorted surface slabs reveals slabs with very low reactivity as the biggest contributors to this difference, at least for the surface slabs considered. The clear difference between classical and quantum results highlights

the importance of performing quantum dynamical simulations when trying to describe the H_2/Cu(111) system exactly. This difference becomes especially relevant when also including surface temperature effects, and when not only focusing on the dissociation reaction.

Finally, distorted surface configurations are considered where only one, three, or five surface atoms are in their distorted positions. It is found that five displaced surface atoms suffice to accurately describe the effect of the surface distortions on the dissociation curve. However, the general disagreement found between the QD and QCD scattering results is already clear when considering only one displaced surface atom. The good agreement between SCM results with a fully distorted surface and with only five surface atoms distorted can be well explained by the distance of the surface atoms from the incoming H_2. Only approximately the closest seven surface atoms are found within a region where the SCM potential significantly contributes to the total PES.

Chapter 5: The quantum dynamics of H_2 on Cu(111) at a surface temperature of 925 K: Comparing theory to experiments

Results obtained using the QD-EAM-SCM for the reactive scattering of H_2 from Cu(111) are now expanded to also include rovibrationally excited initial states. QCD-EAM-SCM results are also still considered, but expanded upon by adding the moving surface EAM-DCM approach.

Very good agreement is found between the dissociation curves of the QD- and QCD-EAM-SCM for the initially rovibrationally excited H_2, although some small differences are found for the higher initial vibrational states v = 1. The moving surface QCD-EAM-DCM results also agreed well with both the static surface EAM-SCM approaches, as was also observed for D_2 in Chapter 3.

Some approaches to binning the final rovibrational state of the molecules scattered during the QCD trajectories were also tested. Little difference was found between either binning to the closest allowed rotational state, or using weights to only include that final rotational states that are allowed by quantum mechanics. Rounding down towards an allowed rotational state, however, vastly underestimated scattering results computed with QD, but only for those trajectories where the initial rotational state was equal to the lowest allowed state (J = 0, 1).

The QD and QCD dissociation curves were also directly compared to published experimental curves from Kaufmann *et al.* obtained from associative desorption measurements[37]. Unfortunately the methods of measuring these curves ensured there was a large amount of uncertainty in the saturation value of the experimental results. Nevertheless, EAM-SCM was shown to better

describe the experimental curve onset than the BOSS approach, especially for the lower initial rovibrational states. A closer look at these onsets, however, also revealed a large amount of noise present in the QD results. This is believed to be primarily caused by the size of the time step (1.5 au) used in the split operator method when propagating the wave-packet in the calculations. Although this value was typical for most calculations performed in the past, it likely lead to significant noise when considering probabilities below 10^{-3}.

Chapter 6: The quantum dynamics of H_2 on Cu(111) at a surface temperature of 925 K: Comparing theory to experiments 2

As a direct continuation of Chapter 5, additional calculations are performed to investigate the effect of the time step of the SPO method on the noise in the dissociation curves. By reducing the time step by a factor 15 (to 0.1 au) for a single BOSS calculation, the error found in the curve is reduced by two orders of magnitude (to 10^{-5}). The noise still present in this reaction probability range is well below the levels found in the experimentally verified signal.

Cuts of the SCM PESs for several thermally distorted surfaces are also compared to the ideal lattice BOSS PES, with a focus on the reaction barrier on each cut. When including the surface temperature effects, the lowest reaction barrier on the bridge-to-hollow reaction site is found to move slightly towards a larger H−H distance, while at the same time moving a little closer to the surface.

To match the approach of previous studies, the dissociation curves of Chapter 5 are also fitted to several sigmoidal functions, which are subsequently used for the simulation of time-of-flight (ToF) spectra. These ToF spectra showed improved agreement with the experimental spectra of Kaufmann *et al.*[37] when using the EAM-SCM approach over the BOSS approach.

The fitting parameters of the sigmoidal function are directly compared to the experimental parameters and to each other. The inflection points of the QCD-EAM-SCM curves at different initial states are found to agree very well, slightly overestimating the experimental values, but displaying the same curvature. The width parameters of the EAM-SCM curves are found to be higher than those of the BOSS results across all initial states, yet both overestimated the value reported in the experiment[37]. This curve broadening due to surface temperature effects for the EAM-SCM has also already been observed for D_2 on Cu(111) as discussed in Chapter 3.

The rotational and vibrational efficacies, measures of the extent to which additional rotational and vibrational energy helps the molecule surpass the dissociation barrier, are calculated by determining the energy shift between

the results of the rovibrational ground state and the excited states. Theory was found to not reproduce the negative rotational efficacy for lower rotational states with either the EAM-SCM or the BOSS approaches, although it captured this parameter well for the higher rotational energies. For the vibrational efficacies, the SCM reproduced experiment (slightly) better than the BOSS, especially when considering the QD results.

Finally the preference for the H_2 to react rotating either parallel to normal to the surface is investigated by calculating the rotational quadrupole alignment parameter. QD results are found to predict a larger preference for rotation parallel to the surface compared to QCD for lower initial rovibrational states, regardless of the BOSS or SCM approach used. This effect disappears, however, when higher initial rovibrational states are considered. In general, the SCM predicted a slightly smaller preference towards parallel rotation compared to the BOSS. This can be well explained by the distorted nature of the surface making exactly parallel rotation less favorable.

1.5 Outlook

As science progresses, new findings and unexpected results pave the way for new research. Thus it has also been for this thesis, where new results of this thesis, or new results released in the same time-frame allowed us to speculate a little on those topics that could be interesting for further study.

The SCM is shown to clearly affect not only the broadness of the dissociation curves of the H_2, but also the scattering probabilities. However, all the work so far has focused on surface slabs at the relatively high surface temperature of 925 K, which are easily described using classical dynamics for the motion of the surface atoms. Unfortunately, this regime is also ill-suited for comparisons with ultra-high vacuum beam adsorption experiments, which are typically performed on surfaces of much lower temperatures. Reducing the surface temperature of the classical dynamics is possible to a degree, however it will start deviating from an exact solution as this temperature dips below the Debye temperature of the surface. Under this Debye temperature zero-point energies and accurate distributions of the quantum mechanically allowed energy levels becomes important, and the surface can not be treated with classical dynamics. Instead other ways would have to be found to generate accurate surface slabs at low surface temperatures, not based purely on classical dynamics approaches. The effect these thermal surface distortions have on the reaction, based on the works in this thesis, are expected to be quite minor. Nevertheless, they could

become more important when one wants to carefully consider specific state-to-state scattering probabilities and/or diffraction of the hydrogen molecule[23, 24].

Another, perhaps expected, future direction of the SCM itself would be expanding the model towards first other Cu lattices, and then eventually to other systems with metals surfaces or other diatomic molecules. As the SCM coupling potential itself only relies on (effective three-body) pair potentials, it should be directly transferable to other Cu lattices when considering H_2, although this has not yet been tested extensively to my knowledge. If the transferability to other copper surface facets is found to be insufficient, additional SRP48 DFT calculations could be easily included to aid in additional fitting to the same functional form. It is very unlikely that the general formulation of the potential would fail when different lattice configurations are involved. Fitting the SCM to other surfaces, or for other diatomics, would of course require new (DFT) calculations. Here an important consideration is the careful selection of surface slab configurations to include in the data-set, ensuring specific distortions are not oversampled. Again, it would be important to first investigate if the sudden approximation is applicable, by considering both the interaction time of the diatomic of choice with the surface, as well as the mass mismatch between the reactant and the surface atoms. If required, additional terms could be added to the potential to account for non-adiabatic effects, which would most likely be best modelled by electronic friction terms.

Other methods of including surface temperature effects have also seen developments, most notably the many variations of the high-dimensional neural network potential approaches (HD-NNPs). These approaches rely on a vast amount of parameters, fitted using machine learning techniques, which allows the NN to describe entire systems, including surface motion, as a single potential[80, 81]. An important topic in this field are the hyperparameters of the system; those parameters that generally have to be manually selected to help guide the machine learning process[82]. Nevertheless, methods do now exist to optimise these hyperparameters automatically[83]. Often additional terms are also used to aid in the fitting, enforcing symmetry through a variety of ways[84]. Although these NNs generally rely on physically motivated functions to describe the interaction between nodes, the nodes themselves will often still consist of fairly simple activation functions, requiring many nodes to construct the whole network. Neural networks are thus often unsuitable to perform any kind of extrapolation outside of the data-set it has been trained on, as its large amount of functions will all behave unexpectedly outside of their intended ranges. Although by carefully constructing these NNPs, some these extrapolation effects can be somewhat diminished[76]. Both these downsides,

the extrapolation and the large amount of function evaluations, greatly affect the effectiveness of NNs when used in the quantum dynamics calculations as they were performed for this thesis. These QD calculations require evaluating the entire PES across the six degrees of freedom of the hydrogen molecule, which can result into up to 10^9 potential evaluations. Furthermore, including surface temperature using a sudden approximation also requires calculating tens to hundreds of PESs to obtain well converged average results.

This contrasts the workings of the SCM, which was designed with the eventual implementation into QD simulations as a primary goal. Its small selection of physically motivated functions to describe molecule-surface interactions, and the models ability to extrapolate (somewhat) outside of the training data provide an ideal basis for calculating the large amount of energies needed to construct a full 6D PES. However, with the recent progress regarding HD-NNPs and the endlessly growing computational power of modern machines, some time in the future NNs will inevitably catch up[85]. It is there that SCM should still provide a solid basis to both benchmark new techniques as well as provide a computationally cheap alternative to compare to. A more direct connection between the SCM and HD-NNPs could also be made, replacing the physically motivated coupling potential of the SCM with some form of an NNP instead. While some preliminary work has been performed on this approach, it has not been fully explored yet. Nevertheless, such a "fusion" of the SCM and NNPs would greatly reduce the computational speed of the model, one of the main advantages.

In a more general sense, the big focus on improving the accuracy of the exchange-correlation functionals pivotal for DFT calculations also provides opportunities for the development of better SCM (coupling) potentials. By "climbing Jacob's ladder"[86], the model can move beyond the use of simple GGA functionals towards the more advanced meta-GGA or hybrid functionals, which could also improve the general applicability of such a newly fitted model. Nevertheless, computational costs should also be taken into account, as many surface distortions are first required to obtain an accurate expression of the SCM coupling potential.

References

(1)   Ertl, G. Reactions at Surfaces: From Atoms to Complexity (Nobel Lecture). *Angewandte Chemie International Edition* **2008**, *47*, 3524–3535, DOI: 10.1002/anie.200800480.

(2)   Van Dishoeck, E. F. Astrochemistry: Overview and Challenges. *Proceedings of the International Astronomical Union* **2017**, *13*, 3–22, DOI: 10.1017/S1743921317011528.

(3)   Palmer, T.; Bonner, P. L., *Enzymes: Biochemistry, Biotechnology, Clinical Chemistry*; Elsevier: 2007.

(4)   Chiusoli, G. P.; Maitlis, P. M., *Metal-Catalysis in Industrial Organic Processes*; Royal Society of Chemistry: 2019.

(5)   Smith, C.; Hill, A. K.; Torrente-Murciano, L. Current and future role of Haber–Bosch ammonia in a carbon-free energy landscape. *Energy & Environmental Science* **2020**, *13*, 331–344, DOI: 10.1039/C9EE02873K.

(6)   Chorkendorff, I., *Concepts of Modern Catalysis and Kinetics*; Wiley-VCH: Weinheim, 2003.

(7)   Ertl, G. Primary Steps in Catalytic Synthesis of Ammonia. *Journal of Vacuum Science & Technology A* **1983**, *1*, 1247–1253, DOI: 10.1116/1.572299.

(8)   Stoltze, P.; Nørskov, J. K. Bridging the "Pressure Gap" between Ultrahigh-Vacuum Surface Physics and High-Pressure Catalysis. *Physical Review Letters* **1985**, *55*, 2502–2505, DOI: 10.1103/PhysRevLett.55.2502.

(9)   Honkala, K.; Hellman, A.; Remediakis, I. N.; Logadottir, A.; Carlsson, A.; Dahl, S.; Christensen, C. H.; Nørskov, J. K. Ammonia Synthesis from First-Principles Calculations. *Science* **2005**, *307*, 555–558, DOI: 10.1126/science.1106435.

(10)   Morbidelli, M.; Gavriilidis, A.; Varma, A., *Catalyst Design: Optimal Distribution of Catalyst in Pellets, Reactors, and Membranes*; Cambridge Series in Chemical Engineering; Cambridge University Press: Cambridge, 2001, DOI: 10.1017/CBO9780511721762.

(11)   Kroes, G.-J. Computational approaches to dissociative chemisorption on metals: towards chemical accuracy. *Physical Chemistry Chemical Physics* **2021**, *23*, 8962–9048, DOI: 10.1039/D1CP00044F.

(12)   Kittel, C.; McEuen, P., *Introduction to Solid State Physics*; John Wiley & Sons: 2018.

(13) Sze, S. M.; Ng, K. K., *Physics of Semiconductor Devices*; John Wiley & Sons: 2006.

(14) Kiselev, V. F.; Krylov, O. V., *Adsorption and Catalysis on Transition Metals and Their Oxides*; Springer Science & Business Media: 2012.

(15) Thauer, R. K.; Klein, A. R.; Hartmann, G. C. Reactions with Molecular Hydrogen in Microorganisms: Evidence for a Purely Organic Hydrogenation Catalyst. *Chemical Reviews* **1996**, *96*, 3031–3042, DOI: `10.1021/cr9500601`.

(16) Lange, J.-P. Methanol Synthesis: A Short Review of Technology Improvements. *Catalysis Today* **2001**, *64*, 3–8, DOI: `10.1016/S0920-5861(00)00503-4`.

(17) Marcilly, C. Present Status and Future Trends in Catalysis for Refining and Petrochemicals. *Journal of Catalysis* **2003**, *216*, 47–62, DOI: `10.1016/S0021-9517(02)00129-X`.

(18) Mäki-Arvela, P.; Hájek, J.; Salmi, T.; Murzin, D. Y. Chemoselective Hydrogenation of Carbonyl Compounds over Heterogeneous Catalysts. *Applied Catalysis A: General* **2005**, *292*, 1–49, DOI: `10.1016/j.apcata.2005.05.045`.

(19) Horiuti, I.; Polanyi, M. Exchange Reactions of Hydrogen on Metallic Catalysts. *Transactions of the Faraday Society* **1934**, *30*, 1164–1172, DOI: `10.1039/TF9343001164`.

(20) Kroes, G.-J.; Díaz, C. Quantum and classical dynamics of reactive scattering of H_2 from metal surfaces. *Chemical Society Reviews* **2016**, *45*, 3658–3700, DOI: `10.1039/c5cs00336a`.

(21) Zaera, F. The Surface Chemistry of Metal-Based Hydrogenation Catalysis. *ACS Catalysis* **2017**, *7*, 4947–4967, DOI: `10.1021/acscatal.7b01368`.

(22) Balooch, M.; Cardillo, M. J.; Miller, D. R.; Stickney, R. E. Molecular Beam Study of the Apparent Activation Barrier Associated with Adsorption and Desorption of Hydrogen on Copper. *Surface Science* **1974**, *46*, 358–392, DOI: `10.1016/0039-6028(74)90315-X`.

(23) Chadwick, H.; Alkoby, Y.; Cantin, J. T.; Lindebaum, D.; Godsi, O.; Maniv, T.; Alexandrowicz, G. Molecular spin echoes; multiple magnetic coherences in molecule surface scattering experiments. *Physical Chemistry Chemical Physics* **2021**, *23*, 7673–7681, DOI: `10.1039/D0CP05399F`.

1

(24)   Chadwick, H.; Somers, M. F.; Stewart, A. C.; Alkoby, Y.; Carter, T. J. D.; Butkovicova, D.; Alexandrowicz, G. Stopping Molecular Rotation Using Coherent Ultra-Low-Energy Magnetic Manipulations. *Nature Communications* **2022**, *13*, 2287, DOI: 10.1038/s41467-022-29830-3.

(25)   Berger, H. F.; Leisch, M.; Winkler, A.; Rendulic, K. D. A Search for Vibrational Contributions to the Activated Adsorption of H_2 on Copper. *Chemical Physics Letters* **1990**, *175*, 425–428, DOI: 10.1016/0009-2614(90)85558-T.

(26)   Michelsen, H. A.; Auerbach, D. J. A critical examination of data on the dissociative adsorption and associative desorption of hydrogen at copper surfaces. *The Journal of Chemical Physics* **1991**, *94*, 7502–7520, DOI: 10.1063/1.460182.

(27)   Rettner, C. T.; Auerbach, D. J.; Michelsen, H. A. Observation of Direct Vibrational Excitation in Collisions of H_2 and D_2 with a Cu(111) Surface. *Physical Review Letters* **1992**, *68*, 2547–2550, DOI: 10.1103/PhysRevLett.68.2547.

(28)   Michelsen, H. A.; Rettner, C. T.; Auerbach, D. J.; Zare, R. N. Effect of rotation on the translational and vibrational energy dependence of the dissociative adsorption of D_2 on Cu(111). *The Journal of Chemical Physics* **1993**, *98*, 8294–8307, DOI: 10.1063/1.464535.

(29)   Rettner, C. T.; Michelsen, H. A.; Auerbach, D. J. Quantum-state-specific dynamics of the dissociative adsorption and associative desorption of H_2 at a Cu(111) surface. *The Journal of Chemical Physics* **1995**, *102*, 4625–4641, DOI: 10.1063/1.469511.

(30)   Hodgson, A.; Samson, P.; Wight, A.; Cottrell, C. Rotational Excitation and Vibrational Relaxation of H_2 Scattered from Cu(111). *Physical Review Letters* **1997**, *78*, 963–966, DOI: 10.1103/PhysRevLett.78.963.

(31)   Murphy, M. J.; Hodgson, A. Role of Surface Thermal Motion in the Dissociative Chemisorption and Recombinative Desorption of D_2 on Ag(111). *Physical Review Letters* **1997**, *78*, 4458–4461, DOI: 10.1103/PhysRevLett.78.4458.

(32)   Cao, K.; Füchsel, G.; Kleyn, A. W.; Juurlink, L. B. F. Hydrogen adsorption and desorption from Cu(111) and Cu(211). *Physical Chemistry Chemical Physics* **2018**, *20*, 22477–22488, DOI: 10.1039/C8CP03386B.

(33)   Hou, H.; Gulding, S. J.; Rettner, C. T.; Wodtke, A. M.; Auerbach, D. J. The Stereodynamics of a Gas-Surface Reaction. *Science* **1997**, *277*, 80–82, DOI: 10.1126/science.277.5322.80.

(34) Sementa, L.; Wijzenbroek, M.; van Kolck, B. J.; Somers, M. F.; Al-Halabi, A.; Busnengo, H. F.; Olsen, R. A.; Kroes, G. J.; Rutkowski, M.; Thewes, C.; Kleimeier, N. F.; Zacharias, H. Reactive scattering of H_2 from Cu(100): Comparison of dynamics calculations based on the specific reaction parameter approach to density functional theory with experiment. *The Journal of Chemical Physics* **2013**, *138*, 044708, DOI: 10.1063/1.4776224.

(35) Nattino, F.; Genova, A.; Guijt, M.; Muzas, A. S.; Díaz, C.; Auerbach, D. J.; Kroes, G.-J. Dissociation and recombination of D_2 on Cu(111): ab initio molecular dynamics calculations and improved analysis of desorption experiments. *The Journal of Chemical Physics* **2014**, *141*, 124705, DOI: 10.1063/1.4896058.

(36) Shuai, Q.; Kaufmann, S.; Auerbach, D. J.; Schwarzer, D.; Wodtke, A. M. Evidence for Electron–Hole Pair Excitation in the Associative Desorption of H_2 and D_2 from Au(111). *The Journal of Physical Chemistry Letters* **2017**, *8*, 1657–1663, DOI: 10.1021/acs.jpclett.7b00265.

(37) Kaufmann, S.; Shuai, Q.; Auerbach, D. J.; Schwarzer, D.; Wodtke, A. M. Associative desorption of hydrogen isotopologues from copper surfaces: Characterization of two reaction mechanisms. *The Journal of Chemical Physics* **2018**, *148*, 194703, DOI: 10.1063/1.5025666.

(38) Chuang, Y.-Y.; Radhakrishnan, M. L.; Fast, P. L.; Cramer, C. J.; Truhlar, D. G. Direct Dynamics for Free Radical Kinetics in Solution: Solvent Effect on the Rate Constant for the Reaction of Methanol with Atomic Hydrogen. *The Journal of Physical Chemistry A* **1999**, *103*, 4893–4909, DOI: 10.1021/jp990969d.

(39) Díaz, C.; Pijper, E.; Olsen, R. A.; Busnengo, H. F.; Auerbach, D. J.; Kroes, G. J. Chemically accurate simulation of a prototypical surface reaction: H_2 dissociation on Cu(111). *Science (New York, N.Y.)* **2009**, *326*, 832–834, DOI: 10.1126/science.1178722.

(40) Darling, G. R.; Holloway, S. Rotational Motion and the Dissociation of H_2 on Cu(111). *The Journal of Chemical Physics* **1994**, *101*, 3268–3281, DOI: 10.1063/1.467574.

(41) Jackson, J. M.; Howarth, A.; Hartree, D. R. Exchange of Energy between Diatomic Gas Molecules and a Solid Surface. *Proceedings of the Royal Society of London. Series A - Mathematical and Physical Sciences* **1997**, *152*, 515–529, DOI: 10.1098/rspa.1935.0206.

(42) Estermann, I.; Stern, O. Beugung von Molekularstrahlen. *Zeitschrift für Physik* **1930**, *61*, 95–125, DOI: 10.1007/BF01340293.

(43)   Raman, C. V., *Molecular Diffraction of Light*; University of Calcutta: 1922.

(44)   Newns, D. M. Self-Consistent Model of Hydrogen Chemisorption. *Physical Review* **1969**, *178*, 1123–1135, DOI: 10.1103/PhysRev.178.1123.

(45)   Hammer, B.; Nørskov, J. K. Electronic Factors Determining the Reactivity of Metal Surfaces. *Surface Science* **1995**, *343*, 211–220, DOI: 10.1016/0039-6028(96)80007-0.

(46)   Burns, G., *Solid State Physics*; Academic Press: 1985.

(47)   Born, M.; Oppenheimer, R. Zur Quantentheorie Der Molekeln. *Annalen der Physik* **1927**, *389*, 457–484, DOI: 10.1002/andp.19273892002.

(48)   Persson, M.; Hellsing, B. Electronic Damping of Adsorbate Vibrations on Metal Surfaces. *Physical Review Letters* **1982**, *49*, 662–665, DOI: 10.1103/PhysRevLett.49.662.

(49)   Hellsing, B.; Persson, M. Electronic Damping of Atomic and Molecular Vibrations at Metal Surfaces. *Physica Scripta* **1984**, *29*, 360–371, DOI: 10.1088/0031-8949/29/4/014.

(50)   Juaristi, J. I.; Alducin, M.; Muiño, R. D.; Busnengo, H. F.; Salin, A. Role of Electron-Hole Pair Excitations in the Dissociative Adsorption of Diatomic Molecules on Metal Surfaces. *Physical Review Letters* **2008**, *100*, 116102, DOI: 10.1103/PhysRevLett.100.116102.

(51)   Novko, D.; Blanco-Rey, M.; Alducin, M.; Juaristi, J. I. Surface Electron Density Models for Accurate Ab Initio Molecular Dynamics with Electronic Friction. *Physical Review B* **2016**, *93*, 245435, DOI: 10.1103/PhysRevB.93.245435.

(52)   Maurer, R. J.; Jiang, B.; Guo, H.; Tully, J. C. Mode Specific Electronic Friction in Dissociative Chemisorption on Metal Surfaces: H_2 on Ag(111). *Physical Review Letters* **2017**, *118*, 256001, DOI: 10.1103/PhysRevLett.118.256001.

(53)   Spiering, P.; Meyer, J. Testing Electronic Friction Models: Vibrational De-excitation in Scattering of H_2 and D_2 from Cu(111). *The Journal of Physical Chemistry Letters* **2018**, *9*, 1803–1808, DOI: 10.1021/acs.jpclett.7b03182.

(54)   Spiering, P.; Shakouri, K.; Behler, J.; Kroes, G.-J.; Meyer, J. Orbital-Dependent Electronic Friction Significantly Affects the Description of Reactive Scattering of N_2 from Ru(0001). *The Journal of Physical Chemistry Letters* **2019**, *10*, 2957–2962, DOI: 10.1021/acs.jpclett.9b00523.

(55) Head-Gordon, M.; Tully, J. C. Molecular Dynamics with Electronic Frictions. *The Journal of Chemical Physics* **1995**, *103*, 10137–10145, DOI: 10.1063/1.469915.

(56) Bonfanti, M.; Díaz, C.; Somers, M. F.; Kroes, G.-J. Hydrogen Dissociation on Cu(111): The Influence of Lattice Motion. Part I. *Physical Chemistry Chemical Physics* **2011**, *13*, 4552, DOI: 10.1039/c0cp01746a.

(57) Wijzenbroek, M.; Somers, M. F. Static surface temperature effects on the dissociation of H_2 and D_2 on Cu(111). *The Journal of Chemical Physics* **2012**, *137*, 054703, DOI: 10.1063/1.4738956.

(58) Bonfanti, M.; Somers, M. F.; Díaz, C.; Busnengo, H. F.; Kroes, G.-J. 7D Quantum Dynamics of H_2 Scattering from Cu(111): The Accuracy of the Phonon Sudden Approximation. *Zeitschrift für Physikalische Chemie* **2013**, 130617035227002, DOI: 10.1524/zpch.2013.0405.

(59) Spiering, P.; Wijzenbroek, M.; Somers, M. F. An improved static corrugation model. *The Journal of Chemical Physics* **2018**, *149*, 234702, DOI: 10.1063/1.5058271.

(60) Nave, S.; Jackson, B. Methane Dissociation on Ni(111): The Role of Lattice Reconstruction. *Physical Review Letters* **2007**, *98*, 173003, DOI: 10.1103/PhysRevLett.98.173003.

(61) Tiwari, A. K.; Nave, S.; Jackson, B. Methane Dissociation on Ni(111): A New Understanding of the Lattice Effect. *Physical Review Letters* **2009**, *103*, 253201, DOI: 10.1103/PhysRevLett.103.253201.

(62) Tiwari, A. K.; Nave, S.; Jackson, B. The temperature dependence of methane dissociation on Ni(111) and Pt(111): Mixed quantum-classical studies of the lattice response. *The Journal of Chemical Physics* **2010**, *132*, 134702, DOI: 10.1063/1.3357415.

(63) Lozano, A.; Shen, X. J.; Moiraghi, R.; Dong, W.; Busnengo, H. F. Cutting a chemical bond with demon's scissors: Mode- and bond-selective reactivity of methane on metal surfaces. *Surface Science* **2015**, *640*, 25–35, DOI: 10.1016/j.susc.2015.04.002.

(64) Guo, H.; Farjamnia, A.; Jackson, B. Effects of Lattice Motion on Dissociative Chemisorption: Toward a Rigorous Comparison of Theory with Molecular Beam Experiments. *The Journal of Physical Chemistry Letters* **2016**, *7*, 4576–4584, DOI: 10.1021/acs.jpclett.6b01948.

1

(65) Seminara, G. N.; Peludhero, I. F.; Dong, W.; Martínez, A. E.; Busnengo, H. F. Molecular Dynamics Study of Molecular and Dissociative Adsorption Using System-Specific Force Fields Based on Ab Initio Calculations: CO/Cu(110) and CH$_4$/Pt(110). *Topics in Catalysis* **2019**, *62*, 1044–1052, DOI: 10.1007/s11244-019-01196-9.

(66) Dutta, J.; Mandal, S.; Adhikari, S.; Spiering, P.; Meyer, J.; Somers, M. F. Effect of surface temperature on quantum dynamics of H$_2$ on Cu(111) using a chemically accurate potential energy surface. *The Journal of Chemical Physics* **2021**, *154*, 104103, DOI: 10.1063/5.0035830.

(67) Dutta, J.; Naskar, K.; Adhikari, S.; Spiering, P.; Meyer, J.; Somers, M. F. Effect of surface temperature on quantum dynamics of D$_2$ on Cu(111) using a chemically accurate potential energy surface, To Be Submitted, 2022, submitted.

(68) Kroes, G. J.; Wijzenbroek, M.; Manson, J. R. Possible effect of static surface disorder on diffractive scattering of H$_2$ from Ru(0001): Comparison between theory and experiment. *The Journal of Chemical Physics* **2017**, *147*, 244705, DOI: 10.1063/1.5011741.

(69) Xiao, Y.; Dong, W.; Busnengo, H. F. Reactive force fields for surface chemical reactions: A case study with hydrogen dissociation on Pd surfaces. *The Journal of Chemical Physics* **2010**, *132*, 014704, DOI: 10.1063/1.3265854.

(70) Jackson, B. The Trapping of Methane on Ir(111): A First-Principles Quantum Study. *The Journal of Chemical Physics* **2021**, *155*, 044705, DOI: 10.1063/5.0058672.

(71) Jackson, B. Quantum studies of methane-metal inelastic diffraction and trapping: The variation with molecular orientation and phonon coupling. *Chemical Physics* **2022**, *559*, 111516, DOI: 10.1016/j.chemphys.2022.111516.

(72) Craig, I. R.; Manolopoulos, D. E. Quantum Statistics and Classical Mechanics: Real Time Correlation Functions from Ring Polymer Molecular Dynamics. *The Journal of Chemical Physics* **2004**, *121*, 3368–3373, DOI: 10.1063/1.1777575.

(73) Suleimanov, Y. V.; Aoiz, F. J.; Guo, H. Chemical Reaction Rate Coefficients from Ring Polymer Molecular Dynamics: Theory and Practical Applications. *The Journal of Physical Chemistry A* **2016**, *120*, 8488–8502, DOI: 10.1021/acs.jpca.6b07140.

(74) Behler, J. First Principles Neural Network Potentials for Reactive Simulations of Large Molecular and Condensed Systems. *Angewandte Chemie International Edition* **2017**, *56*, 12828–12840, DOI: https://doi.org/10.1002/anie.201703114.

(75) Artrith, N.; Behler, J. High-dimensional neural network potentials for metal surfaces: A prototype study for copper. *Physical Review B* **2012**, *85*, 045439, DOI: 10.1103/PhysRevB.85.045439.

(76) Zhu, L.; Zhang, Y.; Zhang, L.; Zhou, X.; Jiang, B. Unified and transferable description of dynamics of H_2 dissociative adsorption on multiple copper surfaces *via* machine learning. *Physical Chemistry Chemical Physics* **2020**, *22*, 13958–13964, DOI: 10.1039/D0CP02291H.

(77) Lin, Q.; Zhang, L.; Zhang, Y.; Jiang, B. Searching Configurations in Uncertainty Space: Active Learning of High-Dimensional Neural Network Reactive Potentials. *Journal of Chemical Theory and Computation* **2021**, *17*, 2691–2701, DOI: 10.1021/acs.jctc.1c00166.

(78) Sheng, H. W.; Kramer, M. J.; Cadien, A.; Fujita, T.; Chen, M. W. Highly optimized embedded-atom-method potentials for fourteen fcc metals. *Physical Review B* **2011**, *83*, 134118, DOI: 10.1103/PhysRevB.83.134118.

(79) Michelsen, H. A.; Rettner, C. T.; Auerbach, D. J. On the Influence of Surface Temperature on Adsorption and Desorption in the D_2/Cu(111) System. *Surface Science* **1992**, *272*, 65–72, DOI: 10.1016/0039-6028(92)91422-8.

(80) Gurney, K., *An Introduction to Neural Networks*; CRC Press: 1997.

(81) Behler, J.; Parrinello, M. Generalized Neural-Network Representation of High-Dimensional Potential-Energy Surfaces. *Physical Review Letters* **2007**, *98*, 146401, DOI: 10.1103/PhysRevLett.98.146401.

(82) Montavon, G.; Orr, G.; Müller, K.-R., *Neural Networks: Tricks of the Trade*; Springer: 2012.

(83) Thie, A.; Menger, M. F.; Faraji, S. HOAX: A Hyperparameter Optimisation Algorithm Explorer for Neural Networks. *Molecular Physics* **2023**, *0*, e2172732, DOI: 10.1080/00268976.2023.2172732.

(84) Schütt, K. T.; Chmiela, S.; von Lilienfeld, O. A.; Tkatchenko, A.; Tsuda, K.; Müller, K.-R., *Machine Learning Meets Quantum Physics*; Springer Nature: 2020.

(85)   Manzhos, S.; Dawes, R.; Carrington, T. Neural Network-Based Approaches for Building High Dimensional and Quantum Dynamics-Friendly Potential Energy Surfaces. *International Journal of Quantum Chemistry* **2015**, *115*, 1012–1020, DOI: `10.1002/qua.24795`.

(86)   Perdew, J. P.; Schmidt, K. Jacob's Ladder of Density Functional Approximations for the Exchange-Correlation Energy. *AIP Conference Proceedings* **2001**, *577*, 1–20, DOI: `10.1063/1.1390175`.

Chapter 2

Methods

While the dissociative chemisorption of a homonuclear diatomic molecule on a thermally distorted surface is one of the easiest systems to describe, it is by no means *easy* to describe. This chapter will discuss the theoretical framework required to accurately describe such a system, as well as what can be learned when applying these methods. In section 2.1 the basics of treating the system quantum dynamically are discussed, expanding on Schrödinger's equation and introducing the Born-Oppenheimer approximation and the time-dependent wave packet approach. Then in section 2.2 the classical dynamics are introduced, discussing methods of bringing purely classical results closer to quantum results. In section 2.3 the static corrugation model, an approach to including surface temperature effects into the dynamics, is introduced. Finally, the approach to computing several observables, which are also available to experimentalists, is discussed in section 2.4.

2.1 Quantum dynamics

To fully describe any system at a quantum dynamical level, one has to solve the Schrödinger equation

$$\hat{H}_{tot}\Psi(\overrightarrow{q}, \overrightarrow{Q}) = E\Psi(\overrightarrow{q}, \overrightarrow{Q}), \qquad (2.1)$$

with $\overrightarrow{q}$ and $\overrightarrow{Q}$ the electronic and nuclear coordinates of the full system described by the wave function $\Psi(\overrightarrow{q}, \overrightarrow{Q})$ and energy E. Separating the electronic and nuclear parts we can write the full Hamiltonian $\hat{H}_{tot}$ describing both the

electronic and nuclear motion as

$$\hat{H}_{tot} = \hat{H}_e(\vec{q}, \vec{Q}) + \sum_n \frac{-1}{2m_n} \nabla^2_{\vec{Q}_n} \tag{2.2}$$

using atomic units. Here the Hamiltonian is separated into an electronic part ($\hat{H}_e$) depending on both the electronic and nuclear coordinates and a summation over each nucleus n with mass m_n.

To solve (2.1) we write $\Psi(\vec{q}, \vec{Q})$ as a the product of the electronic and nuclear parts of the full wave function, summed over each electronic state k

$$\Psi(\vec{q}, \vec{Q}) = \sum_k \chi_k(\vec{Q})\psi_k(\vec{q}; \vec{Q}). \tag{2.3}$$

In the following, the solution to the electronic Schrödinger equation

$$\hat{H}_e(\vec{q}, \vec{Q})\psi(\vec{q}, \vec{Q}) = V_k(\vec{Q})\psi_k(\vec{q}; \vec{Q}), \tag{2.4}$$

will be useful.

Next we substitute (2.3) in (2.1), multiplying from the left with $\psi_k^*(\vec{q}; \vec{Q})$, and integrate over $\vec{q}$, as well as applying the approximations

$$\nabla_{\vec{Q}_n}\psi_k(\vec{q}; \vec{Q}) = 0 \text{ and } \nabla^2_{\vec{Q}_n}\psi_k(\vec{q}; \vec{Q}) = 0. \tag{2.5}$$

With these steps we can set up the nuclear Schrödinger equation

$$\Big[\sum_n \frac{-1}{2m_n}\nabla^2_{\vec{Q}_n} + V_k(\vec{Q})\Big]\chi_k(\vec{Q}) = E\,\chi_k(\vec{Q}) \tag{2.6}$$

for every electronic state k. This procedure is known as the Born-Oppenheimer approximation[1], solving the full Schrödinger equation in two steps, first for the electronic wave function (2.4) and then for the nuclear wave function (2.6).

To now describe a molecule interacting with a surface, we will assume that the surface atoms are completely fixed and, more importantly, that the system is in its ground electronic state. This allows us to further simplify (2.6) to

$$\Big[\sum_n \frac{-1}{2m_n}\nabla^2_{\vec{\rho}_n} + V(\vec{\rho})\Big]\chi(\vec{\rho}) = \hat{H}_{nuc}(\vec{\rho})\,\chi(\vec{\rho}) = E_{tot}\,\chi(\vec{\rho}) \tag{2.7}$$

where $\vec{\rho}$ describes the nuclear coordinates of just the molecule. Here $\hat{H}_{nuc}(\vec{\rho})$ describes the Hamiltonian for just the nuclear motion of this molecule and $\chi(\vec{\rho})$ the wave function for nuclear motion. $V(\vec{\rho})$ describes the corresponding ground

state potential energy surface (PES), the potential energy of the molecule for all nuclear coordinates.

For simplicity's sake the nuclear coordinates of the molecule ($\overrightarrow{\rho}$) are split into two parts: the centre-of-mass (c.m.) coordinates $\overrightarrow{R} = (X, Y, Z)$ and the internal coordinates of the system $\overrightarrow{r}$. We can now rewrite the nuclear Hamiltonian (2.7) as

$$\hat{H}_{nuc}(\overrightarrow{\rho}) = \hat{H}_{nuc}(\overrightarrow{r}, \overrightarrow{R}) = -\frac{1}{2M}\nabla^2_{\overrightarrow{R}} - \frac{1}{2\mu}\nabla^2_{\overrightarrow{r}} + V(\overrightarrow{r}, \overrightarrow{R}) \qquad (2.8)$$

with M and μ respectively the total mass and reduced mass of the molecule.

For convenience we will now also split the Laplace operator for the internal degrees-of-freedom (DoF) into two parts, a vibrational and a rotational part. Furthermore, to make the equation specific to a diatomic molecule scattering from a static surface we will express the internal degrees of freedom $\overrightarrow{r}$ in the form of the distance between the two atoms (r), and the orientation of this molecular bond relative to the surface and the surface normal, respectively, given by θ and ϕ (see figure 2.1). This yields the full Hamiltonian of our diatomic molecule interacting with the surface:

$$\hat{H}_{nuc}(\overrightarrow{r}, \overrightarrow{R}) = -\frac{1}{2M}\nabla^2_{\overrightarrow{R}} \underbrace{-\frac{1}{2\mu}\frac{\partial^2}{\partial r^2}}_{\hat{H}_{vib}} \underbrace{-\frac{\hat{j}^2}{2\mu r^2}}_{\hat{H}_{rot}} + V(\overrightarrow{r}, \overrightarrow{R}). \qquad (2.9)$$

Here $\hat{j}$ represents the angular momentum operator, associated with the angular momentum of the diatomic molecule.

2.1.1 Solving the electronic Schrödinger equation

Density functional theory

To obtain a reasonable accurate representation of the calculated $V(\overrightarrow{r}, \overrightarrow{R})$ of (2.9), we turn towards density functional theory (DFT) due to its ability to efficiently solve the electronic structure problem within the Born-Oppenheimer approximation [see (2.4)]. Hohenberg and Kohn[2] in 1964 showed that for a system of electrons in an external potential the ground state energy is a unique, but unknown, functional of the electron density [$n(\overrightarrow{Q}, \overrightarrow{s})$], which depends on coordinates of both the nuclei (which provide the external field) and of the electrons ($\overrightarrow{s}$). Subsequently, Kohn and Sham[3] suggested an approach to obtaining the kinetic energy of the electrons, one of the main issues with DFT at the time, by redefining the problem to the form of a fictitious system of
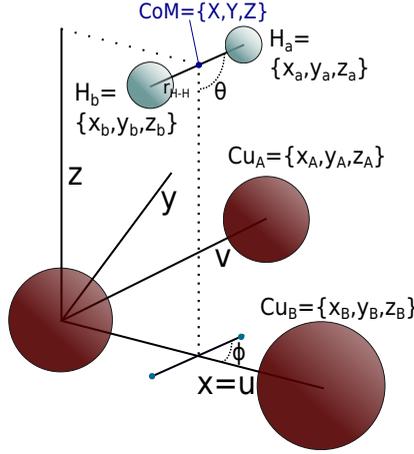
FIGURE 2.1: Coordinate system of our incoming H_2 (light-blue) with lattice vectors for the Cu(111) surface slab (dark red). The 6 DoF of the incoming H_2 molecule are described both in atomic coordinates $(x_a/x_b, y_a/y_b, z_a/z_b)$ and molecular, center-of-mass (c.m.) coordinates (X, Y, Z), with the H-H distance r_{H-H}, the polar angle θ and the azimuthal angle ϕ relative to the x-axis. The surface atoms are described using only atomic coordinates (x_I, y_I, z_I).

non-interacting electrons in an effective external potential. This allows one to rewrite the many electron problem as a set of N single-electron equations

$$\Big[-\frac{\nabla^2_{\vec{s}}}{2} + V_{KS}(\overrightarrow{Q}, \overrightarrow{s}) \Big] \phi_i(\overrightarrow{Q}, \overrightarrow{s}) = \epsilon_i(\overrightarrow{Q}) \phi_i(\overrightarrow{Q}, \overrightarrow{s}) \qquad (2.10)$$

with $\phi_i(\overrightarrow{Q}, \overrightarrow{s})$ equal to the Kohn-Sham orbital of i at given coordinates $(\overrightarrow{Q})$ of the nuclei of the system. The first term should be well recognisable as the operator describing the kinetic energy of the electrons of the system, the second term, the Kohn-Sham potential, can be further split into three terms:

$$V_{KS}(\overrightarrow{Q}, \overrightarrow{s}) = V_{ext}(\overrightarrow{Q}, \overrightarrow{s}) + V_H(\overrightarrow{Q}, \overrightarrow{s}) + V_{xc}(\overrightarrow{Q}, \overrightarrow{s}) \qquad (2.11)$$

where V_{ext} represents the external potential brought about by the positions of the nuclei, and V_H is a simple Hartree potential, given by

$$V_H(\overrightarrow{Q}, \overrightarrow{s}) = \int \frac{n(\overrightarrow{Q}, \overrightarrow{s}')}{|\overrightarrow{s} - \overrightarrow{s}'|} \mathrm{d}\overrightarrow{s}'. \qquad (2.12)$$

Finally the third, and perhaps most interesting, exchange-correlation term V_{xc} corrects the error made in V_H when it is combined with a system of fictitious

Kohn-Sham orbitals. It can be defined as

$$V_{xc}(\overrightarrow{Q}, \overrightarrow{s}) = \frac{\delta E_{xc}[n(\overrightarrow{Q}, \overrightarrow{s})]}{\delta n(\overrightarrow{Q}, \overrightarrow{s})}, \tag{2.13}$$

i.e., as the functional derivative of the exchange-correlation energy (E_{xc}) to the electron density (n).

Unfortunately, an exact expression for a universal exchange-correlation density functional (XC-DF) is not known, although many ways of approximating this functional do exist. These approaches come associated with varying levels of complexity and costs, which can be arranged conceptually on the rungs of what is known as Jacob's ladder[4]. For this thesis, we will only concern ourselves with one of the simpler approximations known as the generalized gradient approximation (GGA)[5]. Here the exchange-correlation energy (for specific coordinates of the nuclei) is written as not only a function of the electron density (n), but also its gradient (∇n):

$$E_{xc}[(n(\overrightarrow{s}), \nabla n(\overrightarrow{s})] = \int f_{xc}[n(\overrightarrow{s}), \nabla n(\overrightarrow{s})]\mathrm{d}\overrightarrow{s}. \tag{2.14}$$

Specific reaction parameter approach to DFT

One semi-empirical method for finding an accurate XC-DF used in this work is the specific reaction parameter (SRP) approach, originally proposed by Truhlar and co-workers[6, 7]. In the SRP approach, experimentally available parameters of a reaction are fitted to results obtained using a linear combination of two different exchange-correlation functionals with a mixing parameter α. The semi-empirical functional, for optimal value of α, is then used to calculate parameters of a different experimental data set, where the agreement with this new data set determines the quality of the SRP-DF. Dìaz *et al.*[8, 9] extended this approach to gas-surface scattering reactions, where the SRP was originally fit to molecular beam dissociative chemisorption experiment of H_2 and D_2 on Cu(111). Here the SRP-DF was considered a true SRP-DF if it could also reproduce the experimental results of other key experiments, such as the rovibrationally inelastic scattering probabilities, to within "chemical accuracy" (1 kcal/mol). Another important topic is the transferability of an SRP-DF, its ability to accurately describe closely related systems the SRP-DF was not originally fit for. An SRP-DF originally fitted for the CH_4/Ni(111) system[10] was, for example, found to reproduce results for the CH_4/Pt(111) system to within chemical accuracy[11].

2.1.2 Potential energy surface fitting

DFT strikes a good balance between accuracy and computational speed when compared to other first-principles methods and when considering small molecules interacting with a surface. Nevertheless, it is not nearly fast enough to calculate the energies of all the different configurations needed for full quantum dynamical simulations of the six-dimensional systems that are discussed in future chapters. Furthermore, the costs associated with a single DFT calculation are large enough that even classical dynamics becomes challenging in direct dynamics mode when one is interested in investigating (dynamically) rare events. Therefore many interpolation, or fitting, schemes have been suggested over the years, which are designed to (efficiently) interpolate between and fit to different DFT data points. These can range from simple force-field fits such as the LEPS procedure[12, 13] to more advanced high-dimensional neural network approaches such as that proposed by Behler and Parinello[14, 15]. In this thesis, I will only concern myself with a third method, originally proposed by Busnengo *et al.*, and called the corrugation reducing procedure (CRP)[16]. In the CRP, the energetic corrugation of the full 6D PES of a diatomic molecule AB approaching a surface is reduced by subtracting the individual atomic contributions, such that one obtains a smooth 6D interpolation function:

$$I^{6D}(\overrightarrow{r}, \overrightarrow{R}) = V^{6D}(\overrightarrow{r}, \overrightarrow{R}) - V_A^{3D}(\overrightarrow{q_A}) - V_B^{3D}(\overrightarrow{q_B}) \qquad (2.15)$$

with $\overrightarrow{q_A}$ and $\overrightarrow{q_B}$ the coordinates of atom A and B. It is assumed that this 6D interpolation function can be made to be smooth, and thus easy to interpolate, which reduces the amount of DFT data points required to obtain a decent fit. Obtaining the 3D atomic contributions to the full potential is again done the same way, but now yielding a 3D interpolation potential

$$I_A^{3D}(\overrightarrow{q_A}) = V_A^{3D}(\overrightarrow{q_A}) - \sum_{n=1}^{N} V_A^{1D}(r_{An})$$
$$I_B^{3D}(\overrightarrow{q_B}) = V_B^{3D}(\overrightarrow{q_B}) - \sum_{n=1}^{N} V_B^{1D}(r_{Bn}) \qquad (2.16)$$

where V_A^{1D} (V_B^{1D}) is generally chosen according to the Z-dependence of the potential of atom A (B) directly above the top site of surface atom n, with r_{An} (r_{Bn}) equal to the distance between the two, and N the total number of surface atoms.

Combining (2.15) and (2.16), we can now write our full 6D, CRP interpolated, potential as

$$V^{6D}(\overrightarrow{r}, \overrightarrow{R}) = I^{6D}(\overrightarrow{r}, \overrightarrow{R}) + I^{3D}(\overrightarrow{q_A}) + I^{3D}(\overrightarrow{q_B}) + \sum_{n=1}^{N} \left[V_A^{1D}(\overrightarrow{r_{An}}) + V_B^{1D}(\overrightarrow{r_{Bn}}) \right].$$
(2.17)

By considering the symmetry of both the incoming diatomic and the (periodic) surface slab, the computational effort to obtain enough DFT data points can be further reduced. For a homo-nuclear diatomic molecule one can further reduce the computational load by setting $I_A^{3D} = I_B^{3D}$ and $V_A^{1D} = V_B^{1D}$.

2.1.3 Solving the nuclear Schrödinger equation

Having found a solution for the electronic part (2.4), the next step in solving the full Schrödinger equation using the Born-Oppenheimer approximation is solving the nuclear part (2.6). Assuming a static surface, with all atoms in their electronic ground state, this means solving (2.7) with the Hamiltonian as described in (2.8). For chapters 4, 5 and 6 in this thesis, this will be done using the time-dependent wave packet (TDWP) approach[17].

Time-dependent wave packet approach

Using the time-dependent Schrödinger equation

$$i\frac{\partial \Psi(t)}{\partial t} = \hat{H}\Psi(t),$$
(2.18)

in atomic units, one can find a formal solution for any time-independent Hamiltonian in the form of

$$\Psi(t = t_f) = \underbrace{e^{-i\hat{H}t_f}}_{\hat{U}(t_f)} \Psi(t = 0).$$
(2.19)

Here $\hat{U}(t_f)$ is commonly known as the time-evolution operator.

Combining (2.19) with our nuclear Hamiltonian in (2.9), one can write the final wave function $\Psi(t_f)$ as a superposition of stationary scattering states $\chi(E; \overrightarrow{r}, \overrightarrow{R})$ which form solutions for (2.7):

$$\Psi(t = t_f; \overrightarrow{r}, \overrightarrow{R}) = \int_{-\infty}^{\infty} \chi(E; \overrightarrow{r}, \overrightarrow{R}) \cdot e^{-iEt_f} \, dE$$
(2.20)

or when Fourier transformed as:

$$\chi(E; \overrightarrow{r}, \overrightarrow{R}) = \frac{1}{2\pi} \int_{-\infty}^{\infty} \Psi(t; \overrightarrow{r}, \overrightarrow{R}) \cdot e^{iEt} \, \mathrm{d}t. \tag{2.21}$$

The initial wave-packet

As the initial wave-packet describing the incoming molecule will be far away from the surface, well out of the interaction range with the surface, it is convenient to split the full (6D) potential into two parts:

$$V(\overrightarrow{r}, \overrightarrow{R}) = V_{gas}(\overrightarrow{r}) + V_{int}(\overrightarrow{r}, \overrightarrow{R}). \tag{2.22}$$

Here the gas-phase part of the potential (V_{gas}) is independent of the c.m. coordinates relative to the surface, while the interaction part (V_{int}) purely describes the interaction with the surface. Now combining this with (2.9), we can rewrite the Hamiltonian for the molecule in the gas-phase

$$\lim_{Z \to \infty} \hat{H}_{nuc}(\overrightarrow{r}, \overrightarrow{R}) = \hat{H}_{gas}(\overrightarrow{r}, \overrightarrow{R}) = -\frac{1}{2M} \nabla_{\overrightarrow{R}}^2 + \hat{H}_{vib} + \hat{H}_{rot} + V_{gas}(\overrightarrow{r}) \tag{2.23}$$

where the c.m. coordinates are now only included in the Laplacian for the molecule.

With this separation we now get the eigenfunctions of the gas-phase Hamiltonian ($\hat{H}_{gas}$) as the product of a plane-wave in $\overrightarrow{R}$ and the wave function describing the internal motion of the molecule, expressed by the rovibrational eigenstates of the diatomic molecule κ ($\Phi_\kappa(\overrightarrow{r})$):

$$\hat{H}_{gas}(\overrightarrow{r}, \overrightarrow{R}) \big[e^{i\overrightarrow{k_0}\overrightarrow{R}} \cdot \Phi_\kappa(\overrightarrow{r}) \big] = \big(E_{kin}(\overrightarrow{k_0}) + E_\kappa \big) \big[e^{i\overrightarrow{k_0}\overrightarrow{R}} \cdot \Phi_\kappa(\overrightarrow{r}) \big] \tag{2.24}$$

with $E_{kin}(\overrightarrow{k_0})$ the kinetic energy of the molecule corresponding to its momentum vector $\overrightarrow{k_0} = (k_0^x, k_0^y, k_0^z)$, and E_κ the eigen energy of rovibrational state κ.

By including a linear superposition of plane-waves in the Z-direction (normal to the surface), we can now construct our full initial wave-packet

$$\Psi(t = 0; \overrightarrow{r}, \overrightarrow{R}) = \Phi_\kappa(\overrightarrow{r}) \cdot e^{ik_0^X X} \cdot e^{ik_0^Y Y} \cdot \int_{-\infty}^{\infty} b(k_0^Z) e^{ik_0^Z Z} \, \mathrm{d}k_0^Z \tag{2.25}$$

with $b(k_0^Z)$ a Gaussian shaped momentum distribution of the form

$$b(k_0^Z) = \left(\frac{2\sigma^2}{\pi} \right)^{\frac{1}{4}} \exp[-2\sigma(k_{av} - k_0^Z)^2 + i(k_{av} - k_0^Z)Z_0]. \tag{2.26}$$

Here k_{av} describes the average momentum described by the Gaussian, with a half-width parameter σ and centered around the initial coordinate in Z (Z_0). By appropriately choosing these parameters, a wave-packet can be constructed that describes molecules in an initial rovibrational state κ moving towards the surface with a range of incidence energies. Care should be taken to ensure no positive momentum (away from the surface) is included in the initial wave-packet.

Representing the wave-packet

In the collocation method, which is described in more detail in [17] and [18], the wave function [$\Psi(\overrightarrow{r})$] is approximated by a set of N linearly independent basis functions [$f_n(\overrightarrow{r})$], and expansion coefficients [c_n]

$$\Psi(\overrightarrow{r}) \approx \sum_{n=1}^{N} c_n f_n(\overrightarrow{r}). \tag{2.27}$$

By defining the wave function only at specific grid points [$\Psi_i = \Psi(\overrightarrow{r}_i)$], this can be rewritten to

$$\Psi_m = \sum_m F_{m,n} c_n \tag{2.28}$$

with $F_{m,n} = f_n(\overrightarrow{r}_m)$, which we can also rewrite to

$$\overrightarrow{\Psi} = \mathbf{f}\,\overrightarrow{c}. \tag{2.29}$$

Here $\mathbf{f}$ describes an N-dimensional square matrix that transforms the coefficient vector $\overrightarrow{c}$, known as the finite basis representation[19, 20], into the wave function as defined on the grid points $\overrightarrow{\Psi}$, generally referred to as the discrete variable representation (DVR)[21, 22]. This technique is especially powerful as one can use cleverly chosen basis functions (f_n) such that one can describe actions of non-local operators [$\hat{O}(\overrightarrow{r})$] on the full wave function [$\Psi(\overrightarrow{r})$] in ways that are computationally very efficient.

Fourier representation

One such form for the basis functions f_n is that of the plane-wave functions (e^{ikr}), as used in section 2.1.3, to define the wave-packet along the lattice vectors[17]. Similarly they are used in the Fourier grid Hamiltonian method, discussed later in section 2.2.1. Plane-waves are especially interesting as they are eigenfunctions of the Laplacian with fairly simple eigenvalues $-k^2$ and they are mutually orthogonal for a series of N equally spaced discrete points[22].

Furthermore, their transformation matrix has the elements $\mathbf{f}_{mn} = e^{\frac{2i\pi mn}{N}}$, which when applied perform a Fourier transform from the coordinate space in r_n to the momentum space k_m. This is particularly convenient due to the availability of well-scaling fast Fourier transform (FFT) routines[23, 24], as switching between the coordinate and momentum space as needed allows for very efficient time propagation of the wave function (ψ), which we will see in the next section.

Several other representations used as shown in (2.25) will not be discussed. Instead the reader is referred to Ref. [22] which describes each of them in detail.

Propagating the wave-packet

With the initial wave-packet as written in (2.25), (2.19) can now be used to propagate the wave function forward in time. For the chapters 4, 5 and 6, this was done using the split-operator (SPO) method as described by Feit, Fleck and Steiger[25]:

$$\Psi(t_0 + \Delta t; \overrightarrow{r}, \overrightarrow{R}) = \exp\left[-\frac{i}{2}\hat{K}(\overrightarrow{r}, \overrightarrow{R})\Delta t\right] \exp\left[-\frac{i}{2}\hat{H}_{rot}(\overrightarrow{r})\Delta t\right] \quad (2.30)$$
$$\exp\left[-i\hat{V}(\overrightarrow{r}, \overrightarrow{R})\Delta t\right] \ \exp\left[-\frac{i}{2}\hat{H}_{rot}(\overrightarrow{r})\Delta t\right]$$
$$\exp\left[-\frac{i}{2}\hat{K}(\overrightarrow{r}, \overrightarrow{R})\Delta t\right] \Psi(t_0; \overrightarrow{r}, \overrightarrow{R}) + O[(\Delta t)^3],$$

with $\hat{K}(\overrightarrow{r}, \overrightarrow{R}) = -\frac{1}{2M}\nabla^2_{\overrightarrow{R}} + \hat{H}_{vib}(\overrightarrow{r})$. With this step wise propagation, first a half-step is done for the free particle propagation, followed by a separate half-step for the rotation of the molecule, and then the full action of the external potential. Subsequently another half-step is done for the rotation and finally the other half-step of the free particle. By transforming between the momentum space (for $\hat{K}$) and the coordinate space (for $\hat{V}$), each of these steps can be very efficiently applied as a multiplication, as was introduced in section 2.1.3. The rotation of the molecule will have to be treated separately, as it contains both potential (in r) and kinetic elements in the spherical coordinate system we use.

However, due to this symmetrical splitting and the non-commutativity of $\hat{K}$ and $\hat{V}$ an error is accumulated in the order of $O[(\Delta t)^3]$, with[17]

$$\text{err} \approx \max\left(-i\frac{\Delta t^3}{8}[\hat{V}, [\hat{V}, \hat{K}]], -i\frac{\Delta t^3}{8}[\hat{K}, [\hat{K}, \hat{V}]]\right). \quad (2.31)$$

Therefore, while very convenient as a time propagation procedure, care should be taken to not take too large time steps, as we will see in chapters 5 and 6.

Analysing the wave-packet

To obtain scattering probabilities from the wave packet during propagation, scattering matrix (S-matrix) elements are calculated using the scattering matrix amplitude formalism of Balint-Kurti and co-workers[26, 27]. Although this approach was originally designed for gas-phase scattering, it was adapted to work with surfaces as well[28]. The S-matrix elements $S_{\kappa \to \kappa' nm}(E)$ describe the (energy dependent) scattering of the diatomic in state κ, to final state κ', with the diffraction state (n,m), obtained from:

$$S_{\kappa \to \kappa' nm}(E) = \delta_{n,0} \delta_{m,0} \delta_{\kappa',\kappa} \cdot \mathrm{e}^{-2ik_0^Z Z_{ana}} \tag{2.32}$$
$$- \frac{\mathrm{e}^{-2ik_{\kappa' nm}^Z Z_{ana}}}{Mb(-k_0^Z)} \left(\frac{k_0^Z k_{\kappa' nm}^Z}{2\pi} \right)^{\frac{1}{2}} A_{\kappa' nm}^{Z_{ana}}(E)$$

with

$$A_{\kappa' nm}^{Z_{ana}}(E) = \int_0^\infty C_{\kappa' nm}^{Z_{ana}}(t) \cdot \mathrm{e}^{iEt} \, \mathrm{d}t, \tag{2.33}$$

the coefficients $C_{\kappa' nm}^{Z_{ana}}(t)$ are given by

$$C_{\kappa' nm}^{Z_{ana}}(t) = \left\langle \frac{\mathrm{e}^{i(k_0^X + n\frac{2\pi}{L_X})X + i(k_0^Y + n\frac{2\pi}{L_Y})Y}}{(L_X L_Y)^{\frac{1}{2}}} \cdot \Phi_{\kappa'}(\overrightarrow{r}) \middle| \Psi(t; \overrightarrow{r}, \overrightarrow{R})|_{Z=Z_{ana}} \right\rangle \cdot \tag{2.34}$$

$C_{\kappa' nm}^{Z_{ana}}(t)$ describe the scattered wave function projected onto the rovibrational states of the free molecule and the molecular diffraction states at the analysis line in Z_{ana}, with L_X and L_Y the length of the surface unit cell. The first term on the right-hand side of (2.32) is included to cancel the contribution of the incident wave function to the time integral of (2.33). The state-to-state scattering probabilities $[P_{\kappa \to \kappa' nm}(E)]$ can now be computed at a specific incidence energy (E) using

$$P_{\kappa \to \kappa' nm}(E) = |S_{\kappa \to \kappa' nm}(E)|^2. \tag{2.35}$$

The reaction probability for an initial rovibrational state κ, at incidence energy E, is computed simply as

$$P_{reac}^\kappa(E) = 1 - \sum_{\kappa' nm} P_{\kappa \to \kappa' nm}(E). \tag{2.36}$$

The total reaction probability is given as 1 minus the sum of the scattering probabilities $P_{\kappa \to \kappa' nm}$.

Another method of obtaining the reaction probability is the reactive flux analysis method. Here we define a flux

$$\rho(E;\kappa;\overrightarrow{R},\theta,\phi) = \frac{2\pi M}{|k_z|\mu} \cdot Im\left[\chi^*(E;\overrightarrow{R},r_{ana},\theta,\phi) \cdot \frac{\partial \chi(E;\overrightarrow{R},r_{ana},\theta,\phi)}{\partial r}\right]\Big|_{r=r_{ana}}$$

(2.37)

through a specific plane given by $r = r_{ana}$[29–31]. By integrating over the other degrees-of-freedom ($\overrightarrow{R}$, θ, ϕ), one can obtain the reaction probability for a specific energy E, and rovibrational state κ, assuming the plane in r at r_{ana} was properly placed in the exit channel of the PES. Furthermore, one can also integrate over only portions of X and Y, yielding site-specific reaction probabilities[32].

Absorbing the wave-packet

Once a part of the wave function has reacted or scattered and it has been analysed, it is computationally helpful to completely remove it from the grid. This will remove the storage requirements for the wave function in large Z (and r) and therefore reduce the total amount of memory needed. By including an imaginary potential $V_{opt} = -iV_{quad}(Z)$ into the potential operator $\hat{V}$ of (2.9) the wave-packet can be absorbed on the grid after passing the analysis plane in Z_{ana}. Here V_{quad} is a purely real function of Z, with the quadratic form

$$V_q(Z) = \begin{cases} A\left(\dfrac{Z - Z_{min}}{Z_{max} - Z_{min}}\right)^2 & \text{for} \quad Z_{min} < Z < Z_{max} \\ 0 & \text{for} \quad Z < Z_{min} \end{cases}.$$

(2.38)

Z_{min} is best chosen to be a grid point right after the analysis line, while Z_{max} is simply the end of the grid. A similar complex absorbing potential (CAP) is constructed on the grid in r, a few grid points behind the analysis line at r_{ana} if it is included.

2.2   Classical dynamics

Instead of constructing a wave-packet and propagating it in time using our PES, which is obtained by solving the electronic Schrödinger equation (2.4) using DFT, one can also turn to much simpler classical dynamics. Here the dynamics of the molecule interacting with the surface is described purely as that of a (point) particle moving through the potential field. Turning to classical mechanics, the expressions most suited for the works in this thesis are those

derived by Hamilton from the Langrangian equations

$$\frac{\mathrm{d}\overrightarrow{q}}{\mathrm{d}t} = \frac{\partial H}{\partial \overrightarrow{p}} \quad \text{and} \quad \frac{\mathrm{d}\overrightarrow{p}}{\mathrm{d}t} = -\frac{\partial H}{\partial \overrightarrow{q}}, \tag{2.39}$$

where $\overrightarrow{q}$ and $\overrightarrow{p}$ describe respectively the coordinates and momentum vector of the system, and H is the classical Hamiltonian. Thus by choosing a suitable Hamiltonian and finding its partial derivatives with respect to to the coordinates, one can find the change in momentum in time. The Hamiltonian describing each atom separately takes on the form of a kinetic part T and a potential part V with

$$H(\overrightarrow{q}, \overrightarrow{p}) = \underbrace{\frac{\overrightarrow{p}^2}{2m}}_{T} + V(\overrightarrow{q}), \tag{2.40}$$

where the kinetic part depends only on the momenta of each of the particles ($\overrightarrow{p}$), while the potential part only depends on the coordinates of the particles ($\overrightarrow{q}$), see for example also (2.8) which has the same components. Combining (2.39) and (2.40), we find that we can express the change in the position in time (also known as the velocity v) as

$$\frac{\mathrm{d}\overrightarrow{q}}{\mathrm{d}t} = \frac{\partial T}{\partial \overrightarrow{p}} = \frac{\overrightarrow{p}}{m} = \overrightarrow{v} \tag{2.41}$$

while the change in momentum over time is described by

$$\frac{\mathrm{d}\overrightarrow{p}}{\mathrm{d}t} = -\frac{\partial V(\overrightarrow{q})}{\partial \overrightarrow{q}}, \tag{2.42}$$

or in words by the negative of the gradient of the potential relative to the coordinates, for our system described by the PES. In Newtonian mechanics one similarly defines the force $\overrightarrow{F}$ as the change in momentum over time which, assuming $\overrightarrow{p} = m\overrightarrow{v}$ with a constant mass m, can be rewritten to

$$\overrightarrow{F} = \frac{\mathrm{d}\overrightarrow{p}}{\mathrm{d}t} = m\frac{\mathrm{d}\overrightarrow{v}}{\mathrm{d}t} = m\overrightarrow{a}, \tag{2.43}$$

with $\overrightarrow{a}$ equal to the acceleration. This is commonly known as Newton's second law of motion.

2.2.1   Quasi-classical dynamics

To better reproduce the quantum dynamical behaviour using purely classical dynamics, one can also turn to *quasi*-classical dynamics (QCD). While the molecules here are treated fully classical, initial energies and momenta are chosen in such a way that they correspond to those one would expect from a quantum dynamical approach. In this thesis, initial rovibrational energies are determined using the Fourier grid Hamiltonian (FGH) method, as outlined by Marston and Balint-Kurti[33]. It relies on discretizing the coordinate space, for this work the gas-phase potential of the diatomic molecule, and then solving the Schrödinger equation and obtaining the eigen energies for the different rovibrational states. It makes use of a fast Fourier transform (FFT)[23, 24] to compute the Hamiltonian matrix, as the kinetic energy term is easier computed in momentum space (see section 2.1.3). This Hamiltonian matrix is subsequently diagonalised.

2.2.2   Initial state selection

The initial position of the diatomic molecule's c.m. is chosen uniformly between 0 and a along the lattice vectors $u[= x - y/\sqrt{3}]$ and $v[= 2y/\sqrt{3}$ for the (111) surface slab], with a the lattice constant of the surface slab. The diatomic molecule is placed far enough away from the surface in Z to be considered in the gas-phase (in this thesis always at least 7 Å). Initial vibrational distances and momenta (in r) are obtained through a constant time step propagation for one full vibrational cycle of the molecule in the gas-phase, which yields the quasi-classical distribution of these parameters. The molecular angles relative to the surface, θ and ϕ (see 2.1), are randomly chosen from a uniform distribution on the sphere with $\cos(\theta)$ from -1 to 1 and ϕ from 0 to 2π, respectively. Only calculations for single initial vibrational (v) and rotational (J) states are used for the chapters in this thesis. Internal angular velocities are chosen according to the quantized angular momentum $L^2 = J(J+1)\hbar^2$, while the angle θ_L between the angular momentum vector and the surface normal is constrained by $\theta_L = \pi$ for $J = 0$ and $\cos(\theta_L) = m_J/\sqrt{J(J+1)}$ if $J \neq 0$, where J is the initial rotational state of the molecule. The initial rotational m_J states are chosen with equal probability between $-J$ and J, with the number of quasi-classical trajectories increased to ensure each m_J state is sampled the same amount of times.

2.2.3 Integration methods

Bulirsch-Stoer

With the initial state selected, the system is propagated forward in time using the Bulirsch-Stoer (BuS) predictor-corrector algorithm[34], according to (2.39) and (2.40). The BuS algorithm combines the Richardson extrapolation[35] and the modified mid-point method to accurately estimate solutions to ordinary differential equations, such as (2.39), while not providing very large computational loads. Here one first chooses some large time step B, which is then subdivided into smaller time step steps b_n. Using Richardson extrapolation and starting from the initial position vector $\overrightarrow{x}(t)$, the new positions $[\overrightarrow{x}(t+B)]$ are estimated by determining the position values for each $\overrightarrow{x}(t+b_n)$, fitting to some analytical form, and then extrapolating to infinitely small sub time steps ($b_n \rightarrow 0$, $n \rightarrow \infty$). Initially starting with two substeps and using rational functions to fit, the BuS algorithm continues to add two more substeps until the extrapolation to infinite substeps is found to have a small enough error to be considered accurate, or a maximum number of iterations (i_{max}) is passed (in this thesis $i_{max} = 9$). If the desired accuracy is not reached within i_{max} iterations, B is halved and the entire sequence is repeated. If the desired accuracy is achieved, a new B can also be estimated based on the number of iterations needed. For this thesis, $B_{new} = 1.5B$ was used when the integration was completed within 6 iterations, or $B_{new} = 0.6^{i-6} \cdot 1.5B$ when it was not.

Velocity-Verlet

Another integration method used in chapter 3 is the velocity-Verlet (VV) algorithm, first described by Verlet[36]. In this simple three step algorithm, one first advances the velocities of the system for half a time step Δt using

$$\overrightarrow{v}(t + \frac{\Delta t}{2}) = \overrightarrow{v}(t) + \overrightarrow{a}(t)\frac{\Delta t}{2},$$
(2.44)

then the positions are advanced the full time step:

$$\overrightarrow{x}(t + \Delta t) = \overrightarrow{x}(t) + \overrightarrow{v}(t + \frac{\Delta t}{2}),$$
(2.45)

and then finally the second half-step is computed, using a new acceleration $\overrightarrow{a}$ obtained from the potential at the new positions $x(t + \Delta t)$:

$$\overrightarrow{v}(t + \Delta t) = \overrightarrow{v}(t + \frac{\Delta t}{2}) + \overrightarrow{a}(t + \Delta t)\frac{\Delta t}{2}.$$
(2.46)

2.2.4   Final state binning

For the trajectories in this thesis, propagation ends when the two atoms move more than a specific distance apart from each other, or when Z is large enough that the molecule can be considered to be in the gas-phase again. As the focus of this thesis will be on H_2 and D_2, these parameters are set to 2.25 Å and 7 Å for the r and Z distances, respectively. The final rovibrational state of the diatomic molecules that are scattered can be determined using several simple binning methods. First the modulus of the classical angular momentum ($|L_f|$) is calculated according to

$$|L_f|^2 = p_\theta{}^2 + \frac{p_\phi{}^2}{\sin^2 \theta} \tag{2.47}$$

where p_θ and p_ϕ describe the momenta conjugate to θ and ϕ which describe the orientation of the molecule relative of the surface (see Fig. 2.1). This angular momentum is then used to determine a classical "rotational state"

$$J_f = \frac{\sqrt{1 + 4|L_f|^2} - 1}{2} \tag{2.48}$$

which is found by equating $|L_f|^2$ to $J(J+1)$.

Next this classical state is binned using one of three methods, with the floor and weighted methods only used in chapter 5. Using the standard binning method, which is how the binning was generally performed in the previous SCM studies, the rotational state is binned to the closest allowed J state, keeping in mind the selection rule for the rotational state of our diatomic molecule: $\Delta J = \pm 2$. With the weighted binning method the integer rotational state closest to J_f is chosen and given a weight of $W_i = 2$ when it is allowed or $W_i = 0$ when it is not allowed, with i for the ith trajectory performed[37]. This approach effectively ignores any trajectory with a disallowed transition while counting those scattered trajectories with allowed final rotational states twice. As a consequence this method will significantly affect reaction and scattering probabilities if the final rotational states of the scattered molecules are not evenly distributed between the allowed and disallowed states. Finally, with the floor binning method the classical rotational state J_f is rounded downwards towards the first allowed J state, keeping in mind the selection rule. For both the standard and floor binning, $W_i = 1$ is always chosen for every trajectory. A weight of $W_i = 1$ is also used for the reacted trajectories of the weighted binning method.

With the rotational state (J) determined, the vibrational state (v) is chosen by finding the rovibrational state which is closest in total rovibrational energy to the states allowed by the binned rotational state. Trajectories are considered rovibrationally elastically scattered when the final rovibrational state of diatomic molecule is binned to the same state as its initial state, and rovibrationally inelastically when the binned final state is not the same as the initial rovibrational state. The m_J state is not taken into account at all for the final state, as it is degenerate with the other possible m_J states within the same (v, J) level.

Reaction (and scattering) probabilities are finally determined by

$$P_{reac} = \frac{\sum\limits_{reacted} W}{\sum\limits_{total} W} \tag{2.49}$$

with W being the weight of each individual trajectory. For the standard and floor binning methods, this procedure amounts to dividing the number of reacted (or scattered) trajectories by the total number of trajectories performed.

2.3 Potentials for surface displacements

2.3.1 Static corrugation model

The static corrugation model (SCM) was designed to include surface temperature effects due to surface atom displacement on the BOSS dynamics of reactive scattering. This is achieved by expanding the description of the PES into three terms[38], with the first one being the the potential for the ideal, static surface: $V_{DFT}(\overrightarrow{q}_{id}, \overrightarrow{r})$. The two additional terms V_{strain} and V_{coup} are included to describe the internal strain of the surface due to distortion, and the change in molecule-surface interaction due to surface atom displacement, respectively. Thus the total PES can be described using

$$V_{DFT}(\overrightarrow{q}, \overrightarrow{r}) = V_{DFT}(\overrightarrow{q}^{id}, \overrightarrow{r}) + V_{coup}(\overrightarrow{q}^{id} \to \overrightarrow{q}, \overrightarrow{r}) + V_{strain}(\overrightarrow{q}^{id} \to \overrightarrow{q}) \tag{2.50}$$

where $\overrightarrow{q}$ describes the positions of all surface atoms, $\overrightarrow{q}_{id}$ the ideal lattice positions of all surface atoms, and $\overrightarrow{r}$ the positions of the adsorbed atoms. $\overrightarrow{r}_{gas}$ describes the position of the small molecule for $Z \to \infty$, where no interaction with the surface is expected. To ensure the coupling potential describes the change in energy of *just* the molecule-surface interaction, due to the surface atoms being displaced from their ideal crystal lattice positions, the

coupling potential is fitted using

$$V_{coup}(\overrightarrow{q}^{\,id} \to \overrightarrow{q}, \overrightarrow{r}) = [V_{DFT}(\overrightarrow{q}, \overrightarrow{r}) \quad - V_{DFT}(\overrightarrow{q}^{\,id}, \overrightarrow{r})]$$
$$- [V_{DFT}(\overrightarrow{q}, \overrightarrow{r}_{gas}) - V_{DFT}(\overrightarrow{q}^{\,id}, \overrightarrow{r}_{gas})]. \tag{2.51}$$

Here the change in internal (strain) energy of the surface due these displacements is subtracted from the change in interaction energy of the molecule with the surface. This strain potential is fitted separately using

$$V_{strain}(\overrightarrow{q}^{\,id} \to \overrightarrow{q}) = V_{DFT}(\overrightarrow{q}, \overrightarrow{r}_{gas}) - V_{DFT}(\overrightarrow{q}^{\,id}, \overrightarrow{r}_{gas}) \tag{2.52}$$

and added back to the full potential in (2.50). With this formulation, the changes in interaction between the molecule and the surface, due to the displacement of surface atoms, is described separately from the changes in interaction of the surface atoms with each other.

As the name already suggests, the SCM also relies on the sudden approximation introduced in section 1.2. Here the motion of the surface atoms is assumed to be slow enough relative to the incoming diatomic molecule that the surface can be approximated as a thermally distorted, but static, surface. One further assumes that the interaction time between the molecule and the surface is short, while the mass mismatch is large, which reduces the influence of energy exchange between the molecule and the surface on the interaction. Under this assumption of a static surface V_{strain} can be neglected during dynamics, as it will be a constant value (and therefore its derivative is 0). Thus the full dimensional DFT PES for the thermally distorted system can be approximated as

$$V_{DFT}(\overrightarrow{q}, \overrightarrow{r}) \approx V_{SCM}(\overrightarrow{q}^{\,id} \to \overrightarrow{q}, \overrightarrow{r}) = V_{DFT}(\overrightarrow{q}^{\,id}, \overrightarrow{r})$$
$$+ V_{coup}(\overrightarrow{q}^{\,id} \to \overrightarrow{q}, \overrightarrow{r}) \tag{2.53}$$

For $V_{DFT}(\overrightarrow{q}^{\,id}, \overrightarrow{r})$ the CRP as discussed in section 2.1.2 is used, although other approaches should also allow for accurate results.

The main focus of the initial work by Wijzenbroek, Spiering and Somers was obtaining a continuous description of V_{coup} for the H_2 on Cu(111) system[38, 39]. This was achieved through interpolation of a collection of DFT data, similar to the CRP approach, and fitting this to

$$V_{coup}(\overrightarrow{r}, \overrightarrow{q}^{\,id} \to \overrightarrow{q}) = \sum_i^{\overrightarrow{r}} \sum_j^{\overrightarrow{q}} \left[V_{H\text{-}Cu}(|\overrightarrow{r_i} - \overrightarrow{q_j}|) - V_{H\text{-}Cu}(|\overrightarrow{r_i} - \overrightarrow{q_j}^{\,id}|) \right] \tag{2.54}$$

with $\vec{r}_i$ the positions of adsorbate i, and $\vec{q}_j$ the position of surface atom j and where

$$V_{H\text{-}Cu}(R) = (1 - s(R))V(R) + s(R)V(P_7) \qquad (2.55)$$

with

$$V(R) = -\mathrm{e}^{-P_4(R-P_5)} \cdot \left(\sum_{k=0}^{3} P_k(R - P_5)^k \right) \qquad (2.56)$$

and

$$s(R) = \begin{cases} 0 & \text{for } R < P_6 \\ \dfrac{1}{2}\cos\left(\dfrac{\pi(R-P_7)}{P_7-P_6}\right) + \dfrac{1}{2} & \text{for } P_6 \leq R \leq P_7 \\ 1 & \text{for } R > P_7 \end{cases} . \qquad (2.57)$$

The SCM was later expanded to include an effective three-body potential, by making each fitting parameter P_i linearly dependent on the the distance between the two adsorbates r_{H-H}:

$$P_i = \begin{cases} P_{i,a}r^{min}_{H-H} + P_{i,b} & \text{for } r_{H-H} < r^{min}_{H-H} \\ P_{i,a}r_{H-H} + P_{i,b} & \text{for } r^{min}_{H-H} \leq r_{H-H} \leq r^{max}_{H-H} \\ P_{i,a}r^{max}_{H-H} + P_{i,b} & \text{for } r_{H-H} > r^{max}_{H-H} \end{cases} . \qquad (2.58)$$

Here the cut-off values r^{max}_{H-H} and r^{min}_{H-H} are obtained from the largest and smallest values of r_{H-H}, respectively, used during the fitting procedures.

To account for thermal expansion effects while using the CRP potential of the system for an ideal lattice, the molecule's c.m. vectors are linearly contracted or stretched along the lattice vectors u and v (see Fig. 2.1). By stretching along the lattice vectors instead of the x- or y-vectors, accidental introduction of extra artificial vibrational or rotational strain is avoided. Thus the full effective SCM potential becomes

$$V_{SCM}(\vec{r}, \vec{q}, \vec{q}^{id}) = V_{CRP}(\vec{r}^{id}(\vec{r}), \vec{q}^{id})$$
$$+ \sum_i^{\vec{r}} \sum_j^{\vec{q}} \left[V_{H\text{-}Cu}(|\vec{r_i} - \vec{q_j}|) - V_{H\text{-}Cu}(|\vec{r}^{id}(\vec{r}) - \vec{q_j}^{id}|) \right]$$
$$(2.59)$$

where $\vec{r}^{id}(\vec{r})$ scales the molecular c.m. vectors along the lattice vectors[39].

Although the SCM was fitted only for the H_2/Cu(111) system, it can be easily employed to also describe other diatomics reacting on other surfaces. Here the most important aspects would be the mass mismatch and interaction time between the molecule and the surface. Both a larger mass mismatch

and a shorter interaction time would reduce the likelihood of energy exchange playing a significant role in the reaction process, increasing the validity of the sudden approximation the SCM is based on. Equations (2.50), (2.51), and (2.52) are similarly general enough to be applied to molecules of more than two atoms interacting with a thermally distorted surface, although new forms of the coupling potential would be required to obtain proper fits.

Thermally distorted surface generation

One important aspect of implementing the SCM is obtaining (accurate) representations of thermally distorted surface slabs of the surface of interest, in this thesis Cu(111). Initial work in designing the SCM achieved this through random displacements of each individual atom from its ideal lattice position, based on a bulk-like displacement uniform in the three Cartesian coordinates, in this thesis referred to as RD-SCM[38, 39]. The magnitude of this displacement is randomly selected from a Gaussian distribution with a standard deviation of

$$\sigma = \sqrt{\frac{3B}{8\pi^2}} \tag{2.60}$$

with B the surface temperature dependent Debye-Waller factor, obtained from fits to experimental inelastic neutron scattering data[40]. To also include the thermal expansion of the surface, surface atom slab positions are shifted along the lattice vectors based on an experimental thermal expansion coefficient[41]. The inter-layer distances, found in the z-direction of the slab, are taken directly from experimental results[42].

Another approach to generating these thermally distorted surface slabs is simple molecular dynamics, using some form of accurate potential, in the micro-canonical ensemble. However, care should be taken to stay above the Debye temperature of the surface when applying such a classical method (≈ 300 K for Cu). At surface temperatures below this "classical" limit the erroneous use of Maxwell-Boltzmann statistics (instead of Bose-Einstein statistics) and zero-point energy leaking, due to an applied thermostat, will influence the final surface atom positions obtained.

In Chapter 3 the generation of a database of thermally distorted surface slabs [of Cu(111)] at a modelled surface temperature of 925 K will be discussed in detail, which is then also used for the three subsequent chapters. Here an embedded-atom method (EAM) potential was used to describe the thermal surface motion, thus the approach will be referred to as the EAM-SCM.

2.3.2 Embedded-atom method

First described by Daw and Baskes in 1983[43], the EAM has been a powerful tool for theoretical surface scientists. The EAM is based on the quasiatom[44], or effective medium[45], approach which was designed to describe impurities in metals[46]. Here an impurity, such as a small atom, embedded in the metal is modelled as a particle in a uniform environment of electron density. The EAM instead takes it one step further, treating each surface atom as the "impurity" in an electron density obtained from contributions of each of the neighbouring atoms. Each atom would thus get an embedding energy, which is defined as the difference in energy between the atom inside the uniform electron density associated with its neighbours, and that of the same atom in a vacuum. The total sum of each individual atomic energy is then approximated as the total (potential) energy of the metal:

$$E_{tot} = \sum_i F_i(n_i) \tag{2.61}$$

where F_i is the so-called embedding energy of atom i, and n_i the density this atom experiences at position r_i.

This initial approach to the EAM did not perform as well as was expected, yielding unrealistic properties for solids due to the neglect of core-core repulsion and the "assumption of extreme locality"[46]. Thus a second, short-range pair interaction was added to the model to yield a total energy given by

$$E_{tot} = \sum_i \left[F_i(n_i) + \frac{1}{2} \sum_{j \neq i} \phi_{ij}(R_{ij}) \right]. \tag{2.62}$$

Here ϕ_{ij} describes the pair interaction potential between atoms i and j, R_{ij} being the distance between the two. In this work, we will use another pair interaction to approximate the density n_i experienced by atom i using

$$n_i = \sum_{j \neq i} \rho_{ij}(R_{ij}) \tag{2.63}$$

where ρ_i yields the density contribution of atom j to the density of atom i.

2.3.3 Dynamic corrugation model

While the SRP48 DFT functional, used for the Cu(111) CRP PES and the SCM coupling potential used in this thesis, has been shown to reproduce H_2 dissociation on the Cu(111) surface to within chemical accuracy[47, 48], it is

most likely not too suitable for describing bulk Cu. The EAM on the other hand is very accurate in describing the Cu system, both the bulk and the surface, itself[49]. Therefore, by combining the SCM expressions (2.50) and (2.59) with the EAM potential of (2.62), it is possible to fully describe the system including the dynamics of the surface:

$$
\begin{aligned}
V_{DCM}(\vec{r}, \vec{q}, \vec{q}^{id}) = {}& V_{CRP}(\vec{r}^{id}(\vec{r}), \vec{q}^{id}) \\
& + \sum_i^{\vec{r}} \sum_j^{\vec{q}} \left[V_{H\text{-}Cu}(|\vec{r_i} - \vec{q_j}|) - V_{H\text{-}Cu}(|\vec{r}^{id}(\vec{r}) - \vec{q_j}^{id}|) \right] \\
& + \sum_k^{\vec{q}} \left[F_k(\sum_{l \neq k}^{\vec{q}} \rho_{kl}(|\vec{q}_k - \vec{q}_l|)) + \frac{1}{2} \sum_{l \neq k}^{\vec{q}} \phi_{kl}(|\vec{q}_k - \vec{q}_l|) \right].
\end{aligned}
\tag{2.64}
$$

While this dynamic corrugation model (DCM) is much more computationally expensive, massively increasing the number of DoF of the system compared to the SCM, it also allows for energy exchange between the molecule and the surface. Furthermore, it also allows for other dynamic effects that could affect dissociation probabilities, such as a dynamic puckering effect of surface atoms moving towards the incoming H_2. As both the EAM-SCM and EAM-DCM are based on exactly the same potentials, with only one allowing the surface to move, it is also an excellent tool to investigate the (lack of) effect these additional DoF have on the many observables that can be calculated for the H_2 on Cu(111) system, some of which we will discuss in section 2.4. This then will also allow for a validation of the sudden approximation that lies at the basis of the SCM.

2.4   Computation of other observables

2.4.1   Rotational quadrupole alignment parameter

The rotational quadrupole alignment parameter (RQAP) $[A_0^{(2)}(J)]$ is a measure of preference for a diatomic molecule to dissociate in particular m_J states. If this parameter is positive, dissociating molecules prefer to react rotating parallel to the surface ($|m_J| = J$; "helicopter"), while negative values indicate a preference for reaction of molecules with a rotation perpendicular to the surface ($|m_J| = 0$; "cartwheel"). A value of 0 indicates no preference for either.

The RQAP is defined as

$$
A_0^{(2)} \equiv \langle 3\cos^2 \theta_L - 1 \rangle
\tag{2.65}
$$

with θ_L the angle between the angular momentum vector and the surface normal. It can also be computed through

$$A_0^{(2)}(v,J) = \frac{\sum_{m_J} P_{stick}(v,J,m_J)\left(\frac{3m_J^2}{J(J+1)} - 1\right)}{\sum_{m_J} P_{stick}(v,J,m_J)}, \tag{2.66}$$

with $P_{stick}(v,J,m_J)$ being the sticking probability for the specific rovibrational state.

Assuming direct inversion under detailed balance the RQAP can also be measured experimentally, although there are no studies available for the H_2 on Cu(111) system to our knowledge. Experimentally obtained RQAPs are available for the D_2/Cu(111) system[50–52].

2.4.2 Simulating time-of-flight spectra

To more directly compare to the time-of-flight (ToF) spectra obtained from the state-selective desorption experiments, we can also directly simulate ToF spectra from our dissociation curves. Mirroring the experimental approach as described in Ref. [53], we make use of direct inversion under detailed balance to directly relate the dissociative adsorption results to the ToF spectra obtained from associative desorption experiments. Here we relate the intensity of the ToF spectrum to the the sticking probability function multiplied by a flux-weighted velocity distribution expressed in the time domain, accounting for a $\frac{t'}{x_0}$ term due to the detection method used:

$$I(t')dt' = K \cdot C(t') \cdot \exp\left(\frac{-E_{kin}[t']}{2k_bT_s}\right)\left(\frac{x_0}{t'}\right)^4 \cdot P_{stick}(E_{kin}[t'])\,dt'. \tag{2.67}$$

Here k_b is the Boltzmann constant, T_s the surface temperature, K a proportionality constant, $E_{kin} = m\left(\frac{x_0}{t'}\right)^2$, and $t' = t - t_{shift}$. A cutoff function $[C(t')]$ is also included, which models the experimental decrease in ion detection efficiency as the kinetic energy decreases[54]. Here t (t_{shift}) and x_0 describe the travel time in (after leaving) the field-free region, and the length of this field-free region in the detector of the experimental setup that is being simulated, respectively. Using this expression the assumption is made that all molecules desorb parallel to the surface normal, completely neglecting any off-normal contribution to the final signal. This means we can set the kinetic energy (E_{kin}) equal to the kinetic energy normal to the surface (E_n). In Chapter 3 comparisons will be made to work where this does not hold, and instead the desorbed molecules are modelled to desorb in a cone with the surface as a base. This requires an additional term, integrating over the expected aperature of the cone and the

azimuthal angle, as well as slight modifications in the calculation of the kinetic energy E_{kin} and the length of the field-free region, which is well described in Ref. [55]. In Chapter 6 comparisons are made to the more recent experimental work of Kaufmann *et al.* on H_2, D_2, and HD, where this angular averaging can be fully neglected[54].

Two cutoff functions are used throughout this thesis. In Chapter 3 it is of a tanh form:

$$C(t') = 1 - \tanh\left(\frac{t' - t_c}{t_w}\right) \tag{2.68}$$

with t_c a cutoff parameter, and t_w a width parameter which governs how fast the signal decays, matching that of earlier work[55]. The cutoff function used in Chapter 6 is instead of an exponential form,

$$C(E_{kin}) = 1 - e^{-E_{slope}(E_{kin} - E_{min})} \text{ for } E_{kin} > E_{min}, \tag{2.69}$$

based on the kinetic energy of the molecule, as was used in a more recent experimental study[54]. The cutoff parameters E_{slope}, which governs how fast the signal decays, and E_{min}, which determines the minimal energy of the molecule needed for it to be experimentally detectable, were obtained from the same experimental study.

To simulate the ToF spectra using equation (2.67), we require a continuous representation of the dissociation curves $[P_{stick}(E_n)]$, which we obtained from fitting to several functional forms as used in chapters 3 and 6. The fitting method used was that of Levenberg-Marquardt[56, 57], as implemented in the LMFIT package[58]. The first is the error function (ERF) form

$$P_{stick}(E_n) = \frac{A}{2}\left[1 + \text{erf}\left(\frac{E_n - E_0}{W}\right)\right], \tag{2.70}$$

with A, E_0 and W equal to the saturation value, the energy at half saturation, and the width of the curve respectively. This symmetric sigmoidal function is one of the most used functional forms for fitting dissociation curves, both for theoretical and experimental works, which ensures a large amount of data to compare to.

Next comes the generalized logistic function (LGS), which is the only function used in Chapter 3:

$$P_{stick}(E_n) = \frac{A}{\left(1 + \nu \exp\left[-\frac{E-B}{C}\right]\right)^{\frac{1}{\nu}}}. \tag{2.71}$$

The LGS provides a flexible root to derive several other functional forms. Here

A is again the saturation parameter, B the effective barrier height parameter, C the width parameter, and ν a parameter which influences the symmetry of the curve. Several other functional forms can be found by picking specific values for ν, with of particular note the ordinary logistic function ($\nu = 1$) and the Gompertz function (GMP, $\nu \to 0^+$) given by

$$P_{stick}(E_n) = A \cdot \exp \left[- \exp \left(- \frac{E_n - B}{C} \right) \right], \tag{2.72}$$

where A, B and C similarly describe the saturation value, the energy at half saturation, and the width of the curve, respectively. The GMP function in particular has a very asymmetric sigmoidal form, with a much more gradual increase towards the saturation value compared to the initial curve onset.

Finally, a combination of Gompertz function and the LGS function (with $\nu = 1$), in previous studies used as the five-parameter function (FPC), is given by

$$P_{stick}(E_n) = \frac{A \cdot \exp \left[- \exp \left(- \frac{E_n - B}{C} \right) \right]}{1 + \exp \left(- \frac{E_n - B_1}{C_1} \right)}. \tag{2.73}$$

Again A, B and C similarly describe the saturation value, the energy at half saturation, and the width of the curve, respectively. The two additional terms B_1 and C_1 increase the flexibility of the function at the cost of adding two additional parameters.

2.4.3   Threshold offset and efficacies

Using the (fitted) state-selective results, it is also possible to obtain both rotational and vibrational efficacies, as discussed in Chapter 6. These efficacies indicate the ability of rotational and vibrational energy of the diatomic molecule to promote reaction with the surface, which is often available from experiments.

To best obtain these values this thesis will make use of the "threshold value" method by Shuai *et al.*[59]. With this method the shift in translational energy $[\Delta S(v, J)]$ of the fitted dissociation curves $[P_{stick}(v, J; E_{kin})]$ with respect to the results of the rovibrational ground state $[P_{stick}(v = 0, J = 0; E_{kin})]$ is calculated by minimising the root-mean-square (RMS) difference between the

curves (or the logarithm of the curves) of the two states

$$RMS[v, J, \Delta S(v, J)] = \Big[\frac{1}{n} \sum_{E_{kin}}^{n} \Big(P_{stick}(v, J; [E_{kin} - \Delta S(v, J)]) $$
$$-P_{stick}(v = 0, J = 0; E_{kin})\Big)^2\Big]^{\frac{1}{2}}. \tag{2.74}$$

This threshold offset ΔS should then allow for an analysis of the results independent of the functional form chosen. The offset can also be fit directly to the sticking probability curves obtained from our dynamics as well as give us another observable that we can compare directly to the experimental value. We make use of the Levenberg-Marquardt routine for fitting, minimising the difference between the sticking curve of the rovibrationally excited state and that of the rovibrational ground state.

With this offset, one can then directly calculate the rotational

$$\mu_{rot}(v, J) = \frac{\Delta S(v, J) - \Delta S(v, 0)}{E_{int}(v, J) - E_{int}(v, 0)} \text{ for } J > 0 \tag{2.75}$$

and vibrational

$$\mu_{vib}(v, J) = \frac{\Delta S(v, 0) - \Delta S(0, 0)}{E_{int}(v, 0) - E_{int}(0, 0)} \text{ for } v > 0 \tag{2.76}$$

efficacies for the (fitted) dissociation curves. The internal energies of the molecule are again obtained from the FGH method as described in 2.2.1.

References

(1) Born, M.; Oppenheimer, R. Zur Quantentheorie Der Molekeln. *Annalen der Physik* **1927**, *389*, 457–484, DOI: `10.1002/andp.19273892002`.

(2) Hohenberg, P.; Kohn, W. Inhomogeneous Electron Gas. *Physical Review* **1964**, *136*, B864–B871, DOI: `10.1103/PhysRev.136.B864`.

(3) Kohn, W.; Sham, L. J. Self-Consistent Equations Including Exchange and Correlation Effects. *Physical Review* **1965**, *140*, A1133–A1138, DOI: `10.1103/PhysRev.140.A1133`.

(4) Perdew, J. P.; Schmidt, K. Jacob's Ladder of Density Functional Approximations for the Exchange-Correlation Energy. *AIP Conference Proceedings* **2001**, *577*, 1–20, DOI: `10.1063/1.1390175`.

(5) Perdew, J. P.; Chevary, J. A.; Vosko, S. H.; Jackson, K. A.; Pederson, M. R.; Singh, D. J.; Fiolhais, C. Atoms, Molecules, Solids, and Surfaces: Applications of the Generalized Gradient Approximation for Exchange and Correlation. *Physical Review B* **1992**, *46*, 6671–6687, DOI: `10.1103/PhysRevB.46.6671`.

(6) Gonzalez-Lafont, A.; Truong, T. N.; Truhlar, D. G. Direct Dynamics Calculations with NDDO (Neglect of Diatomic Differential Overlap) Molecular Orbital Theory with Specific Reaction Parameters. *The Journal of Physical Chemistry* **1991**, *95*, 4618–4627, DOI: `10.1021/j100165a009`.

(7) Chuang, Y.-Y.; Radhakrishnan, M. L.; Fast, P. L.; Cramer, C. J.; Truhlar, D. G. Direct Dynamics for Free Radical Kinetics in Solution: Solvent Effect on the Rate Constant for the Reaction of Methanol with Atomic Hydrogen. *The Journal of Physical Chemistry A* **1999**, *103*, 4893–4909, DOI: `10.1021/jp990969d`.

(8) Díaz, C.; Pijper, E.; Olsen, R. A.; Busnengo, H. F.; Auerbach, D. J.; Kroes, G. J. Chemically accurate simulation of a prototypical surface reaction: H_2 dissociation on Cu(111). *Science (New York, N.Y.)* **2009**, *326*, 832–834, DOI: `10.1126/science.1178722`.

(9) Díaz, C.; Olsen, R. A.; Auerbach, D. J.; Kroes, G. J. Six-dimensional dynamics study of reactive and non reactive scattering of H_2 from Cu(111) using a chemically accurate potential energy surface. *Physical Chemistry Chemical Physics* **2010**, *12*, 6499–6519, DOI: `10.1039/C001956A`.

(10) Nattino, F.; Migliorini, D.; Kroes, G.-J.; Dombrowski, E.; High, E. A.; Killelea, D. R.; Utz, A. L. Chemically Accurate Simulation of a Polyatomic Molecule-Metal Surface Reaction. *The Journal of Physical Chemistry Letters* **2016**, *7*, 2402–2406, DOI: `10.1021/acs.jpclett.6b01022`.

(11) Migliorini, D.; Chadwick, H.; Nattino, F.; Gutiérrez-González, A.; Dombrowski, E.; High, E. A.; Guo, H.; Utz, A. L.; Jackson, B.; Beck, R. D.; Kroes, G.-J. Surface Reaction Barriometry: Methane Dissociation on Flat and Stepped Transition-Metal Surfaces. *The Journal of Physical Chemistry Letters* **2017**, *8*, 4177–4182, DOI: 10.1021/acs.jpclett.7b01905.

(12) Sato, S. Potential Energy Surface of the System of Three Atoms. *The Journal of Chemical Physics* **1955**, *23*, 2465–2466, DOI: 10.1063/1.1741936.

(13) McCreery, J. H.; Wolken, G. A Model Potential for Chemisorption: H_2 +W(001). *The Journal of Chemical Physics* **1975**, *63*, 2340–2349, DOI: 10.1063/1.431663.

(14) Behler, J.; Parrinello, M. Generalized Neural-Network Representation of High-Dimensional Potential-Energy Surfaces. *Physical Review Letters* **2007**, *98*, 146401, DOI: 10.1103/PhysRevLett.98.146401.

(15) Behler, J. First Principles Neural Network Potentials for Reactive Simulations of Large Molecular and Condensed Systems. *Angewandte Chemie International Edition* **2017**, *56*, 12828–12840, DOI: https://doi.org/10.1002/anie.201703114.

(16) Busnengo, H. F.; Salin, A.; Dong, W. Representation of the 6D potential energy surface for a diatomic molecule near a solid surface. *The Journal of Chemical Physics* **2000**, *112*, 7641–7651, DOI: 10.1063/1.481377.

(17) Kosloff, R. Time-Dependent Quantum-Mechanical Methods for Molecular Dynamics. *The Journal of Physical Chemistry* **1988**, *92*, 2087–2100, DOI: 10.1021/j100319a003.

(18) Manzhos, S.; Ihara, M.; Carrington, T. Using Collocation to Solve the Schrödinger Equation. *Journal of Chemical Theory and Computation* **2023**, DOI: 10.1021/acs.jctc.2c01232.

(19) Corey, G. C.; Lemoine, D. Pseudospectral Method for Solving the Time-dependent Schrödinger Equation in Spherical Coordinates. *The Journal of Chemical Physics* **1992**, *97*, 4115–4126, DOI: 10.1063/1.463916.

(20) Lemoine, D. The Finite Basis Representation as the Primary Space in Multidimensional Pseudospectral Schemes. *The Journal of Chemical Physics* **1994**, *101*, 10526–10532, DOI: 10.1063/1.467870.

(21) Light, J. C.; Hamilton, I. P.; Lill, J. V. Generalized Discrete Variable Approximation in Quantum Mechanics. *The Journal of Chemical Physics* **1985**, *82*, 1400–1409, DOI: 10.1063/1.448462.

(22) Cerjan, C., *Numerical Grid Methods and Their Application to Schrödinger's Equation*; Springer Science & Business Media: 1993.

(23) Besprozvannaya, A.; Tannor, D. J. Fast Sine/Cosine Transform for Periodic Functions with Reflection Symmetry. *Computer Physics Communications* **1991**, *63*, 569–577, DOI: 10.1016/0010-4655(91)90276-Q.

(24) Press, W. H.; Teukolsky, S. A.; Vetterling, W. T.; Flannery, B. P., *Numerical Recipes 3rd Edition: The Art of Scientific Computing*; Cambridge University Press: 2007.

(25) Feit, M. D.; Fleck, J. A.; Steiger, A. Solution of the Schrödinger Equation by a Spectral Method. *Journal of Computational Physics* **1982**, *47*, 412–433, DOI: 10.1016/0021-9991(82)90091-2.

(26) Balint-Kurti, G. G.; Dixon, R. N.; Marston, C. C. Time-Dependent Quantum Dynamics of Molecular Photofragmentation Processes. *Journal of the Chemical Society, Faraday Transactions* **1990**, *86*, 1741–1749, DOI: 10.1039/FT9908601741.

(27) Balint-Kurti, G. G.; Dixon, R. N.; Marston, C. C. Grid methods for solving the Schrödinger equation and time dependent quantum dynamics of molecular photofragmentation and reactive scattering processes. *International Reviews in Physical Chemistry* **1992**, *11*, 317–344, DOI: 10.1080/01442359209353274.

(28) Mowrey, R. C.; Kroes, G. J. Application of an Efficient Asymptotic Analysis Method to Molecule–Surface Scattering. *The Journal of Chemical Physics* **1995**, *103*, 1216–1225, DOI: 10.1063/1.469831.

(29) Neuhauser, D.; Baer, M.; Judson, R. S.; Kouri, D. J. The Application of Time-Dependent Wavepacket Methods to Reactive Scattering. *Computer Physics Communications* **1991**, *63*, 460–481, DOI: 10.1016/0010-4655(91)90270-U.

(30) Zhang, D. H.; Zhang, J. Z. H. Full-dimensional Time-dependent Treatment for Diatom–Diatom Reactions: The H_2+OH Reaction. *The Journal of Chemical Physics* **1994**, *101*, 1146–1156, DOI: 10.1063/1.467808.

(31) Olsen, R. A.; Philipsen, P. H. T.; Baerends, E. J.; Kroes, G. J.; Lo/vvik, O. M. Direct Subsurface Absorption of Hydrogen on Pd(111): Quantum Mechanical Calculations on a New Two-Dimensional Potential Energy Surface. *The Journal of Chemical Physics* **1997**, *106*, 9286–9296, DOI: 10.1063/1.474040.

2

2

(32) McCormack, D. A.; Kroes, G.; Olsen, R. A.; Groeneveld, J. A.; van Stralen, J. N. P.; Baerends, E. J.; Mowrey, R. C. Quantum Dynamics of the Dissociation of H_2 on Cu(100): Dependence of the Site-Reactivity on Initial Rovibrational State. *Faraday Discussions* **2000**, *117*, 109–132, DOI: `10.1039/b002507k`.

(33) Marston, C. C.; Balint-Kurti, G. G. The Fourier grid Hamiltonian method for bound state eigenvalues and eigenfunctions. *The Journal of Chemical Physics* **1989**, *91*, 3571–3576, DOI: `10.1063/1.456888`.

(34) Bulirsch, R.; Stoer, J. Numerical treatment of ordinary differential equations by extrapolation methods. *Numerische Mathematik* **1966**, *8*, 1–13, DOI: `10.1007/BF02165234`.

(35) Richardson, L. F.; Gaunt, J. A. VIII. The Deferred Approach to the Limit. *Philosophical Transactions of the Royal Society of London. Series A, Containing Papers of a Mathematical or Physical Character* **1997**, *226*, 299–361, DOI: `10.1098/rsta.1927.0008`.

(36) Verlet, L. Computer "Experiments" on Classical Fluids. I. Thermodynamical Properties of Lennard-Jones Molecules. *Physical Review* **1967**, *159*, 98–103, DOI: `10.1103/PhysRev.159.98`.

(37) Rodríguez-Fernández, A.; Bonnet, L.; Crespos, C.; Larrégaray, P.; Díez Muiño, R. When Classical Trajectories Get to Quantum Accuracy: The Scattering of H_2 on Pd(111). *The Journal of Physical Chemistry Letters* **2019**, *10*, 7629–7635, DOI: `10.1021/acs.jpclett.9b02742`.

(38) Wijzenbroek, M.; Somers, M. F. Static surface temperature effects on the dissociation of H_2 and D_2 on Cu(111). *The Journal of Chemical Physics* **2012**, *137*, 054703, DOI: `10.1063/1.4738956`.

(39) Spiering, P.; Wijzenbroek, M.; Somers, M. F. An improved static corrugation model. *The Journal of Chemical Physics* **2018**, *149*, 234702, DOI: `10.1063/1.5058271`.

(40) Sears, V. F.; Shelley, S. A. Debye–Waller factor for elemental crystals. *Acta Crystallographica Section A Foundations of Crystallography* **1991**, *47*, 441–446, DOI: `10.1107/S0108767391002970`.

(41) Kroeger, F. R.; Swenson, C. A. Absolute linear thermal-expansion measurements on copper and aluminum from 5 to 320 K. *Journal of Applied Physics* **1977**, *48*, 853–864, DOI: `10.1063/1.323746`.

(42) Chae, K. H.; Lu, H. C.; Gustafsson, T. Medium-energy ion-scattering study of the temperature dependence of the structure of Cu(111). *Physical Review B* **1996**, *54*, 14082–14086, DOI: `10.1103/PhysRevB.54.14082`.

(43) Daw, M. S.; Baskes, M. I. Semiempirical, Quantum Mechanical Calculation of Hydrogen Embrittlement in Metals. *Physical Review Letters* **1983**, *50*, Publisher: American Physical Society, 1285–1288, DOI: 10.1103/PhysRevLett.50.1285.

(44) Stott, M. J.; Zaremba, E. Quasiatoms: An approach to atoms in nonuniform electronic systems. *Physical Review B* **1980**, *22*, 1564–1583, DOI: 10.1103/PhysRevB.22.1564.

(45) Nørskov, J. K. Covalent effects in the effective-medium theory of chemical binding: Hydrogen heats of solution in the 3D metals. *Physical Review B* **1982**, *26*, Publisher: American Physical Society, 2875–2885, DOI: 10.1103/PhysRevB.26.2875.

(46) Daw, M. S.; Baskes, M. I. Embedded-atom method: Derivation and application to impurities, surfaces, and other defects in metals. *Physical Review B* **1984**, *29*, 6443–6453, DOI: 10.1103/PhysRevB.29.6443.

(47) Nattino, F.; Díaz, C.; Jackson, B.; Kroes, G.-J. Effect of Surface Motion on the Rotational Quadrupole Alignment Parameter of D_2 Reacting on Cu(111). *Physical Review Letters* **2012**, *108*, 236104, DOI: 10.1103/PhysRevLett.108.236104.

(48) Mondal, A.; Wijzenbroek, M.; Bonfanti, M.; Díaz, C.; Kroes, G.-J. Thermal Lattice Expansion Effect on Reactive Scattering of H_2 from Cu(111) at $T_s = 925$ K. *The Journal of Physical Chemistry A* **2013**, *117*, 8770–8781, DOI: 10.1021/jp4042183.

(49) Sheng, H. W.; Kramer, M. J.; Cadien, A.; Fujita, T.; Chen, M. W. Highly optimized embedded-atom-method potentials for fourteen fcc metals. *Physical Review B* **2011**, *83*, 134118, DOI: 10.1103/PhysRevB.83.134118.

(50) Gulding, S. J.; Wodtke, A. M.; Hou, H.; Rettner, C. T.; Michelsen, H. A.; Auerbach, D. J. Alignment of $D_2(v, J)$ Desorbed from Cu(111): Low Sensitivity of Activated Dissociative Chemisorption to Approach Geometry. *The Journal of Chemical Physics* **1996**, *105*, 9702–9705, DOI: 10.1063/1.472979.

(51) Wetzig, D.; Rutkowski, M.; David, R.; Zacharias, H. Rotational Corrugation in Associative Desorption of D_2 from Cu(111). *Europhysics Letters* **1996**, *36*, 31, DOI: 10.1209/epl/i1996-00183-2.

(52) Hou, H.; Gulding, S. J.; Rettner, C. T.; Wodtke, A. M.; Auerbach, D. J. The Stereodynamics of a Gas-Surface Reaction. *Science* **1997**, *277*, 80–82, DOI: 10.1126/science.277.5322.80.

2

(53)   Michelsen, H. A.; Rettner, C. T.; Auerbach, D. J.; Zare, R. N. Effect of rotation on the translational and vibrational energy dependence of the dissociative adsorption of D_2 on Cu(111). *The Journal of Chemical Physics* **1993**, *98*, 8294–8307, DOI: 10.1063/1.464535.

(54)   Kaufmann, S.; Shuai, Q.; Auerbach, D. J.; Schwarzer, D.; Wodtke, A. M. Associative desorption of hydrogen isotopologues from copper surfaces: Characterization of two reaction mechanisms. *The Journal of Chemical Physics* **2018**, *148*, 194703, DOI: 10.1063/1.5025666.

(55)   Nattino, F.; Genova, A.; Guijt, M.; Muzas, A. S.; Díaz, C.; Auerbach, D. J.; Kroes, G.-J. Dissociation and recombination of D_2 on Cu(111): ab initio molecular dynamics calculations and improved analysis of desorption experiments. *The Journal of Chemical Physics* **2014**, *141*, 124705, DOI: 10.1063/1.4896058.

(56)   Levenberg, K. A Method for the Solution of Certain Non-Linear Problems in Least Squares. *Quarterly of Applied Mathematics* **1944**, *2*, 164–168, DOI: 10.1090/qam/10666.

(57)   Marquardt, D. W. An Algorithm for Least-Squares Estimation of Non-linear Parameters. *Journal of the Society for Industrial and Applied Mathematics* **1963**, *11*, 431–441.

(58)   Newville, M. et al. Lmfit/Lmfit-Py 1.0.0, Zenodo, 2019, DOI: 10.5281/zenodo.3588521.

(59)   Shuai, Q.; Kaufmann, S.; Auerbach, D. J.; Schwarzer, D.; Wodtke, A. M. Evidence for Electron–Hole Pair Excitation in the Associative Desorption of H_2 and D_2 from Au(111). *The Journal of Physical Chemistry Letters* **2017**, *8*, 1657–1663, DOI: 10.1021/acs.jpclett.7b00265.

Beyond the static corrugation model

Abstract

The D_2 on Cu(111) system has for many years been one of the major benchmark systems for surface scientists. Generating surface configurations using the embedded atom method (EAM), we investigate the quality of the chemically accurate static corrugation model (SCM) for including surface temperature effects, with a focus on the random displacement approach to its distorted surface generation. With this EAM potential, we also treat the Cu(111) surface of our system fully dynamically and shed a further light on not only the quality of the SCM sudden approach, but also the limited effect of energy exchange with the surface. Reaction and (in)elastic scattering probability curves, as well as simulated time-of-flight spectra, show good agreement with both earlier works and experimental results, with surface reactions showing a preference for surface atoms displaced away from the incoming molecule. The good agreement with the non-static surface model also further establishes the limited effect of energy exchange on not only the reaction, but also on the elastic and inelastic scattering probabilities, even though some molecular translational energy is deposited into the surface.

3.1   Introduction

For many years, theoreticians and experimentalists have been working on describing gas-solid surface reactions[1–3]. These are especially of interest due to their importance in many (industrial) processes, such as the Haber-Bosch process[4] or H_2 dissociation for hydrogen engines[5]. To best describe these processes the reaction mechanisms are broken up into simple elementary reaction steps. Studying of individual steps would then allow for a very accurate description of the full catalytic process.

Our system of choice for this chapter is the D_2 dissociation on a Cu(111) surface. This system is one of the model systems for surface scientists, with a lot of available experimental[6–13] and theoretical[2, 14–19] data. In the past, theoretical work was often performed using the Born-Oppenheimer and the static surface (BOSS) approach, where surface atoms are assumed to be fully static, and the electron and nucleus dynamics are assumed to be separated. Here the *ab initio* density functional theory (DFT) results are often fit to a 6D potential energy surface (PES), using an approach such as the corrugation reducing procedure (CRP)[20].

Making use of this method, Díaz *et al.*[14] developed the specific reaction parameter (SRP) approach. By linearly combining two different DFT functionals, one overestimating and one underestimating the dissociation barrier, this work was able to reproduce experimental molecular beam experiments of H_2 of Cu(111) with an error of less than 1.0 kcal/mol[21].

Although good results were obtained using these methods, the surface slab was kept at its ideal, "0 K" configuration, whereas experiments are often performed at higher temperatures[22]. To allow for the PES to take into account surface temperature effects, Wijzenbroek and Somers coined the static corrugation model (SCM)[23]. In this model, surface slab atoms are displaced from the ideal lattice, but kept static. It was theorised such an approach would work well for a H_2 or D_2 on copper system, which is expected to have only limited energy transfer, both due to the mass mismatch between hydrogen and copper atoms as well as the relatively slow speed of the thermally equilibrated copper surface atoms. A two body (H-Cu) coupling potential (V_{coup}) was introduced to describe the changes in the PES due to these displacements. This coupling potential was fitted to a data set of surface configurations obtained using DFT calculations with the SRP48 exchange-corellation functional[17]. This initial approach to the SCM showed great agreement with *ab initio* molecular dynamics (AIMD) calculations using the same DFT functional[17]. Furthermore, it resulted in better agreement with experiment than originally achieved with the SRP-BOSS approach, although the limited size of the data

set also showed a sizeable error in the H-Cu coupling potential. To improve upon the SCM, Spiering *et al.*[24] expanded the SCM to an effective three-body potential, by including the H-H distance into the coupling potential. Furthermore, the data set for fitting was greatly expanded, which reduced the RMSE of the fitted three-body coupling potential to 29.4 meV, compared to 66.6 meV for the two-body potential of the initial study. To generate these statically distorted surface slabs for the SCM, each surface atom is displaced using a normal distribution based on experimentally determined Debye-Waller factor for a specific modelled temperature. The interlayer distances are instead taken directly from experiment.

It is, however, still unclear if such a random displacement generates physically relevant surface slabs. Therefore, we elected to expand upon the SCM approach by generating surface slabs using a highly accurate embedded atom method (EAM) potential as described by Sheng *et al.*[25]. This potential has been shown to accurately describe not only lattice constants and phonon dispersion curves but also thermal expansion of the bulk metal and the FCC copper surface slabs[25]. These surface slabs can then be used in combination with the SCM coupling potential to generate dissociation curves and simulated time-of-flight spectra. A comparison of these curves between these randomly displaced surfaces and EAM generated surfaces should allow us to validate the quality of this earlier work.

To further expand our model, we can even use the EAM potential to dynamically describe our copper surface during dissociation simulations. Here, the SCM coupling potential does not only describe the effect of the surface on the D_2, but also describes the effect of the D_2 on the surface, effectively allowing for energy exchange to be introduced in our system. Energy exchange has long be theorised to not be very relevant for dissociation probabilities in the H_2 on Cu(111) system, due to the large mass mismatch. In this work, however, we will be able to investigate its effect directly, by comparing results from both a static and dynamic surface using exactly the same potentials.

With the SCM approach, switching to another surface facet of the D_2/Cu system would only require a new CRP BOSS PES. This contrasts other approaches, like high dimensional neural network potentials (HD-NNPs), which would need a new extended training set to be fit to. The SCM coupling potential is also generic in that respect, as it has been shown that the underlying DFT functional of V_{coup} is transferable between the H_2 on Cu(111) and H_2 Cu(100) systems[26]. Moreover, recently a H_2 on Cu(211) stepped CRP BOSS PES has been constructed also with the SRP48 DFT functional[27, 28].

The transferability of the SCM approach to surface slabs of a different transition metal, such as Pt or Ag, will still require additional work. Although

this can be greatly reduced by using one of the many (CRP) PESs[3] and EAM potentials[25] available in literature, reducing it to merely fitting a new SCM coupling potential. Of special interest would be those systems with an early barrier, as they exhibit a relatively small amount of corrugation, and a large mass mismatch between the D_2 and the metal. For those systems where no well performing GGA-level DFT functionals are available, like Pd[29], another first principles approach would be required to obtain a data set to fit the SCM coupling potential. Similarly, a new data set would be required to fit an HD-NNP for such a new system, which can generally also require extensive DFT data sets[30].

In this chapter, however, we aim to investigate two assumptions made in previous studies. Primarily, we will validate the physical relevance of the SCM random displacement approach to surface slab generation, by comparing the results of D_2 dissociation on such a surface slab to a physically accurate surface slab generated with an EAM potential. Furthermore, we also go beyond the SCM by dynamically treating the metal atoms of the surface slab with this EAM potential. This will allows us to both further investigate the quality of the sudden approximation that lies at the base of the SCM, as well as investigate the importance of energy exchange with the Cu surface for chemisorption and rovibrationally (in)elastic scattering probabilities.

3.2   Method

All calculations for this chapter are performed using the quasi-classical dynamics (QCD) approach as described in section 2.2.1, for a variety of initial rovibrational states. The final states of the scattered trajectories are binned using the standard binning method. The time-of-flight spectra presented in 3.3.3 were simulated using fits to the obtained dissociation curves using the LGS functional form, with the required experimental parameters and angular averaging as published in [16].

Results of both the random displacement (RD-SCM) and the MD based EAM-SCM results are included, as well as the moving surface EAM-DCM results. For the EAM-SCM and EAM-DCM results, a database of thermally distorted surface slabs was created using molecular dynamics, and the highly accurate EAM potential for copper as described by Sheng *et al.*[25]. This same database of surface slabs is also used in Chapters 4, 5, and 6 of this thesis.

To be able to perform molecular dynamics, the EAM potential is described using 1001 equidistant data points for the pair, density and embedding functions, which are fitted using cubic splines. A cutoff is used at 0 Å and 6.5 Å for the pair and density functions, and at 0.0 and 1.0 density for the embedding

function. Outside these final spline knots, both the value of the function and its derivative yield 0.

NVT dynamics were run using a Velocity-Verlet algorithm[31] and the Berendsen thermostat[32], while NVE propagation was performed using the Bulirsch-Stoer predictor-corrector algorithm[33].

Step-wise volume scaling was performed to equilibrate the pressure and Cu lattice constant, by running 1 ps of NVT dynamics and storing the virial pressure each step, calculated using[34]

$$P_{vir} = Nk_bT + \frac{1}{2} \cdot \frac{1}{3} \sum_{i \neq j} r_{ij} \cdot F_{ij} \tag{3.1}$$

Here N is the number of (mobile) surface atoms, k_b is the Boltzmann constant, T is the instantaneous surface temperature, and r_{ij} and F_{ij} are, respectively, the distance and force between surface atom i and j. Due to double counting this dot product in halved. The total average pressure is then divided by a scaling factor of 2500 GPa and used to scale the simulation box volume. This scaling factor was chosen arbitrarily, to ensure the surface is not scaled too fast or too slow.

To ensure this yields satisfactory results, we also determine the pressure from the diagonal components of the virial stress tensor. Both these methods are grounded in theory and should yield in the same values under equilibrated conditions[34].

3.2.1 Bulk lattice constant determination

To determine the relaxed bulk lattice constant, a cell of $7 \times 7 \times 7$ Cu atoms was placed in the optimal FCC lattice structure. Some initial momentum was also included, using a normal distribution based on the modelled surface temperature, to avoid any rapid changes during the initial surface relaxation steps. The minimum image convention is applied in the x, y and z Cartesian directions, Next this slab was propagated in the canonical ensemble (NVT) for 40000 steps with a step size of .005 ps, for a total propagation of 200 ps. Volume rescaling was performed between 40 and 160 ps of this run, scaling every ps to ensure the thermodynamically favoured box volume is attained. To evaluate the quality of this run, the average atom-atom distance, temperature, and the kinetic and potential energy of the bulk copper are calculated each step and stored for evaluation. Next this NVT relaxed bulk is propagated for 250 steps (∼6 ps) in the micro-canonical ensemble (NVE), where total propagation time varies due to the use of the Bulrisch-Stoer predictor-corrector

algorithm. Here we again evaluate the stability of our copper based on the temperature, average atom-atom distance, kinetic and potential energies, and the virial pressure and diagonal components of the virial stress tensor. The relaxed bulk lattice constant is finally obtained from the final volume of our box. This is repeated 200 times, each with a unique seed used to generate the initial conditions, to obtain the average bulk lattice constant of this potential for our chosen temperature.

3.2.2   Surface slab generation

To generate surface slabs, we take the calculated bulk lattice constant to generate the initial $7 \times 7 \times 7$ FCC copper lattice, and again apply some initial momentum from a normal distribution based on the modelled surface temperature. We further repeat all steps for our bulk lattice, as described above, but without applying any volume rescaling.

Then three consecutive layers of our surface slab with the lowest value of z, for a total of 147 atoms, are set locked to their current positions. The minimum image convention is only applied in the x- and y-directions, parallel to the static layers. This new surface slab is then propagated in the canonical ensemble for a total of 250 ps and a step size of 0.0005 ps (50000 steps). It is important to note we do not apply any volume rescaling during these steps, to ensure our static layers properly model the bulk. This does also mean our top layers will exhibit some stress, due to the change in pressure when moving from the bulk to a surface configuration. A short NVE run of 1000 steps ($\sim$40 ps) is again used to determine stability of our surface slab.

To ensure the surface slab atoms are always located approximately at the same position, we next attempt to re-center our slab. We perform an NVE dynamics run of 25000 steps ($\sim$1100 ps), logging the average position of each atom in the top layer of our surface slab. After this run, we shift our entire slab, including the static bulk-like layers, so that the average position of the entire top layer is found at (x, y, z)=(0, 0, 0). With this process completed, we start our final dynamics run to obtain traces of our surface slab positions and momenta. During an NVE dynamics run of 1250 steps, we take a snapshot every 50 steps ($\sim$2 ps) of both the surface slab positions and momenta for a total of 25 snapshots each. To obtain a suitable and diverse amount of traces, we repeat this entire surface slab generation scheme 1000 times, for a total of 25000 surface slab positions with matching momenta. These can then be loaded into our SCM dynamics as an alternative to the random displacement approach of the earlier works.
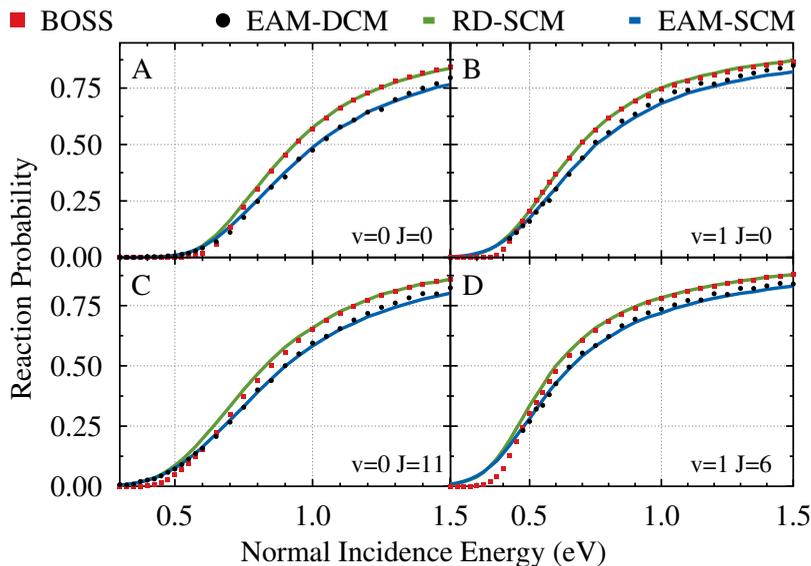
FIGURE 3.1: State-specific reaction probabilities for the D_2 on Cu(111) system and for four different approaches: BOSS (red squares), RD-SCM (green curve), EAM-SCM (blue curve) and EAM-DCM (black circles). For the CM approaches, a modelled surface temperature of 925K was used. Shown are the initial rovibrational states (a) v = 0, J = 0; (b) v = 1, J = 0; (c) v = 0, J = 11; (d) v = 1, J = 6.

3.3 Results and discussion

3.3.1 Reaction probability curves

To validate the quality and physical relevance of the random displacement approach to generating SCM surface slabs (RD-SCM), we will compare the dissociative chemisorption reaction probabilities obtained with this approach to those obtained using surface slabs generated with an EAM potential (EAM-SCM). Also included are dissociation curves for the same dynamics on a moving surface, using the EAM potential to also describe the interactions between the copper atoms. This method we will refer to as the dynamic corrugation model (DCM), using an EAM potential (EAM-DCM). Comparisons between these different methods will give us insight not only in the quality of the RD-SCM generated surface slabs, but also on the effect of energy exchange with our moving surface and the validity of the sudden approach as we use it in the SCM. Finally, we include results of an ideal, "0 K" static surface, which we obtain using the often used BOSS approach. This allows us to investigate the general effect the different models for including surface temperature effects have on the

dissociation curves.

In Figure 3.1, we show the reaction probability curves for several different rovibrational states. As expected, the general trend for all the different approaches are relatively similar. At low incidence energy, the D_2 molecule does not have enough energy to pass over the minimum energy barrier for dissociation, and reaction probability will be minimal. As the normal incidence energy increases so does dissociation probability, until it reaches a maximum, or saturation, value.

The first point of note in this figure is the difference in saturation values between the different approaches. Both the RD-SCM and BOSS methods show a similar saturation at around 0.9, while the EAM-SCM and EAM-DCM approaches both have a lower value at around 0.85, with the EAM-DCM approach always being slightly higher. This could indicate the surface slabs generated with the EAM potential contain somewhat higher maximum barriers compared to those generated through the RD-SCM. These values are, however, very difficult to obtain experimentally and thus is of much less importance for the quality of our model when comparing to experiment[16].

All three CM approaches (RD-SCM, EAM-SCM and EAM-DCM) predict a higher reaction probability than that shown by the BOSS model, yet their curves do not increases as steeply. This broadening of the dissociation curve is generally attributed to surface temperature effects, and has been extensively discussed in earlier work[23, 24, 35]. Both the EAM-SCM and EAM-DCM show a bit more broadening than the RD-SCM approach, although it is harder to quantize due to the lower saturation value. This is especially of note as previous work has shown some indication the width and the saturation value of the dissociation curves are not completely independent[23].

The availability of energy exchange appears to only very limitedly affect our system, as we find great agreement between the static surface approach of the EAM-SCM and the dynamic surface approach of the EAM-DCM. Although earlier studies have shown similar results for H_2[17, 36–38], this is one of the first examples of a direct and extensive comparison between almost identical methods, one with a dynamic surface and one without.

3.3.2   (In-)elastic scattering probabilities

To further analyse our dissociation simulations, we can also look at the rovibrational elastic and inelastic scattering probabilities. In Figure 3.2, we again compare the BOSS (red squares), RD-SCM (green curves), EAM-SCM (blue curves) and EAM-DCM (black circles) methods, now for the elastic [(b), (d), (f),
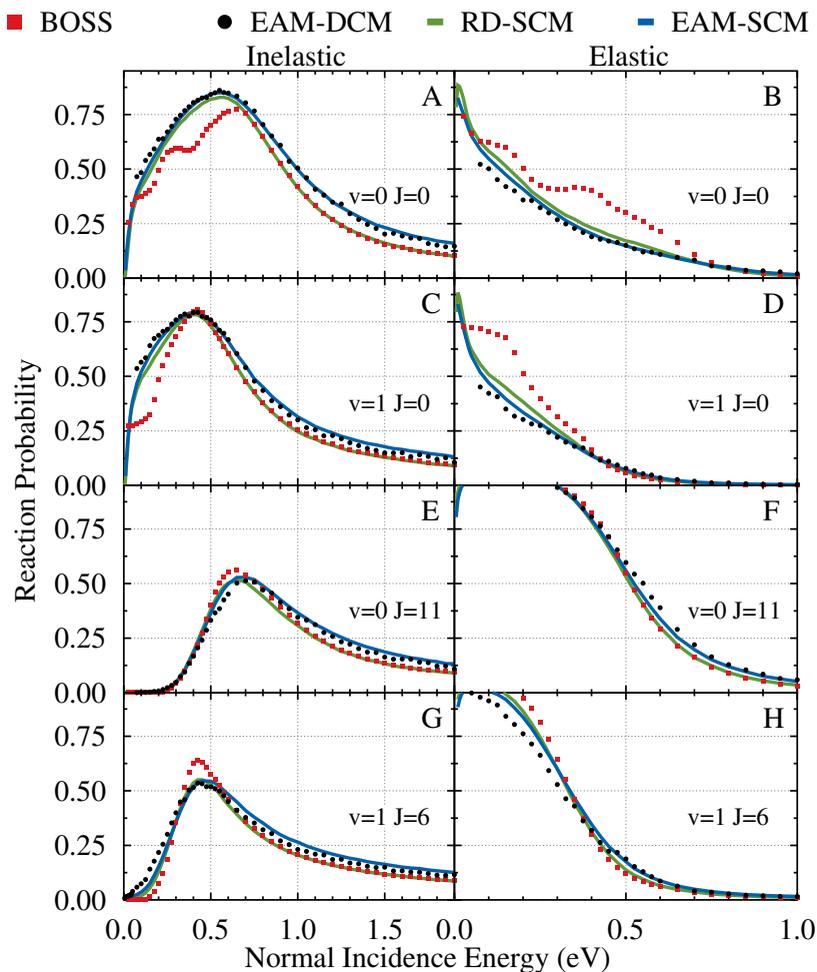
FIGURE 3.2: State-specific, elastic [(b), (d), (f), and (h)] and inelastic [(a), (c), (e), and (g)] scattering probabilities for the D_2 on Cu(111) system and for four different approaches: BOSS (red squares), RD-SCM (green curves), EAM-SCM (blue curves) and EAM-DCM (black circles). For the CM approaches, a modelled surface temperature of 925K was used. Shown are the initial rovibrational states: (a) and (b) v = 0, J = 0; (c) and (d) v = 1, J = 0; (e) and (f) v = 0 J = 11; (g) and (h) v = 1, J = 6.

and (h)] and in-elastic [(a), (c), (e), and (f)] rovibrational scattering probabilities for the same four initial rovibrational states as discussed before.

In general, we find a preference for elastic scattering at lower incidence energies, where there is not enough energy available within the molecule to reach other rovibrational states. As the kinetic energy of the molecule increases, more and more rovibrational states become available and we find higher and higher probability for inelastic scattering. At very high incidence energies, chemisorption dominates and only limited scattering is observed.

For the rovibrational ground state [(a) and (b)], as well as the vibrationally excited states [(c), (d), (g), and (h)], the BOSS model predicts much higher elastic scattering for the lower incidence energies. Moving to higher energies, we again see almost perfect agreement with the RD-SCM curves and qualitative agreement with the EAM-SCM and EAM-DCM approaches. Surprisingly, this effect is absent for the $v = 0$, $J = 11$ state, where the BOSS model shows good agreement with all CM results for all incidence energies.

Agreement between the EAM-SCM and EAM-DCM approaches is again very good, with only minor differences we can partially attribute to the relatively low amount of trajectories ran for the EAM-DCM approach. This further validates the quality of the SCM sudden approach. As the main difference between these two approaches is the possibility of energy exchange between the copper surface and the D_2 molecule, this agreement further enforces our observation of the limited effect of energy exchange on not only the final dissociation results, but also on these rovibrational (in)elastic scattering results. The latter are expected to be more sensitive to details of the PES and to the exchange of energy between D_2 and the surface.

Interestingly, an analysis of the energy exchange in our DCM trajectories does show a small transfer of energy between the copper surface and D_2 molecule. At very low incidence energies (< 150 meV), we find a flow of energy into the D_2 ($< 10\%$), while at higher incidence energies we primarily find a drain of energy into the surface ($\sim 15\%$). This drain of energy was found to be predominantly flowing from the translational energy of the D_2 molecule. Consequently, little difference was found in the rovibrational energy of scattered molecules when comparing the EAM-DCM and EAM-SCM approaches. Furthermore, the average turning point of the scattered molecules was found to be similar between these two methods. This, combined with the minimal differences in (in)elastic rovibrational scattering probabilities, leads us to believe this energy exchange as a result of a mostly mechanical coupling primarily occurs after the scattering event as the D_2 moves away from the surface. We are not aware of any previous works discussing this phenomenon without there being additional particles already on the surface[39], and as such would consider it of great

interest for future work.

The energy exchange at very low incidence energies does appear to affect the final rovibrational state of the scattered molecules. Primarily, it appears to be directly related to the z-coordinate, as molecules that get closer to the surface obtain a larger amount of energy. It remains, however, a question on how accurate the QCT method is for these very low incidence energies and to what extent quantum dynamical effects like zero point energy conservation, of the molecule and of the surface atoms, play a role[2].

3.3.3   Simulated time-of-flight spectra

To better compare our theoretical results to experiment, our reaction probability curves were used to simulate time-of-flight (ToF) spectra. We followed the procedure as outlined in 2.4.2, but also in more detail by Nattino *et al.*[16]. The cut-off function was of the tanh form, with t_c and t_w equal to 19.5 μs and 6.6 μs, respectively. As experimental results are often obtained in the form ToF spectra, and are generally most sensitive for the curve onset of the initial state specific reaction probability curve, we believe ToF spectra are one of the better ways of comparing theoretical results to experimental data, especially when correct and accurate experimental ToF parameters are known and have been published. Thus this work is of great interest, as it both simulated ToF spectra, and fit experimental results using the same expression.

Simulated spectra of a selection of four different rovibrational states for the four theoretical approaches discussed in this work are shown in Figure 3.3. The rovibrational states shown were chosen such that they cover a variety of different excited states, as well as the rovibrational ground state. Furthermore, we also included experimental results from Auerbach *et al.*[8] refit in earlier work, as well as AIMD results, both obtained from the work by Nattino *et al.*[16]. These experimental results were obtained from recombinative desorption experiments of D_2 permeating through the bulk metal to a $Cu(111)$ surface, at a surface temperature of 925 K. As such rely on the applicability of detailed balance[8]. Surface motion effects, for a modelled surface temperature of 925 K, were also included in these AIMD results.

Figures 3.3(a), 3.3(e), and 3.3(i) show our simulated results for the rovibrational ground state. Good agreement is found between the different CM approaches, as was the case for the chemical desorption curves. A slight difference between peak width is observable, with the EAM-SCM approach showing the highest width. The peak location, however, appears to be the same for all three methods. The BOSS model, on the other hand, shows a much more narrow peak with a peak location at a shorter time of flight. The AIMD peak
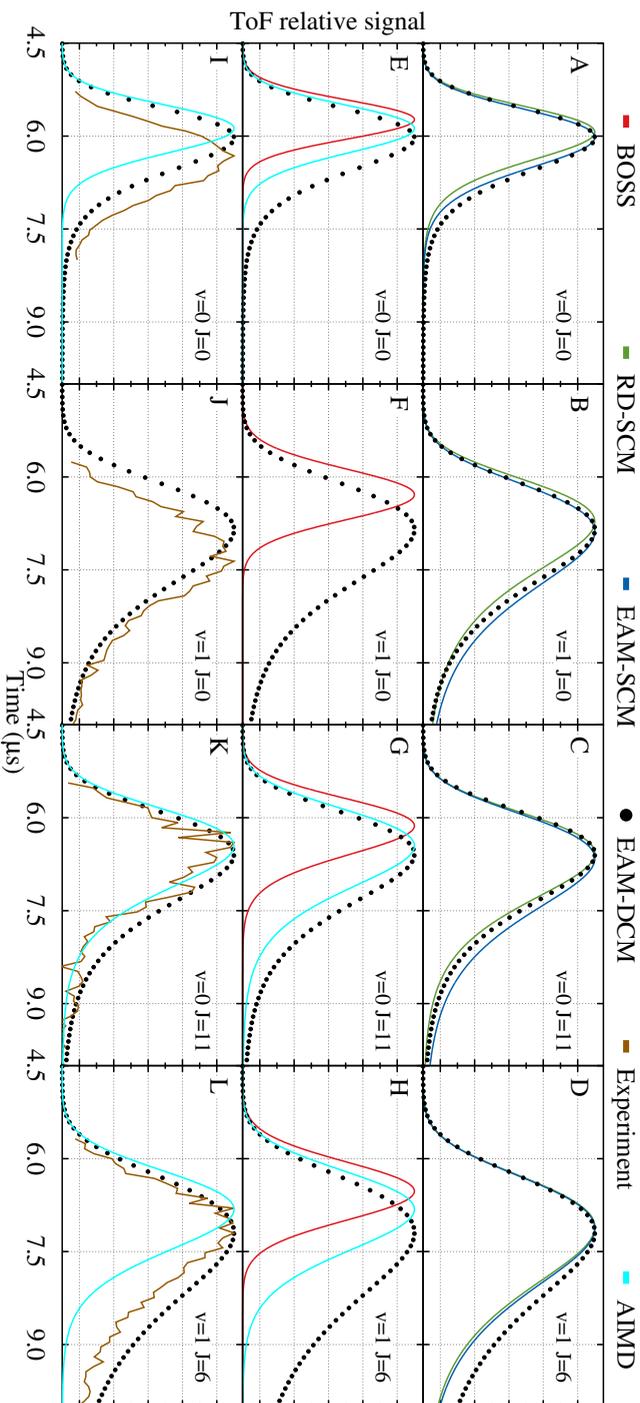
FIGURE 3.3:   Simulated time-of-flight spectra for the D_2 on Cu(111) system. For four different rovibrational states, RD-SCM (green curves), EAM-SCM (blue curves) and EAM-DCM (black circles) are compared to each other [(a)–(d)], as well as to the BOSS approach (red curves)[(e)–(h)], and refitted experimental results (orange curves)[(i)–(l)] and AIMD results (cyan curves)[(e)–(l)] from Nattino *et al.*[16]. For the CM approaches and the AIMD results, a modelled surface temperature of 925K was used, which matches the conditions of the experiment. Shown are the initial rovibrational states: (a), (e), and (i) $v = 0$, $J = 0$; (b), (f), and (h) $v = 1$, $J = 0$; [(c), (g), and (k)]: $v = 0$ $J = 11$; [(d), (h), and (l)]: $v = 1$, $J = 6$.

can be found at approximately the same value as the CM peaks, yet its width is significantly lower. In contrast, looking at the experimental curve, we observe a width similar to that of the CM approaches. The curve is, however, shifted compared to the CM curves, showing a peak location at a higher time of flight.

A similar thing can be observed in Figs. 3.3(b), 3.3(f), and 3.3(j) for the vibrationally excited v = 1, J = 0 state. Unfortunately, however, no AIMD data was available for this state. The width for the three CM approaches is once again similar and close to that of the experimental results. Peak location also shows similar results, with the CM approaches underestimating that of the experiment. The BOSS model shows the worst agreement, with a much narrower peak and a peak height about twice as far from experiment.

Moving to the rotationally excited states in Figure 3.3(e)-(h), we again see that the BOSS model yields both the narrowest peak, as well as the lower time-of-flight for the peak. The different CM approaches show peaks at the highest time of flight, each with approximately the same value. The experimental results are found somewhere between these peaks, with a width closer to that of the CM results. AIMD results for these curves are a bit mixed, as the agreement for the v = 0, J = 11 state appears to be almost perfect, while agreement with the v = 1, J = 6 experimental data is much worse.

Overall, we see improved agreement with experiment when including the SCM and DCM approaches, regardless of which variation. RD-SCM, EAM-SCM, EAM-DCM all show very similar results, with RD-SCM always showing the narrowest peak of the three. Due to the nature of simulating the time-of-flight spectra, however, small variations are expected. The results when using the BOSS model showed the narrowest peaks as well as the shortest time-of-flight for each rovibrational state we investigated, often well below the value found in experiment. This matches findings from earlier work[16].

3.3.4   Effect of RD-SCM on atom displacement

In an attempt to directly compare the randomly generated and EAM generated surface slabs, we investigated the displacements of each individual surface slab atom for every Cartesian coordinate. Only those atoms within the SCM cutoff distance of 16 bohrs (~ 8.47 Å) were included in these results. As discussed in section 2.3.1 of Chapter 2, the RD-SCM approach makes use of the Debye-Waller factor to calculate the standard deviation for the Gaussian displacement of each surface atom. The EAM-SCM approach instead uses surface slabs simulated through another potential, in our case the EAM. Assuming the simulation attains a proper thermodynamic equilibrium, this approach should also result in a Gaussian distribution for our displacements.

3
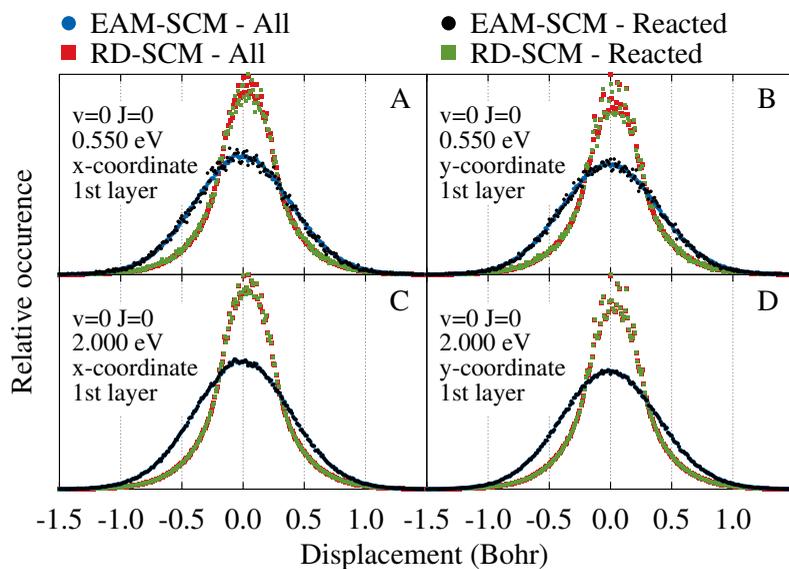
FIGURE 3.4: Surface slab atom displacement at a modelled surface temperature of 925 K relative to the ideal, 0 K lattice. Only those atoms in the first surface layer are included for those trajectories ran on the rovibrational ground state. Included are the displacements both for those trajectories that reacted, and for all trajectories ran for RD-SCM, green and red squares respectively, and EAM-SCM, black and blue circles respectively. Displacements are shown for D_2 normal incidence energies of 0.550 eV [(a) and (b)] or 2.000 eV [(c) and (d)], separating the x-coordinate [(a) and (c)] and y-coordinate [(b) and (d)].

3
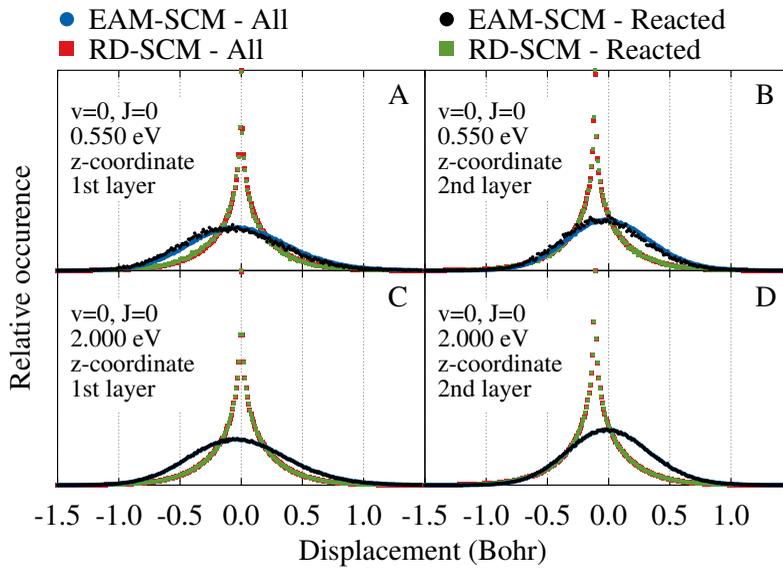
FIGURE 3.5: Surface slab atom displacement at a modelled surface temperature of 925 K relative to the ideal, 0 K lattice. Only those trajectories ran on the rovibrational ground state are shown. Included are the displacements both for those trajectories that reacted, and for all trajectories ran for RD-SCM, green and red squares respectively, and EAM-SCM, black and blue circles respectively. Displacements are shown for D_2 normal incidence energies of 0.550 eV [(a) and (b)] or 2.000 eV [(c) and (d)], separating the x-coordinate [(a) and (c)] and y-coordinate [(b) and (d)].

In Figure 3.4, we outlined the displacements in the x- [(a) and (c)] and y-direction [(b) and (d)] both at the onset of the reaction probability curve [(a) and (b)] as well as at the saturation value [(c) and (d)]. Only those surface slab atoms at the top layer were included in these results. Separate curves were also included for only those trajectories where the D_2 dissociated.

Comparing the RD-SCM displacements for all trajectories (red) to only those that reacted (green), we see very similar curves, both for the x- and y-coordinates. Due to the low reaction probability at curve onset, the data set for the reacted trajectories show a decent amount of noise. This is significantly decreased when looking at the displacement distribution of the reacted slabs near saturation value, although there is still a variation in the results for very low displacements. There also appears to be a slight preference towards a positive displacement even at these higher incidence energies. It is unclear yet why this occurs, although it could be related to the method of generating displacements.

Similar noise is found with the EAM-SCM results for the reacted trajectories at low incidence energy. This, however, disappears when moving towards high energy, or when also including the trajectories that did not react. Furthermore, no clear preference can be found towards a positive or negative displacement, as would be expected for in-plane displacements.

Comparing the two methods to each other, we do see a very clear difference. While both approaches appear to result in a normal distribution of displacements, they have a very different width. The EAM-SCM displacements, obtained from EAM surface slab simulations, showing much broader peaks.

Next, we discuss the most interesting of the three Cartesian directions, the z-coordinate. Displacements towards (+z), or away from (-z), the incoming reactant molecules have in previous works been shown to affect dissociation probabilities[40–43]. For example, Bonfanti *et al.*[40] used a simple 7D model to quantum dynamically show increased reaction probabilities when surface layer atoms are moved away from the incoming H_2 molecule.

In Figures 3.5(a) and 3.5(b), we compare the EAM-SCM and RD-SCM results at reaction probability curve onset for the first and second surface layer atoms. Again only those trajectories that reacted were included separately. For EAM-SCM, reacted trajectories appear to show a clear preference towards a negative displacement in z, away from the D_2 molecule, as the peak of the atom displacement distribution is slightly shifted towards negative z. This phenomena can be observed both for the first layer (a) as well as the second layer (b) and matches results found with the simple 7D model[40]. Interestingly, the opposite effect is found for the CH_4 on Pt(111), Ir(111) and Ni(111) systems, where surface atom displacement away from the reactant increased the barrier

height[41–43]. Furthermore, limited dynamic puckering of the surface atoms is expected away from the bulk when treating this system dynamically, as systems with a large mass mismatch have been shown to be primarily dominated by the the recoil effect[42, 43].

A similar effect can not be seen with the results for the RD-SCM approach, as both the reacted and total surface atom displacements distributions show a similar width and peak location. This distribution also does not appear to be that of a Gaussian. We attribute this to the way the displacements are generated, as it is only ensured the total displacements in the direction of the displacement, and not for the x-, y- or z-axes individually, follows a Gaussian distribution with the standard deviation calculated with the Debye-Waller factor. Similar distributions to that in the z-direction are thus found when looking along the u- and v-axes for the (111) surface slab. Furthermore, the second layer shows a static shift of negative z. This is also attributed to the RD surface slab generation, as experimental interlayer distances are applied when generating the surface, instead of the bulk lattice constant, as is used for the x- and y-directions.

At much higher incidence energies [(c) and (d)], we no longer see the EAM-SCM preference towards a negative z-displacement. At such a high energy, almost all trajectories will react, making the lowest barrier path much less visible. For the RD-SCM results, we again see this second layer shift due to the experimental interlayer distance.

3.4 Conclusion

Using the dissociation of D_2 on Cu(111) as a model system, we investigated the physical relevance of the random displacement approach to SCM surface slab generation[23, 24]. Surface slabs were generated using both this approach and a highly accurate EAM potential, which has been shown to accurately describe copper bulk and surfaces[25]. Furthermore, we used this EAM potential to dynamically treat our surface, allowing us to both test the validity of the sudden approach as well as investigate any effect of energy exchange with the surface, which has long been theorised to be of little importance for this system[24]. Each calculation used the same CRP PES based on the SRP48 functional as had been used in previous studies, with the CM approaches all applying the effective 3-body potential as published by Spiering *et al.*[24].

We found good agreement between the dissociation curves of the RD-SCM and the EAM-SCM approaches, as well as with the EAM-DCM approach. Agreement was especially good for reaction curve onset, which has been shown to be the most accurate for experimental results, while the saturation value

was found to be lower for the two methods based on the EAM surface slabs. All three methods resulted in increased broadening of the dissociation S-curve compared to the BOSS approach, which is generally attributed to surface temperature effects.

Similar agreement was found for rovibrational (in)elastic scattering curves, where only the BOSS model significantly deviated from the results found with the different CM approaches. The good agreement between EAM-SCM and EAM-DCM indicated limited to no effect of energy exchange on the reaction and, more importantly, the (in)elastic scattering probabilities. Nevertheless, we did find a drain of 15% of the translational energy of the scattered molecules for almost the entire incidence energy range, which we have not found to be reported in other studies.

A further evaluation of the dissociation curves was performed by simulating a time-of-flight spectrum for each curve, through fitting to the LGS functional form and relying on detailed balance. Such a simulated spectrum is especially sensitive to reaction curve onset, as had been seen in an earlier study[16]. Again we found great agreement between the different CM approaches, as well as improved agreement with experiment[16] compared to the BOSS method.

To directly compare the surface slabs generated for the RD-SCM and EAM-SCM approaches, we mapped the displacements for each individual surface atom from its ideal lattice position, both for all trajectories and only for those trajectories that reacted. As expected, no preference was found for either method when considering the x- and y- coordinate, although the EAM generated slabs did show a much broader distribution of displacements. For the z-coordinate, however, we found a clear preference for reaction when the surface atoms are displaced away from the incoming D_2, but only for the EAM-SCM approach. Surface slabs generated using the RD-SCM did not even show Gaussian distributions in their displacement, as the displacement method only ensured a normal distribution in the total displacement of the atom.

In general we found good agreement between the reaction probabilities and rovibrational (in)elastic scattering probabilities obtained using the EAM-SCM and RD-SCM approaches, although the RD-SCM approach to surface generation showed much narrower atom displacement distributions. Furthermore, the good agreement with the non-static surface approach of EAM-DCM indicated both the very limited effect of energy exchange on the dissociation and (in)elastic scattering probabilities, despite having observed some energy drain into the surface.

With the success of the SCM sudden approach, combined with physically relevant surfaces generated with an EAM potential, we have opened a pathway towards quantum dynamically treating the motion of D_2 on a non-ideal Cu(111)

surface. Accurate quantum dynamically treatment of such systems would be a major step forward in describing the rovibrational (in)elastic scattering as well as the low incidence energy regime, which are dominated by quantum effects ill-described by QCT dynamics.

3

References

(1)   Luntz, A. C. In *Chemical Bonding at Surfaces and Interfaces*, Nilsson, A.,
      Pettersson, L. G. M., Nørskov, J. K., Eds.; Elsevier: Amsterdam, 2008,
      pp 143–254, DOI: `10.1016/B978-044452837-7.50004-6`.

(2)   Kroes, G.-J.; Somers, M. F. Six-dimensional dynamics of dissociative
      chemisorption of H_2 on metal surfaces. *Journal of Theoretical and Com-
      putational Chemistry* **2005**, *04*, 493–581, DOI: `10.1142/S021963360500`
      `1647`.

(3)   Kroes, G.-J.; Díaz, C. Quantum and classical dynamics of reactive scat-
      tering of H_2 from metal surfaces. *Chemical Society Reviews* **2016**, *45*,
      3658–3700, DOI: `10.1039/c5cs00336a`.

(4)   Smith, C.; Hill, A. K.; Torrente-Murciano, L. Current and future role
      of Haber–Bosch ammonia in a carbon-free energy landscape. *Energy &
      Environmental Science* **2020**, *13*, 331–344, DOI: `10.1039/C9EE02873K`.

(5)   Zambelli, T.; Barth, J. V.; Wintterlin, J.; Ertl, G. Complex pathways
      in dissociative adsorption of oxygen on platinum. *Nature* **1997**, *390*,
      495–497, DOI: `10.1038/37329`.

(6)   Anger, G.; Winkler, A.; Rendulic, K. D. Adsorption and desorption ki-
      netics in the systems H_2/Cu(111), H_2/Cu(110) and H_2/Cu(100). *Surface
      Science* **1989**, *220*, 1–17, DOI: `10.1016/0039-6028(89)90459-7`.

(7)   Hou, H.; Gulding, S. J.; Rettner, C. T.; Wodtke, A. M.; Auerbach, D. J.
      The Stereodynamics of a Gas-Surface Reaction. *Science* **1997**, *277*, 80–82,
      DOI: `10.1126/science.277.5322.80`.

(8)   Michelsen, H. A.; Rettner, C. T.; Auerbach, D. J.; Zare, R. N. Effect
      of rotation on the translational and vibrational energy dependence of
      the dissociative adsorption of D_2 on Cu(111). *The Journal of Chemical
      Physics* **1993**, *98*, 8294–8307, DOI: `10.1063/1.464535`.

(9)   Rettner, C. T.; Michelsen, H. A.; Auerbach, D. J. Quantum-state-specific
      dynamics of the dissociative adsorption and associative desorption of
      H_2 at a Cu(111) surface. *The Journal of Chemical Physics* **1995**, *102*,
      4625–4641, DOI: `10.1063/1.469511`.

(10) Hodgson, A.; Samson, P.; Wight, A.; Cottrell, C. Rotational Excitation
      and Vibrational Relaxation of H_2 Scattered from Cu(111). *Physical
      Review Letters* **1997**, *78*, 963–966, DOI: `10.1103/PhysRevLett.78.963`.

(11) Michelsen, H. A.; Auerbach, D. J. A critical examination of data on the dissociative adsorption and associative desorption of hydrogen at copper surfaces. *The Journal of Chemical Physics* **1991**, *94*, 7502–7520, DOI: 10.1063/1.460182.

(12) Cao, K.; Füchsel, G.; Kleyn, A. W.; Juurlink, L. B. F. Hydrogen adsorption and desorption from Cu(111) and Cu(211). *Physical Chemistry Chemical Physics* **2018**, *20*, 22477–22488, DOI: 10.1039/C8CP03386B.

(13) Kaufmann, S.; Shuai, Q.; Auerbach, D. J.; Schwarzer, D.; Wodtke, A. M. Associative desorption of hydrogen isotopologues from copper surfaces: Characterization of two reaction mechanisms. *The Journal of Chemical Physics* **2018**, *148*, 194703, DOI: 10.1063/1.5025666.

(14) Díaz, C.; Pijper, E.; Olsen, R. A.; Busnengo, H. F.; Auerbach, D. J.; Kroes, G. J. Chemically accurate simulation of a prototypical surface reaction: H_2 dissociation on Cu(111). *Science (New York, N.Y.)* **2009**, *326*, 832–834, DOI: 10.1126/science.1178722.

(15) Mondal, A.; Wijzenbroek, M.; Bonfanti, M.; Díaz, C.; Kroes, G.-J. Thermal Lattice Expansion Effect on Reactive Scattering of H_2 from Cu(111) at T_s = 925 K. *The Journal of Physical Chemistry A* **2013**, *117*, 8770–8781, DOI: 10.1021/jp4042183.

(16) Nattino, F.; Genova, A.; Guijt, M.; Muzas, A. S.; Díaz, C.; Auerbach, D. J.; Kroes, G.-J. Dissociation and recombination of D_2 on Cu(111): ab initio molecular dynamics calculations and improved analysis of desorption experiments. *The Journal of Chemical Physics* **2014**, *141*, 124705, DOI: 10.1063/1.4896058.

(17) Nattino, F.; Díaz, C.; Jackson, B.; Kroes, G.-J. Effect of Surface Motion on the Rotational Quadrupole Alignment Parameter of D_2 Reacting on Cu(111). *Physical Review Letters* **2012**, *108*, 236104, DOI: 10.1103/PhysRevLett.108.236104.

(18) Smeets, E. W. F.; Voss, J.; Kroes, G.-J. Specific Reaction Parameter Density Functional Based on the Meta-Generalized Gradient Approximation: Application to H_2 + Cu(111) and H_2 + Ag(111). *The Journal of Physical Chemistry A* **2019**, *123*, 5395–5406, DOI: 10.1021/acs.jpca.9b02914.

(19) Wijzenbroek, M.; Klein, D. M.; Smits, B.; Somers, M. F.; Kroes, G.-J. Performance of a Non-Local van der Waals Density Functional on the Dissociation of H_2 on Metal Surfaces. *The Journal of Physical Chemistry A* **2015**, *119*, 12146–12158, DOI: 10.1021/acs.jpca.5b06008.

(20)   Busnengo, H. F.; Salin, A.; Dong, W. Representation of the 6D potential energy surface for a diatomic molecule near a solid surface. *The Journal of Chemical Physics* **2000**, *112*, 7641–7651, DOI: 10.1063/1.481377.

(21)   Díaz, C.; Olsen, R. A.; Auerbach, D. J.; Kroes, G. J. Six-dimensional dynamics study of reactive and non reactive scattering of H_2 from Cu(111) using a chemically accurate potential energy surface. *Physical Chemistry Chemical Physics* **2010**, *12*, 6499–6519, DOI: 10.1039/C001956A.

(22)   Kroes, G.-J.; Díaz, C.; Pijper, E.; Olsen, R. A.; Auerbach, D. J. Apparent failure of the Born–Oppenheimer static surface model for vibrational excitation of molecular hydrogen on copper. *Proceedings of the National Academy of Sciences* **2010**, *107*, 20881–20886, DOI: 10.1073/pnas.1001098107.

(23)   Wijzenbroek, M.; Somers, M. F. Static surface temperature effects on the dissociation of H_2 and D_2 on Cu(111). *The Journal of Chemical Physics* **2012**, *137*, 054703, DOI: 10.1063/1.4738956.

(24)   Spiering, P.; Wijzenbroek, M.; Somers, M. F. An improved static corrugation model. *The Journal of Chemical Physics* **2018**, *149*, 234702, DOI: 10.1063/1.5058271.

(25)   Sheng, H. W.; Kramer, M. J.; Cadien, A.; Fujita, T.; Chen, M. W. Highly optimized embedded-atom-method potentials for fourteen fcc metals. *Physical Review B* **2011**, *83*, 134118, DOI: 10.1103/PhysRevB.83.134118.

(26)   Sementa, L.; Wijzenbroek, M.; van Kolck, B. J.; Somers, M. F.; Al-Halabi, A.; Busnengo, H. F.; Olsen, R. A.; Kroes, G. J.; Rutkowski, M.; Thewes, C.; Kleimeier, N. F.; Zacharias, H. Reactive scattering of H_2 from Cu(100): Comparison of dynamics calculations based on the specific reaction parameter approach to density functional theory with experiment. *The Journal of Chemical Physics* **2013**, *138*, 044708, DOI: 10.1063/1.4776224.

(27)   Füchsel, G.; Cao, K.; Er, S.; Smeets, E. W. F.; Kleyn, A. W.; Juurlink, L. B. F.; Kroes, G.-J. Anomalous Dependence of the Reactivity on the Presence of Steps: Dissociation of D_2 on Cu(211). *The Journal of Physical Chemistry Letters* **2018**, *9*, 170–175.

(28)   Smeets, E. W. F.; Füchsel, G.; Kroes, G.-J. Quantum Dynamics of Dissociative Chemisorption of H_2 on the Stepped Cu(211) Surface. *The Journal of Physical Chemistry C* **2019**, *123*, 23049–23063, DOI: 10.1021/acs.jpcc.9b06539.

(29) Boereboom, J. M.; Wijzenbroek, M.; Somers, M. F.; Kroes, G. J. Towards a specific reaction parameter density functional for reactive scattering of H $_2$ from Pd(111). *The Journal of Chemical Physics* **2013**, *139*, 244707, DOI: `10.1063/1.4851355`.

(30) Behler, J. First Principles Neural Network Potentials for Reactive Simulations of Large Molecular and Condensed Systems. *Angewandte Chemie International Edition* **2017**, *56*, 12828–12840, DOI: `https://doi.org/10.1002/anie.201703114`.

(31) Verlet, L. Computer "Experiments" on Classical Fluids. I. Thermodynamical Properties of Lennard-Jones Molecules. *Physical Review* **1967**, *159*, 98–103, DOI: `10.1103/PhysRev.159.98`.

(32) Berendsen, H. J. C.; Postma, J. P. M.; van Gunsteren, W. F.; Di Nola, A.; Haak, J. R. Molecular dynamics with coupling to an external bath. *The Journal of Chemical Physics* **1984**, *81*, 3684–3690, DOI: `10.1063/1.448118`.

(33) Bulirsch, R.; Stoer, J. Numerical treatment of ordinary differential equations by extrapolation methods. *Numerische Mathematik* **1966**, *8*, 1–13, DOI: `10.1007/BF02165234`.

(34) Tsai, D. H. The virial theorem and stress calculation in molecular dynamics. *The Journal of Chemical Physics* **1979**, *70*, 1375–1382, DOI: `10.1063/1.437577`.

(35) *Dynamics of Gas-Surface Interactions: Atomic-level Understanding of Scattering Processes at Surfaces*; Muino, R. D., Busnengo, H. F., Eds.; Springer Series in Surface Sciences; Springer-Verlag: Berlin Heidelberg, 2013, DOI: `10.1007/978-3-642-32955-5`.

(36) Kroes, G.-J.; Juaristi, J. I.; Alducin, M. Vibrational Excitation of H$_2$ Scattering from Cu(111): Effects of Surface Temperature and of Allowing Energy Exchange with the Surface. *The Journal of Physical Chemistry C* **2017**, *121*, 13617–13633, DOI: `10.1021/acs.jpcc.7b01096`.

(37) Dohle, M.; Saalfrank, P. Surface oscillator models for dissociative sticking of molecular hydrogen at non-rigid surfaces. *Surface Science* **1996**, *373*, 14.

(38) Wang, Z. S.; Darling, G. R.; Holloway, S. The surface temperature dependence of the inelastic scattering and dissociation of hydrogen molecules from metal surfaces. *The Journal of Chemical Physics* **2004**, *120*, 2923–2933, DOI: `10.1063/1.1636724`.

(39)   Wijzenbroek, M.; Kroes, G. J. An ab initio molecular dynamics study of D $_2$ dissociation on CO-precovered Ru(0001). *Physical Chemistry Chemical Physics* **2016**, *18*, 21190–21201, DOI: 10.1039/C6CP00291A.

(40)   Bonfanti, M.; Somers, M. F.; Díaz, C.; Busnengo, H. F.; Kroes, G.-J. 7D Quantum Dynamics of H_2 Scattering from Cu(111): The Accuracy of the Phonon Sudden Approximation. *Zeitschrift für Physikalische Chemie* **2013**, 130617035227002, DOI: 10.1524/zpch.2013.0405.

(41)   Henkelman, G.; Jónsson, H. Theoretical Calculations of Dissociative Adsorption of CH_4 on an Ir(111) Surface. *Physical Review Letters* **2001**, *86*, 664–667, DOI: 10.1103/PhysRevLett.86.664.

(42)   Tiwari, A. K.; Nave, S.; Jackson, B. Methane Dissociation on Ni(111): A New Understanding of the Lattice Effect. *Physical Review Letters* **2009**, *103*, 253201, DOI: 10.1103/PhysRevLett.103.253201.

(43)   Nave, S.; Jackson, B. Methane dissociation on Ni(111) and Pt(111): Energetic and dynamical studies. *The Journal of Chemical Physics* **2009**, *130*, 054701, DOI: 10.1063/1.3065800.

Quantum dynamical surface temperature effects on the dissociative chemisorption of H_2 from Cu(111)

Abstract

Accurately describing surface temperature effects for the dissociative scattering of H_2 on a metal surface at a quantum dynamical level is currently one of the open challenges for theoretical surface scientists. We present the first quantum dynamical (QD) simulations of hydrogen dissociating on a Cu(111) surface which accurately describe all relevant surface temperature effects, using the static corrugation model (SCM). The reaction probabilities we obtain show very good agreement with those found using quasi-classical dynamics (QCD) both for individual surface slabs and for an averaged, thus Monte-Carlo sampled, set of thermally distorted surface configurations. Rovibrationally elastic scattering probabilities show a much clearer difference between the QCD and QD results, which appears to be traceable back towards thermally distorted surface configurations with very low dissociation probabilities. This underlines the importance of investigating more observables than just dissociation. By

reducing the number of distorted surface atoms included in the dynamical model, we also show that only including one, or even three, surface atoms is generally not enough to accurately describe the effects of surface temperature on dissociation and elastic scattering. These results are a major step forward in accurately describing hydrogen scattering from a thermally excited Cu(111) surface. They open up a pathway to better describe reaction and scattering from other relevant crystal facets, such as stepped surfaces, at moderately elevated surface temperatures where quantum effects are expected to play a more important role in the dissociation of H$_2$ on Cu.

4.1   Introduction

One of the major focuses in the field of theoretical heterogeneous catalysis simulations is the accurate description of surface temperature effects on gas-solid reactive scattering[1–13]. These are especially of interest as they form an important basis for many industrial processes, such as the Haber-Bosch process [14] or H$_2$ powered engines[15]. To gain the most accurate description, these processes are broken down into their elementary steps, and a focus is put on describing each step individually.

In the past one often relied on the Born-Oppenheimer static surface (BOSS) approximation, where the surface is assumed to be both fully static and with the atoms in their ideal lattice positions, and electron and nucleus dynamics assumed to be fully separable[1]. Dynamics is performed using a 6D potential energy surface (PES) where all H$_2$ degrees of freedom are included, which is fit to density functional theory (DFT) results using i.e. the corrugation reducing procedure (CRP)[16]. These fitting procedures, however, often cannot or do not take into account the distorted nature of a thermally excited surface, while the relevant industrial processes, and experimental studies, are performed at elevated surface temperatures.

Nevertheless, some approaches do exist that can take these surface effects into account. These include a variety of methods including static distortion models and phonon baths studied by Busnengo *et al.*, and Jackson *et al.* for the CH$_4$ dissociation reaction [5, 7, 9–11, 17, 18]. Other approaches include the static disorder parameter by Manson and co-workers[19], the effective Hartree potential by Dutta *et al.*[12, 20], as well as the more general ring polymer molecular dynamics[21, 22] and high-dimensional neural network potential (HD-NNP) approaches[23–26].

HD-NNPs, in particular, are currently an intensively studied method to describing the PES, and have been shown to be usable in a wide variety of systems[23]. However, in our experience HD-NNPs also often still require

dense data sets, as extrapolation beyond the available dataset can yield wildly unexpected results. Careful planning in determining the appropriate symmetry functions[23]. While significant speed-ups can be achieved using these NNPs compared to AIMD simulations, we find they are generally not computationally fast enough to be used in state-of-the-art quantum dynamics (QD) simulations. Furthermore, none have yet been tested thoroughly by also computing accurate rotational and vibrational inelastic scattering or diffraction probabilities compared to experimental data[27–29]. As such, we believe HD-NNPs have not yet achieved the balance between speed and accuracy required for our application.

The system of choice in this thesis is the dissociative chemisorption of H_2 on a (thermally excited) Cu(111) surface, a particularly well studied model system, which would allow for a comparison to a wide range of both theoretical[3, 4, 8, 25, 30–34] and experimental [35–40] results. In particular, this system is being experimentally revisited by Alexandrowicz and co-workers, who have recently measured sharply defined state-to-state diffraction probabilities with their molecular interferometry setup[40–43]. Previous experimental work by Kaufmann *et al.* has also fully characterised a slow reaction channel of the H_2/Cu(111) system[39]. This reaction channel shows a strong temperature and vibrational dependency[37, 38], but has to our knowledge not yet been observed in theoretical studies.

Furthermore, using the specific reaction parameter (SRP) approach to DFT, Díaz *et al.* were already able to reproduce experimental molecular beam results to within 1 kcal / mol with the BOSS model[30]. The static corrugation model (SCM) further improved this BOSS model by adding an accurate description of surface temperature effects to quasi-classical dynamics (QCD) of H_2 dissociating on a Cu(111) surface[2]. The addition of a highly accurate embedded atom method (EAM) potential to generate thermally distorted surface slabs (Chapter 3) finally improved upon previous iterations of the SCM, which relied on random displacements to generate surface slabs[2, 3]. The introduction of the EAM potential also allowed for an explicit inclusion of surface motion into QCD using the dynamic corrugation model (DCM), as was shown in Chapter 3. Reaction and scattering probabilities obtained with this EAM-SCM and EAM-DCM show great agreement with experimental results and clearly demonstrated the validity of the sudden approximation for the H_2 on Cu(111) system.

Thus, the SCM is a prime candidate for introducing all relevant vibrational degrees of freedom into quantum dynamical simulations without also introducing a very large computational cost associated with introducing many more dynamical variables related to the surface atoms. Quantum effects are expected to be especially important for the description of accurate state-resolved

scattering probabilities, in particular for stepped surfaces such as Cu(211)[44]. Quantum effects are also expected to be important for an accurate description of (initially) rovibrationally excited H_2 molecules, or when considering lower surface temperatures (T_s). State-resolved scattering, rovibrationally excited molecules and lower surface temperatures are all important for describing industrial applications or reproducing experimental results. Potentials obtained using the SCM have also shown to be smooth enough to allow for an accurate description of both higher rovibrational states as well as state-resolved inelastic scattering probabilities[2–4]. However, the molecular dynamics used to generate surface slabs, as has been done using the EAM potential for $T_s = 925$ K, is not expected to yield accurate displacements for surface temperatures lower than 300 K[45].

The sudden approximation that lies at the basis of the SCM is expected to work best at a large mass mismatch between the reactant and the surface atom, and at shorter interaction times with the surface. However for those systems where the mass mismatch between H atoms and the transition metal atoms is very large, even the longer surface interaction times could likely be modeled accurately enough with a static surface. Electronic friction due to elecron-hole pair excitations is not included in our model as has been shown to not have a major effect for the H_2/Cu(111) system[46]. However, for other systems it might have to be included, which is currently only possible at a classical level[47–49].

In this Chapter, I present the use of the EAM-SCM to include all relevant surface temperature effects of the dissociation and rovibrationally elastic scattering of H_2 on a 925 K Cu(111) surface employing QD instead of QCD for the dynamics. First, the effect of constraining the H_2 molecule to a specific (1×1) unit cell using QCD will be discussed. Next, comparisons will be made between the reaction and elastic scattering probabilities obtained with QD and QCD, both for BOSS and EAM-SCM. For the EAM-SCM results, the probabilities curves are compared both for individual distorted slabs and as an average over all the slabs considered. This should shed light on the effect and importance of quantum effects, of H_2 and of the surface within a sudden approximation. Finally, the effect of displacing only a single or a limited number of surface atoms on the accurate description of the surface temperature effects is investigated.

4.2   Method

In this chapter, we will make use of the SCM as discussed in section 2.3.1 of Chapter 2 to describe the thermal surface effect of the H_2 chemisorption on

Cu(111), using both the QD TDWP approach as described in section 2.1.3 (QD-EAM-SCM) and the quasi-classical dynamics approach expanded upon in section 2.2.1 (QCD-EAM-SCM). The ideal lattice 6D PES that describes the perfect lattice surface interacting with the H_2 molecule is obtained from a corrugation reducing procedure (CRP) fit to density functional theory (DFT) results. This DFT dataset was obtained using the SRP48 exchange-correlation functional[8, 13]. The effective three-body coupling potential of the SCM, which expands the PES to include thermal lattice distortions, is also fitted to SRP48 DFT results[3]. Only those surface atoms within 16 bohrs (~ 8.47 Å) of the unit cell corner (U, V, Z)=(0, 0, 0) and within the top two layers of the distorted surface slab were included for the calculation of the SCM potential, as was done in the previous chapter.

4.2.1   Quantum dynamics

We obtain reaction and elastic scattering probabilities using QD for a total of 104 thermally distorted surface slabs. These slabs were acquired from unique traces of molecular dynamics using the EAM potential[45], as was described in Chapter 3. The reaction and scattering probabilities are averaged to get a single representative dissociation or elastic scattering probability curve of H_2 dissociating on, or scattering from, a thermally excited Cu(111) surface.

The reactive scattering of the H_2 is fast compared to the motion of the surface atoms, and the mass mismatch between the H and Cu atoms is very large. Thus, the hydrogen molecule and the solid represent two (thermally) separate systems, with the solid equilibrated to the surface temperature of 925 K, but the H_2 not. This would mean that the effects of the (quantum) dynamics of the surface on the reactive scattering of the H_2 can be (implicitly) included by using the sudden approximation. This is achieved by Monte-Carlo sampling many different surface degrees-of-freedom associated with the $\sim$70 surface atoms included in a typical SCM potential evaluation.

Compared to purely classical dynamics, the QD-SCM does not suffer from an incorrect redistribution of internal energies of both the solid and the hydrogen (especially when including a thermostat), or from erroneous use of Maxwell-Boltzmann statistics for the surface atoms at lower temperatures. The large amount of surface atoms that can be included with the SCM also provide a clear advantage over other approximate quantum dynamical studies, which generally make use of reduced degrees-of-freedom of the solid[33, 50], or describe the dynamics of the surface using a few Hartree products as anzats[12, 20]. Furthermore, with no need for a harmonic oscillator approximation for the

surface, the SCM allows for thermal expansion effects of the solid to be included, which have been shown to be clearly of relevance[2].

Evenmore, for the SCM and low surface temperatures, one could use the phonon displacement vectors to sample surface configurations with the correct Bose-Einstein statistics. Assuming one uses the proper periodic boundary conditions and the quasi-harmonic approximation[51]. This allows for a more direct comparison to earlier[52] and more recent state of the art diffraction experiments[40, 43] using a full quantum description of both H_2 and the solid, albeit within the sudden approximation where energy exchange is not taken into account.

For each individual surface configuration, the QD reaction or elastic scattering curve is obtained via three different wave packets, one with an energy range from 0.10 to 0.30 eV, $0.25-0.70$ eV, and from $0.65-1.00$ eV. Details regarding the computational parameters for each of these wave packets are described in the appendix (6.A) of Chapter 6.

4.2.2   Quasi-classical dynamics

These QD simulations fully including all relevant surface temperature effects are compared to QCD calculations. Surface atom displacements for the EAM-SCM approach are randomly selected from the total database of 25.000 surface configurations constructed in Chapter 3. Propagation is performed using the Bulirsch-Stoer predictor-corrector algorithm [53], ending when the two H atoms move more than 2.25 Å apart for a reactive trajectory, or when the Z c.m. coordinate is further than 7 Å from the surface for a scattered trajectory. For each incidence energy a total of 50.000 trajectories were performed, each using a unique surface configuration in the QCD-EAM-SCM. Additionally, each of the 104 surface configurations used in QD-EAM-SCM were also separately investigated with 50.000 trajectories per incidence energy using QCD-EAM-SCM.

In this chapter we also investigate the effect of applying a minimum image convention to the c.m. of the incoming H_2 molecule. When the c.m. moves further outside of the boundaries of 0 to a in both the lattice U and V coordinates, it is mapped back into the (1×1) unit cell when computing the PES and/or the forces associated with it. This makes the actual PES used in the dynamics to be translation symmetric when the molecule leaves the (1×1) unit cell. This translation symmetry constraint on the dynamics of H_2 is investigated in detail in order to verify the use of a single (1×1) unit cell in the QD. The SCM corrugation V_{coup} interaction could be influenced by such a symmetry constraint, as it is only diminished beyond approximately 10 bohrs /

5.5 Å (see the $P7$ parameter of Eq. 2.57)[3]. The use of a single (1×1) unit cell reduces the computational demands for the QD enormously. This is vital, as with the current approach to Monte-Carlo sample over at least 100 individual surfaces we present here entail a computationally challenging task, even when using the (1×1) single unit cell approximation.

4.2.3 Limited atom static corrugation model

In past works models to include surface atom degrees of freedom often focused primarily on distorting one, or a few, of the degrees of freedom (DoF) of the surface atom closest to the reactant impact site[10, 11, 33, 34, 54]. To investigate the quality of such an assumption for our system, we aim to also investigate the effect of only including a small number of surface atoms on the reaction and elastic scattering probabilities obtained using the EAM-SCM. Instead of using all atoms found within the 16 bohrs (~ 8.47 Å) SCM cutoff radius described earlier in the methods section, distorted surface atoms are ranked based on their distance from the middle of the top layer of the (1×1) unit cell [(U, V, Z)=($\frac{a}{2}$, $\frac{a}{2}$, 0)]. Only a limited number of surface atoms are then included in the model, while all others are kept at their ideal lattice positions. This procedure allows us to easily navigate the approximations one makes if including only a limited number of surface DoFs at both the QCD as well as the QD level of theory. This method we will refer to as the limited atom SCM, or NAt-EAM-SCM. Here N stands for the number of surface atoms included, in this work 1At, 3At and 5At, for one, three and five surface atoms respectively.

4.3 Results and discussion

By comparing results from QD and QCD simulations of the dissociative chemisorption of H_2 on Cu(111), we aim to verify the quality of the SCM approach to including surface temperature effects into the QD simulations of the hydrogen molecule. Our focus will be on the rovibrational ground state of H_2, in particular comparing the results obtained using the QD-EAM-SCM and QCD-EAM-SCM approaches. The QD-EAM-SCM implements the QD of H_2 directly and fully correlated, but as stated before, the QD of the surface atom degrees of freedom are treated on a sudden approximation level using Monte-Carlo sampling. The QCD-EAM-SCM uses QCD for the dynamics of H_2 and again treats the dynamics of the surface on the same sudden approximation level, but with many more unique surface samples included compared to QD-EAM-SCM. In Chapter 3, the QCD-EAM-SCM was also validated (for D_2) to the DCM, where the surface was allowed to move. It was found that

the energy exchange possible in the DCM, but not in the SCM, was negligible (for D$_2$, which as a higher mass than H$_2$). We are therefore confident that the sudden approximation of the SCM for H$_2$ will hold even better, and allow us to perform the QD-EAM-SCM, via Monte-Carlo sampling, on such a scale.

The surface configurations we use in this EAM-SCM approach, both for the QCD and QD, were obtained from classical dynamics using the EAM potential at a modeled surface temperature of 925 K. This surface temperature was chosen to be able to compare to experimental results [32, 36], but is also well within the classical regime for this Cu system. This implies the correct use of the Maxwell-Boltzmann statistics, inherent to molecular dynamics, in the effective Monte-Carlo sampling in both QCD-EAM-SCM and QD-EAM-SCM.

4.3.1   Constrained results

One of the main constraints of our QD implementation is the size of the unit cell that can feasibly be used in the time-dependent wave packet (TDWP) method. Moving from a (1×1) to a (2×2) unit cell would already increase computational costs by a factor of four. While a small unit cell can easily be used with the BOSS approach, due to the periodicity of the ideal surface lattice, the same can not be assumed when thermally distorting the lattice. Therefore, we first investigated the effect of constraining the H$_2$ molecule to a (1×1) unit cell of the surface using, computationally much cheaper, QCD simulations. This translation symmetry constraint was simply implemented by always mapping the H$_2$ c.m. U and V coordinates into the single (1×1) unit cell before calculating the actual PES and the forces derived from it.

In Figure 4.1, we show the reaction and elastic scattering probabilities obtained with QCD for the H$_2$ on a Cu(111) surface at a modeled surface temperature of 925 K. Included are both the (1×1) unit cell constrained (1×1)-EAM-SCM and the unconstrained EAM-SCM results, for the (a) rovibrational ground state as well as a (b) vibrationally, (c) rotationally, and (d) rovibrationally excited initial state. Agreement between the constrained and non-constrained EAM-SCM results seems perfect for all four rovibrational states included, both for the reaction and elastic scattering probabilities. This excellent agreement confirms that the SCM does still yield accurate results when the H$_2$ molecule is constrained within a (1×1) unit cell of the surface for QCD, and likely also for QD.
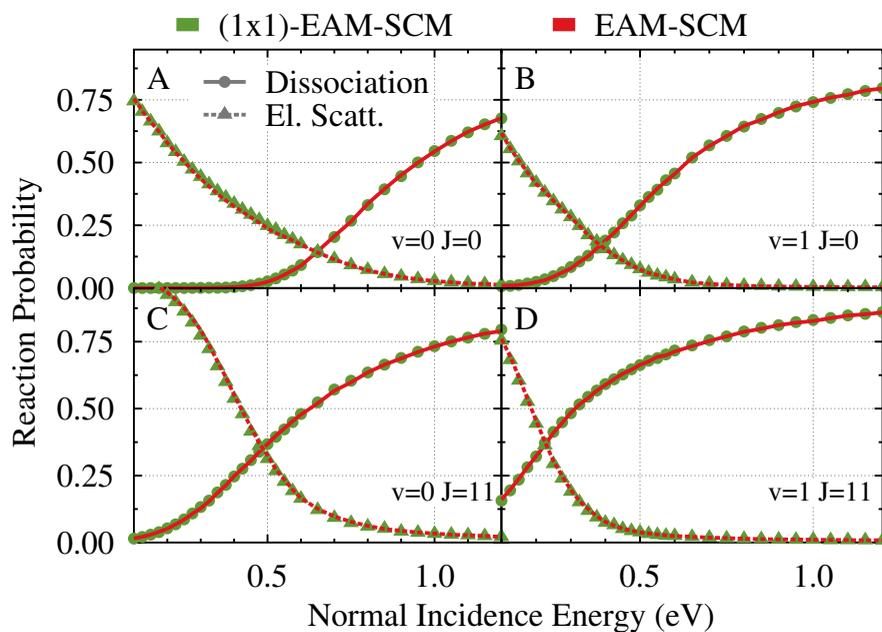
FIGURE 4.1: Reaction and rovibrationally elastic scattering probabilities obtained using both the (1×1)-EAM-SCM (green circles) and regular EAM-SCM (red curves). Reaction is shown as solid circles and lines, while the elastic scattering is shown as triangles and dashed lines. Included are: (a) the rovibrational ground state v = 0, J = 0; (b) a vibrationally excited state v = 1, J = 0; (c) a rotationally excited state v = 0, J = 11; and (d) a rovibrationally excited state v = 1, J = 11. The system of choice is H_2 reacting on a thermally distorted Cu(111) surface at a modeled surface temperature of 925 K.

4
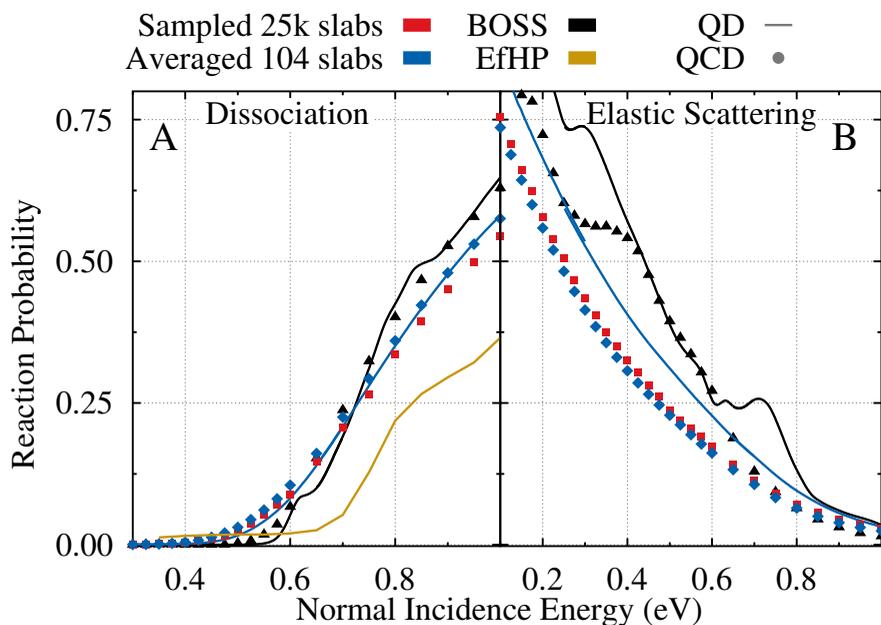
FIGURE 4.2: Reaction (a) and rovibrationally elastic scattering (b) probability curves for the H$_2$ in the rovibrational ground state (v = 0, J = 0) on a Cu(111) surface. Included are results obtained using the EAM-SCM both for a random sampling over all 25000 surface slabs with QCD (red squares), and an average of 104 selected surface slabs using both QD (blue curve) and QCD (blue diamonds). BOSS results for QD and QCD are shown as a black curve and black triangles, respectively. Finally reaction probabilities from other work by Adhikari *et al*, obtained using the QD EfHP approach[12], are shown as a yellow curve. For the EAM-SCM and EfHP results, a modeled surface temperature of 925 K is used.

4.3.2 Dissociative chemisorption and rovibrationally elastic scattering

With confirmation that the SCM still yields accurate results for H_2 constrained to a small (1×1) unit cell, we next include the EAM-SCM into our QD calculations. In Figure 4.2, we display the reaction (a) and rovibrationally elastic scattering (b) probability curves for the QD-EAM-SCM model, obtained as an average of calculations on 104 unique EAM generated surface slabs at a modeled surface temperature of 925 K. QCD-EAM-SCM results, obtained as an average of these 104 surface slabs, are also included. These results are also compared to QCD-EAM-SCM results obtained from randomly selecting surfaces out of the 25000 surface slabs available, as was done in Chapter 3. This allows us to get an estimate on the error we can expect when only including such a relatively low amount of unique surface slabs into our QD-EAM-SCM model. Furthermore, we also compare our results to those obtained by Dutta *et al.*, who applied their EfHP method to include thermal surface displacements into QD simulations for the same $H_2/Cu(111)$ system[12]. They also used the same underlying BOSS CRP PES and SCM V_{coup} potentials, all based on the same SRP48 DFT functional, and exactly the same TDWP code. Finally, we also include results obtained using the perfect lattice BOSS approach both with QD and QCD, as has often been investigated in the past.

As expected, each dissociation probability curve shows a slow build-up at low incidence energy as most incoming adsorbates do not have enough energy to pass over the reaction barrier. At higher incidence energies, we find a mostly linear relation between the incidence energy and reaction, which will then eventually level off to a saturation value at energies well out of the plotted range. Only the QD-BOSS results show a slight deviation in this analysis, with a small "bump" in reaction probability around a normal incidence energy of 0.7 eV. The EfHP results displays by far the lowest reactivity, which can be explained by this model only including thermal displacements and not lattice expansion, as well as making other approximations related to the effective Hartree approach[2, 12]. Agreement between the reaction probabilities obtained for the 104 surface slabs compared to the results for a random selection of 25.000 surface slabs for QCD-EAM-SCM is good. This implies only a small error is expected in our QD-EAM-SCM results due to the relatively few surface slabs used. However some small variation is observed, indicating better results could be obtained if the number of included surface slabs is increased. Clearly this is possible at the expense of using more computational resources by simply running more TDWP QD runs. We have chosen, in view of the limited time, for using ~100 surfaces for the QD-EAM-SCM and by estimating the error by

simply comparing to QCD-EAM-SCM results.

The QCD-EAM-SCM and the QD-EAM-SCM results show a much earlier curve onset, while also not increasing as steeply towards their maximum value, when compared to BOSS curves. This broadening of the reaction probability curve is generally associated with surface temperature effects, which we also show in Chapter 3 for the D_2/Cu(111) system, and is discussed in previous work[2, 32, 55]. Furthermore, the agreement between the QCD-EAM-SCM and QD-EAM-SCM results is also very good, with the QD curve displaying slightly less broadening. This is a strong indication of an accurate description of thermal surface effects in our QD results. However, this agreement is not perfect and thus also demonstrates subtle quantum effects do already come into play for the reaction of hydrogen on a 925 K copper surface.

When we consider the elastic scattering in Figure 4.2(b), we observe much less subtle quantum effects. Again the agreement between the scattering probabilities obtained for the 104 surface slabs compared to the results for a random selection of 25000 surface slabs for QCD-EAM-SCM is good. The BOSS results show some variation between QCD and QD, although this can be mostly attributed to the "bumps" we see around 0.3 and 0.7 eV, which we previously also showed for D_2 in Chapter 3.

A clear difference is visible when comparing the QD-EAM-SCM and QCD-EAM-SCM results, where QD shows a much higher probability for elastic scattering at lower incidence energies. This observation underlines the importance of properly investigating a system using QD, and shows the limited information available when only reaction probabilities are investigated and compared. Furthermore, these quantum effects could become even more important for higher initial rovibrational states of the H_2, especially for rovibrational inelastic scattering and/or diffraction. It is also expected to be especially important for lower surface temperatures or scattering reactions from stepped surfaces [Cu(211)]. Unfortunately, this has not been investigated thoroughly yet, partly due to the computational challenges associated with these systems.

However, the SCM approach (for H_2 and D_2), and the use of the scattering amplitude formalism in the QD are expected to really shines here.

To further investigate the quality of the QD dynamics compared to our QCD results, we take a closer look at the reaction and elastic scattering results on a few individual thermally distorted surface slabs. Especially of interest are those surfaces where the dissociation probability is either much higher or lower than on average. This allows us to validate the model not just on average when Monte-Carlo sampling over many surface configurations, but also for the specific edge cases it will have to deal with.
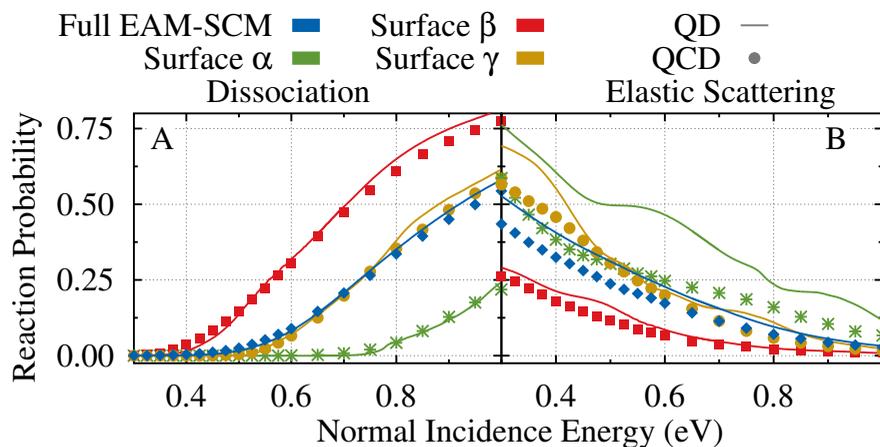
FIGURE 4.3: Reaction (a) and rovibrationally elastic scattering (b) probabilities for three specific thermally excited surface slabs, and the average of all investigated distorted surface slabs. A a modeled surface temperature of 925 K was used with the incident H_2 in the rovibrational ground state. Results for surface α, β, and γ are shown as green stars and curves, red squares and curves, and yellow circles and curves, respectively. The results for the averaged probabilities obtained using the EAM-SCM are shown as blue curves and diamonds. The curves represent the QD results, while the symbols represent the QCD results. For the full EAM-SCM results, the QD curves consist of an average of 104 surface slabs, while the QCD results are obtained from random sampling of all 25.000 distorted surface slabs.

In Figure 4.3(a), we show reaction probabilities for three different surface slabs: not very reactive (surface α), very reactive (surface β) and typical (surface γ). Also included are the averaged results for all the EAM-SCM distorted surface slabs.

For dissociation, we again see the characteristic S-curve shape, with the results for the more reactive surface slab β already levelling off towards a saturation value. In contrast, the curve the less reactive surface slab α just passed the curve onset and is reaching the linear part of the S-curve. Overall, the agreement between the QCD results as symbols and the QD results as a line is excellent. As was the case for the Monte-Carlo sampled results, we see a small decrease in curve broadness for QD compared to QCD, which is more visible for the results of slab β than for the other two.

In general, we see no great variation in the agreement between QCD and QD when we compare the reaction probabilities found for the individual surface slabs to those obtained for the general average. However, no such claim can be made for the elastic scattering probabilities, as can be seen in Figure 4.3(b). We find great agreement between the rovibrationally elastic scattering probabilities obtained using the reactive surface slab β, better than that of the averaged results. In contrast, the agreement between the QD and QCD probabilities found for the typical slab γ are close in line to that found for the full average of all surface slabs. Finally, the probabilities found for the less reactive surface slab α show the largest difference between the QD- and QCD-EAM-SCM. This appears to indicate that the differences between the QD and QCD elastic scattering probabilities we find in Figure 4.2(b). are primarily caused by those surface slabs that have a much higher barrier due to the thermal distortion of the surface. However, further studies, also including more surface slabs into the QD-EAM-SCM, will be required to fully understand this phenomenon.

4.3.3   Limited surface atom degrees of freedom

In previous studies, the effect of including surface atom degrees of freedom were often described through the displacement of a single surface atom, or even a single DoF of a single surface atom[10, 11, 33]. While such an approach is computationally very efficient, it is not too clear if all thermal surface effects can be described through such a small number of degrees of freedom, or even a single one. Using the EAM-SCM, we are able to selectively include or exclude the contribution of specific distorted surface atoms. With this, we aim to investigate the effect of reducing the number of surface atoms taken into account for the thermal surface effects of the H_2 on Cu(111) system, both in QD and QCD.

In Figure 4.4, we show the reaction and rovibrationally elastic scattering probabilities obtained with QD- and QCD-EAM-SCM when only including one, three or five thermally distorted Cu(111) surface atoms. The surface atoms to include were selected based on their distance from the center of the (1×1) Cu(111) surface unit cell, starting with the closest surface atom. Also included are the results of the full EAM-SCM model, which includes ∼70 surface atoms depending on the specific distorted surface slab used, and the BOSS results.

Again, agreement between reaction probabilities obtained QD-EAM-SCM and QCD-EAM-SCM appears to be very good, even for those results where less surface atoms are included in the model. We also see a clear decrease in elastic scattering probabilities obtained with QD-EAM-SCM compared to QCD-EAM-SCM for all the EAM-SCM results. However, there is also a clear difference between the EAM-SCM results where less surface atoms are taken into account, both for reaction and scattering probabilities. In particular, the scattering and dissociation curves show much more "BOSS-like" probabilities, with less of the broadening usually attributed to surface temperature effects, when only a single surface atom is thermally displaced. Adding two more surface atoms to the model already greatly increases agreement with the full EAM-SCM model, although there is still a noticeable discrepancy with the results obtained from the full model. Finally, the 5At-EAM-SCM results show excellent agreement with the full model This appears to indicate that correctly implementing surface temperature effects will require at least five surface atoms to be included to get accurate results for the H_2 on Cu(111) system when including a modeled surface temperature of 925 K. The observation that using only five surface atoms already gives such good results correlates with the effectiveness of only using a single (1×1) unit cell for the QD, as only ∼10 surface atoms are found within the ∼7 bohrs (∼3.7 Å) distance where V_{coup} contributes significantly towards the potential energy of the PES[3]. This is an important characteristic to keep in mind when designing new models for including surface temperature, although it is currently unclear if this characteristic is specific for our system, or even the model used to describe it.

4.4 Conclusion

We investigated the quality of the EAM-SCM in quantum dynamical calculations to accurately describe all relevant surface temperature effects. Dissociation and rovibrationally elastic scattering probabilities were computed, using both QCD and QD, for the H_2 on Cu(111) system at a modeled surface temperature of 925 K for the rovibrational ground state. Similar the previous chapter a CRP PES based on the SRP48 functional was used, which has been shown to be

4
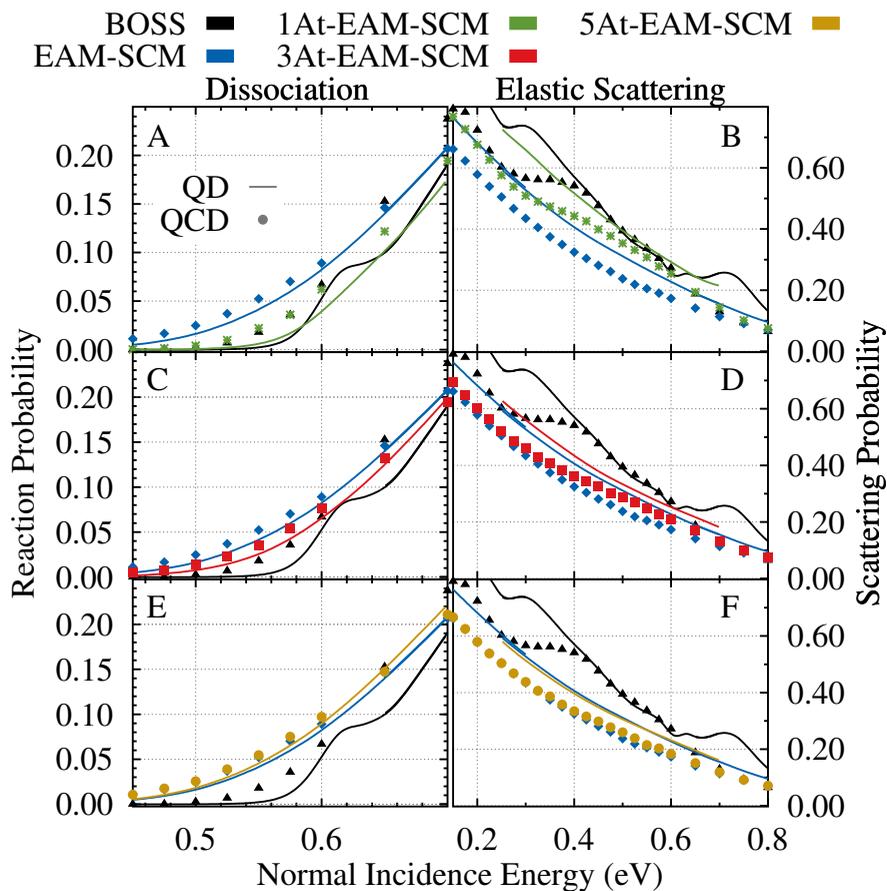
FIGURE 4.4: Reaction [(a), (c), and (e)] and rovibrationally elastic scattering [(b), (d), and (f)] probabilities obtained for the 1At-, 3At- and 5At-EAM-SCM approach, as well as the full EAM-SCM and the BOSS approaches. Here, 1At, 3At, and 5At refer to the number of surface atoms included into the EAM-SCM, and are shown as green stars and curves [(a) and (b)], as red squares and curves [(c) and (d)], and as yellow circles and curves [(e) and (f)], respectively. The BOSS results are included as black curves and triangles, and the full surface EAM-SCM results are shown as blue diamonds and curves. The curves represent the QD results, while the symbols represent the QCD results. The QD curves consist of an average of 104 surface slabs, for the EAM-SCM results with one, three, five, and all thermally distorted surface atoms (within the cutoff) included consist of an average of 104 surface slabs. The QCD results are obtained from random sampling of all 25.000 distorted surface slabs.

chemically accurate[30]. The SCM coupling potential was described using the effective three-body potential as published by Spiering *et al.*[3]. The surface configurations used were obtained with molecular dynamics using a highly accurate EAM potential[45], as is described in Chapter 3.

Before implementing the SCM into our QD calculations, we first investigated the effect of constraining the H_2 molecule to a (1×1) unit cell, as much larger cells are computationally unfeasible for QD. Reaction and elastic scattering probabilities obtained using QCD and a variety of rovibrational states showed excellent agreement between those simulations where the H_2 molecules were and were not constrained.

With confirmation that the SCM would yield accurate results, even when such a small unit cell is used, we next included the EAM-SCM into our quantum dynamics. Both the QCD and QD reaction probability curves obtained using the SCM showed the characteristic curve broadening compared to the BOSS results found when surface temperature effects are taken into account. Furthermore, the QCD- and QD-EAM-SCM results showed great agreement with each other when considering reaction probabilities, which indicates the quality of the quasi-classical approach for this system and observable. The QD-EAM-SCM results did display a very slight decrease in curve broadening compared to the QCD results, which clearly indicates a quantum effect that could be of importance. The QD-EAM-SCM elastic scattering probabilities were found to be significantly higher than the QCD results, which could indicate an important quantum effect for this system. In contrast, for the BOSS model the difference in scattering probability was much less apparent, which could indicate a role of surface temperature effects or our model in particular.

To further investigate this difference between QD and QCD, we next compared reaction and scattering probabilities obtained for several specific distorted surfaces using the EAM-SCM. A highly reactive, a less reactive, and a typical surface slab were chosen for comparison, to get an overview of the different types of surface slabs available. Again reaction probabilities were found to have great agreement between QD and QCD, even for the three specific surface slabs, although the highly reactive slab again displayed a small difference in curve broadness between QD-EAM-SCM and QCD-EAM-SCM. Interestingly, elastic scattering probabilities obtained for the typical and highly reactive surface configurations also showed great agreement between the QCD and QD results, whereas as clear difference between QCD and QD was found only for the less reactive surface configuration. This could indicate the difference in elastic scattering probabilities found is primarily caused by those surfaces that show a low reactivity, although further work would be required to fully investigate this finding.

Finally, we aimed at getting a better understanding of surface atom degrees of freedom that play a relevant role in describing the surface temperature effects with the SCM approach. Reaction and elastic scattering probabilities were obtained using EAM-SCM where only one, three or five surface atoms where thermally displaced. These probabilities were then compared to those obtained using both the BOSS model and the full EAM-SCM. We found that including the thermal distortions of only one surface atom into the system was not sufficient to accurately describing the surface temperature effects of the system, with this approach more closely resembling the BOSS results than the EAM-SCM results. Only when a total of five surface atom degrees of freedom were included in the model did we find close to an accurate description of the thermally distorted surface. A clear difference was already found between the elastic scattering probabilities obtained using QD and QCD even for those curves where only a single distorted surface was included in the EAM-SCM, however.

Previous work has already shown that the underlying DFT functional of V_{coup} is transferable between different facets of the copper surface[44, 56]. This opens up the opportunity to expand this work further towards the Cu(100) facet and eventually the Cu(211) stepped surface. However, the number of surface slabs in the Monte-Carlo sampling in this work were quite limited (104), and as such we expect to obtain more definitive results once more QD-EAM-SCM simulations can be performed, also including results from different initial rovibrational states of H_2. Additional work is also required to allow for accurate results of reactive scattering from surface slabs below approximately 300 K[45]. Here the classical MD approach to generating slabs with the EAM is expected not to give accurate results, predominantly because the use of a thermostat that extracts the zero point energy from the Cu system, but also from implicitly employing a Maxwell-Boltzmann statistical sampling of the phonons that are actually bosons and adhere to the Bose-Einstein statistics[12].

References

(1) Kroes, G.-J.; Díaz, C. Quantum and classical dynamics of reactive scattering of H_2 from metal surfaces. *Chemical Society Reviews* **2016**, *45*, 3658–3700, DOI: 10.1039/c5cs00336a.

(2) Wijzenbroek, M.; Somers, M. F. Static surface temperature effects on the dissociation of H_2 and D_2 on Cu(111). *The Journal of Chemical Physics* **2012**, *137*, 054703, DOI: 10.1063/1.4738956.

(3) Spiering, P.; Wijzenbroek, M.; Somers, M. F. An improved static corrugation model. *The Journal of Chemical Physics* **2018**, *149*, 234702, DOI: 10.1063/1.5058271.

(4) Smits, B.; Somers, M. F. Beyond the static corrugation model: Dynamic surfaces with the embedded atom method. *The Journal of Chemical Physics* **2021**, *154*, 074710, DOI: 10.1063/5.0036611.

(5) Jackson, B. Quantum studies of methane-metal inelastic diffraction and trapping: The variation with molecular orientation and phonon coupling. *Chemical Physics* **2022**, *559*, 111516, DOI: 10.1016/j.chemphys.2022.111516.

(6) Kroes, G.-J. Computational approaches to dissociative chemisorption on metals: towards chemical accuracy. *Physical Chemistry Chemical Physics* **2021**, *23*, 8962–9048, DOI: 10.1039/D1CP00044F.

(7) Xiao, Y.; Dong, W.; Busnengo, H. F. Reactive force fields for surface chemical reactions: A case study with hydrogen dissociation on Pd surfaces. *The Journal of Chemical Physics* **2010**, *132*, 014704, DOI: 10.1063/1.3265854.

(8) Mondal, A.; Wijzenbroek, M.; Bonfanti, M.; Díaz, C.; Kroes, G.-J. Thermal Lattice Expansion Effect on Reactive Scattering of H_2 from Cu(111) at T_s = 925 K. *The Journal of Physical Chemistry A* **2013**, *117*, 8770–8781, DOI: 10.1021/jp4042183.

(9) Seminara, G. N.; Peludhero, I. F.; Dong, W.; Martínez, A. E.; Busnengo, H. F. Molecular Dynamics Study of Molecular and Dissociative Adsorption Using System-Specific Force Fields Based on Ab Initio Calculations: CO/Cu(110) and CH_4/Pt(110). *Topics in Catalysis* **2019**, *62*, 1044–1052, DOI: 10.1007/s11244-019-01196-9.

(10) Tiwari, A. K.; Nave, S.; Jackson, B. The temperature dependence of methane dissociation on Ni(111) and Pt(111): Mixed quantum-classical studies of the lattice response. *The Journal of Chemical Physics* **2010**, *132*, 134702, DOI: 10.1063/1.3357415.

(11)   Guo, H.; Farjamnia, A.; Jackson, B. Effects of Lattice Motion on Dissociative Chemisorption: Toward a Rigorous Comparison of Theory with Molecular Beam Experiments. *The Journal of Physical Chemistry Letters* **2016**, *7*, 4576–4584, DOI: `10.1021/acs.jpclett.6b01948`.

(12)   Dutta, J.; Mandal, S.; Adhikari, S.; Spiering, P.; Meyer, J.; Somers, M. F. Effect of surface temperature on quantum dynamics of H_2 on Cu(111) using a chemically accurate potential energy surface. *The Journal of Chemical Physics* **2021**, *154*, 104103, DOI: `10.1063/5.0035830`.

(13)   Nattino, F.; Díaz, C.; Jackson, B.; Kroes, G.-J. Effect of Surface Motion on the Rotational Quadrupole Alignment Parameter of D_2 Reacting on Cu(111). *Physical Review Letters* **2012**, *108*, 236104, DOI: `10.1103/PhysRevLett.108.236104`.

(14)   Smith, C.; Hill, A. K.; Torrente-Murciano, L. Current and future role of Haber–Bosch ammonia in a carbon-free energy landscape. *Energy & Environmental Science* **2020**, *13*, 331–344, DOI: `10.1039/C9EE02873K`.

(15)   Zambelli, T.; Barth, J. V.; Wintterlin, J.; Ertl, G. Complex pathways in dissociative adsorption of oxygen on platinum. *Nature* **1997**, *390*, 495–497, DOI: `10.1038/37329`.

(16)   Busnengo, H. F.; Salin, A.; Dong, W. Representation of the 6D potential energy surface for a diatomic molecule near a solid surface. *The Journal of Chemical Physics* **2000**, *112*, 7641–7651, DOI: `10.1063/1.481377`.

(17)   Lozano, A.; Shen, X. J.; Moiraghi, R.; Dong, W.; Busnengo, H. F. Cutting a chemical bond with demon's scissors: Mode- and bond-selective reactivity of methane on metal surfaces. *Surface Science* **2015**, *640*, 25–35, DOI: `10.1016/j.susc.2015.04.002`.

(18)   Jackson, B. The Trapping of Methane on Ir(111): A First-Principles Quantum Study. *The Journal of Chemical Physics* **2021**, *155*, 044705, DOI: `10.1063/5.0058672`.

(19)   Kroes, G. J.; Wijzenbroek, M.; Manson, J. R. Possible effect of static surface disorder on diffractive scattering of H_2 from Ru(0001): Comparison between theory and experiment. *The Journal of Chemical Physics* **2017**, *147*, 244705, DOI: `10.1063/1.5011741`.

(20)   Dutta, J.; Naskar, K.; Adhikari, S.; Spiering, P.; Meyer, J.; Somers, M. F. Effect of surface temperature on quantum dynamics of D_2 on Cu(111) using a chemically accurate potential energy surface, To Be Submitted, 2022, submitted.

(21) Craig, I. R.; Manolopoulos, D. E. Quantum Statistics and Classical Mechanics: Real Time Correlation Functions from Ring Polymer Molecular Dynamics. *The Journal of Chemical Physics* **2004**, *121*, 3368–3373, DOI: 10.1063/1.1777575.

(22) Suleimanov, Y. V.; Aoiz, F. J.; Guo, H. Chemical Reaction Rate Coefficients from Ring Polymer Molecular Dynamics: Theory and Practical Applications. *The Journal of Physical Chemistry A* **2016**, *120*, 8488–8502, DOI: 10.1021/acs.jpca.6b07140.

(23) Behler, J. First Principles Neural Network Potentials for Reactive Simulations of Large Molecular and Condensed Systems. *Angewandte Chemie International Edition* **2017**, *56*, 12828–12840, DOI: https://doi.org/10.1002/anie.201703114.

(24) Artrith, N.; Behler, J. High-dimensional neural network potentials for metal surfaces: A prototype study for copper. *Physical Review B* **2012**, *85*, 045439, DOI: 10.1103/PhysRevB.85.045439.

(25) Zhu, L.; Zhang, Y.; Zhang, L.; Zhou, X.; Jiang, B. Unified and transferable description of dynamics of H_2 dissociative adsorption on multiple copper surfaces *via* machine learning. *Physical Chemistry Chemical Physics* **2020**, *22*, 13958–13964, DOI: 10.1039/D0CP02291H.

(26) Lin, Q.; Zhang, L.; Zhang, Y.; Jiang, B. Searching Configurations in Uncertainty Space: Active Learning of High-Dimensional Neural Network Reactive Potentials. *Journal of Chemical Theory and Computation* **2021**, *17*, 2691–2701, DOI: 10.1021/acs.jctc.1c00166.

(27) Somers, M. F.; Olsen, R. A.; Busnengo, H. F.; Baerends, E. J.; Kroes, G. J. Reactive scattering of H_2 from Cu(100): Six-dimensional quantum dynamics results for reaction and scattering obtained with a new, accurately fitted potential-energy surface. *The Journal of Chemical Physics* **2004**, *121*, 11379–11387, DOI: 10.1063/1.1812743.

(28) Cueto, M. d.; Muzas, A. S.; Somers, M. F.; Kroes, G. J.; Díaz, C.; Martín, F. Exploring surface landscapes with molecules: rotationally induced diffraction of H_2 on LiF(001) under fast grazing incidence conditions. *Physical Chemistry Chemical Physics* **2017**, *19*, 16317–16322, DOI: 10.1039/C7CP02904G.

(29) Muzas, A. S.; del Cueto, M.; Gatti, F.; Somers, M. F.; Kroes, G. J.; Martín, F.; Díaz, C. H_2LiF(001) diffractive scattering under fast grazing incidence using a DFT-based potential energy surface. *Physical Review B* **2017**, *96*, 205432, DOI: 10.1103/PhysRevB.96.205432.

4

(30)   Díaz, C.; Pijper, E.; Olsen, R. A.; Busnengo, H. F.; Auerbach, D. J.; Kroes, G. J. Chemically accurate simulation of a prototypical surface reaction: H$_2$ dissociation on Cu(111). *Science (New York, N.Y.)* **2009**, *326*, 832–834, DOI: `10.1126/science.1178722`.

(31)   Díaz, C.; Olsen, R. A.; Auerbach, D. J.; Kroes, G. J. Six-Dimensional Dynamics Study of Reactive and Non Reactive Scattering of H$_2$ from Cu(111) Using a Chemically Accurate Potential Energy Surface. *Physical Chemistry Chemical Physics* **2010**, *12*, 6499–6519, DOI: `10.1039/C0019 56A`.

(32)   Nattino, F.; Genova, A.; Guijt, M.; Muzas, A. S.; Díaz, C.; Auerbach, D. J.; Kroes, G.-J. Dissociation and recombination of D$_2$ on Cu(111): ab initio molecular dynamics calculations and improved analysis of desorption experiments. *The Journal of Chemical Physics* **2014**, *141*, 124705, DOI: `10.1063/1.4896058`.

(33)   Bonfanti, M.; Somers, M. F.; Díaz, C.; Busnengo, H. F.; Kroes, G.-J. 7D Quantum Dynamics of H$_2$ Scattering from Cu(111): The Accuracy of the Phonon Sudden Approximation. *Zeitschrift für Physikalische Chemie* **2013**, 130617035227002, DOI: `10.1524/zpch.2013.0405`.

(34)   Kroes, G.-J.; Juaristi, J. I.; Alducin, M. Vibrational Excitation of H$_2$ Scattering from Cu(111): Effects of Surface Temperature and of Allowing Energy Exchange with the Surface. *The Journal of Physical Chemistry C* **2017**, *121*, 13617–13633, DOI: `10.1021/acs.jpcc.7b01096`.

(35)   Michelsen, H. A.; Rettner, C. T.; Auerbach, D. J.; Zare, R. N. Effect of rotation on the translational and vibrational energy dependence of the dissociative adsorption of D$_2$ on Cu(111). *The Journal of Chemical Physics* **1993**, *98*, 8294–8307, DOI: `10.1063/1.464535`.

(36)   Rettner, C. T.; Michelsen, H. A.; Auerbach, D. J. Quantum-state-specific dynamics of the dissociative adsorption and associative desorption of H$_2$ at a Cu(111) surface. *The Journal of Chemical Physics* **1995**, *102*, 4625–4641, DOI: `10.1063/1.469511`.

(37)   Hou, H.; Gulding, S. J.; Rettner, C. T.; Wodtke, A. M.; Auerbach, D. J. The Stereodynamics of a Gas-Surface Reaction. *Science* **1997**, *277*, 80–82, DOI: `10.1126/science.277.5322.80`.

(38)   Murphy, M. J.; Hodgson, A. Adsorption and desorption dynamics of H$_2$ and D$_2$ on Cu(111): The role of surface temperature and evidence for corrugation of the dissociation barrier. *The Journal of Chemical Physics* **1998**, *108*, 4199–4211, DOI: `10.1063/1.475818`.

(39) Kaufmann, S.; Shuai, Q.; Auerbach, D. J.; Schwarzer, D.; Wodtke, A. M. Associative desorption of hydrogen isotopologues from copper surfaces: Characterization of two reaction mechanisms. *The Journal of Chemical Physics* **2018**, *148*, 194703, DOI: 10.1063/1.5025666.

(40) Chadwick, H.; Somers, M. F.; Stewart, A. C.; Alkoby, Y.; Carter, T. J. D.; Butkovicova, D.; Alexandrowicz, G. Stopping Molecular Rotation Using Coherent Ultra-Low-Energy Magnetic Manipulations. *Nature Communications* **2022**, *13*, 2287, DOI: 10.1038/s41467-022-29830-3.

(41) Godsi, O.; Corem, G.; Alkoby, Y.; Cantin, J. T.; Krems, R. V.; Somers, M. F.; Meyer, J.; Kroes, G.-J.; Maniv, T.; Alexandrowicz, G. A general method for controlling and resolving rotational orientation of molecules in molecule-surface collisions. *Nature Communications* **2017**, *8*, 15357, DOI: 10.1038/ncomms15357.

(42) Alkoby, Y.; Chadwick, H.; Godsi, O.; Labiad, H.; Bergin, M.; Cantin, J. T.; Litvin, I.; Maniv, T.; Alexandrowicz, G. Setting benchmarks for modelling gas–surface interactions using coherent control of rotational orientation states. *Nature Communications* **2020**, *11*, 3110, DOI: 10.1038/s41467-020-16930-1.

(43) Chadwick, H.; Alkoby, Y.; Cantin, J. T.; Lindebaum, D.; Godsi, O.; Maniv, T.; Alexandrowicz, G. Molecular spin echoes; multiple magnetic coherences in molecule surface scattering experiments. *Physical Chemistry Chemical Physics* **2021**, *23*, 7673–7681, DOI: 10.1039/D0CP05399F.

(44) Smeets, E. W. F.; Füchsel, G.; Kroes, G.-J. Quantum Dynamics of Dissociative Chemisorption of H_2 on the Stepped Cu(211) Surface. *The Journal of Physical Chemistry C* **2019**, *123*, 23049–23063, DOI: 10.1021/acs.jpcc.9b06539.

(45) Sheng, H. W.; Kramer, M. J.; Cadien, A.; Fujita, T.; Chen, M. W. Highly optimized embedded-atom-method potentials for fourteen fcc metals. *Physical Review B* **2011**, *83*, 134118, DOI: 10.1103/PhysRevB.83.134118.

(46) Spiering, P.; Meyer, J. Testing Electronic Friction Models: Vibrational De-excitation in Scattering of H_2 and D_2 from Cu(111). *The Journal of Physical Chemistry Letters* **2018**, *9*, 1803–1808, DOI: 10.1021/acs.jpclett.7b03182.

(47) Füchsel, G.; Klamroth, T.; Monturet, S.; Saalfrank, P. Dissipative Dynamics within the Electronic Friction Approach: The Femtosecond Laser Desorption of H_2/D_2 from Ru(0001). *Physical Chemistry Chemical Physics* **2011**, *13*, 8659, DOI: 10.1039/c0cp02086a.

(48)   Maurer, R. J.; Jiang, B.; Guo, H.; Tully, J. C. Mode Specific Electronic Friction in Dissociative Chemisorption on Metal Surfaces: H$_2$ on Ag(111). *Physical Review Letters* **2017**, *118*, 256001, DOI: `10.1103/PhysRevLett.118.256001`.

(49)   Spiering, P.; Shakouri, K.; Behler, J.; Kroes, G.-J.; Meyer, J. Orbital-Dependent Electronic Friction Significantly Affects the Description of Reactive Scattering of N$_2$ from Ru(0001). *The Journal of Physical Chemistry Letters* **2019**, *10*, 2957–2962, DOI: `10.1021/acs.jpclett.9b00523`.

(50)   Smits, B.; Litjens, L. G. B.; Somers, M. F. Accurate Description of the Quantum Dynamical Surface Temperature Effects on the Dissociative Chemisorption of H$_2$ from Cu(111). *The Journal of Chemical Physics* **2022**, *156*, 214706, DOI: `10.1063/5.0094985`.

(51)   Togo, A.; Tanaka, I. First Principles Phonon Calculations in Materials Science. *Scripta Materialia* **2015**, *108*, 1–5, DOI: `10.1016/j.scriptamat.2015.07.021`.

(52)   Farias, D.; Rieder, K.-H. Atomic Beam Diffraction from Solid Surfaces. *Reports on Progress in Physics* **1998**, *61*, 1575, DOI: `10.1088/0034-4885/61/12/001`.

(53)   Bulirsch, R.; Stoer, J. Numerical treatment of ordinary differential equations by extrapolation methods. *Numerische Mathematik* **1966**, *8*, 1–13, DOI: `10.1007/BF02165234`.

(54)   Busnengo, H. F.; Di Césare, M. A.; Dong, W.; Salin, A. Surface Temperature Effects in Dynamic Trapping Mediated Adsorption of Light Molecules on Metal Surfaces: H 2 on Pd(111) and Pd(110). *Physical Review B* **2005**, *72*, 125411, DOI: `10.1103/PhysRevB.72.125411`.

(55)   *Dynamics of Gas-Surface Interactions: Atomic-level Understanding of Scattering Processes at Surfaces*; Muino, R. D., Busnengo, H. F., Eds.; Springer Series in Surface Sciences; Springer-Verlag: Berlin Heidelberg, 2013, DOI: `10.1007/978-3-642-32955-5`.

(56)   Sementa, L.; Wijzenbroek, M.; van Kolck, B. J.; Somers, M. F.; Al-Halabi, A.; Busnengo, H. F.; Olsen, R. A.; Kroes, G. J.; Rutkowski, M.; Thewes, C.; Kleimeier, N. F.; Zacharias, H. Reactive scattering of H$_2$ from Cu(100): Comparison of dynamics calculations based on the specific reaction parameter approach to density functional theory with experiment. *The Journal of Chemical Physics* **2013**, *138*, 044708, DOI: `10.1063/1.4776224`.

Chapter 5

The quantum dynamics of H$_2$ on Cu(111) at a surface temperature of 925 K: Comparing theory to experiments

Abstract

We present results of our recently expanded static corrugation model (SCM) approach that included the relevant surface temperature effects, applied to the dissociative chemisorption reaction of H$_2$ on a Cu(111) surface. The reaction and rovibrationally elastic scattering probabilities that we obtain at a quantum dynamical (QD) level, as an average of many statically distorted surface configurations, show great agreement with those of a dynamic surface model. This greatly reinforces the validity of the sudden approximation inherent to the SCM. We further investigate several simple methods of binning the final rovibrational state of quasi-classical dynamics simulations to find those best suited to reproduce the QD results for our system. Finally, we show that the SCM obtained results reproduce experimental dissociation curves very well when the uncertainty in experimental saturation values is taken into account. Some indication of a slow channel, so far only observed in experiment, can also

be found at low incidence energies, although more rigorous QD simulations are required to reduce the noise inherent to our propagation methods.

5.1 Introduction

Heterogeneous catalysis is one of the backbones of modern life, being vital in processes such as steam reforming, for H_2 production, and the Haber-Bosch process, for the production of fertilisers[1, 2]. Here the accurate modelling of gas-surface dissociation reactions is an important topic, as it is often the rate-limiting elementary step in these reactions[3]. Past works often relied on simple static and ideal surface models to describe the elementary reactions, neglecting the potentially important effects of energy exchange with the surface or thermal distortion of the surface. As industrial heterogeneous catalysis processes generally take place well above 0 K, further gains in the description of these simple dissociation reactions can be attained by finding accurate models for describing surface temperature effects[4].

For this chapter, our system of choice is once again the dissociative chemisorption of H_2 on a (thermally excited) Cu(111) surface. This system is one of the model systems in the field of surface science, with an array of experimental[5–12] and theoretical[13–26] data available. In particular, Kaufmann *et al.* recently presented experimental results that allowed them to fully characterise a slow reaction channel for the system, which shows strong temperature and vibrational dependencies, but has not yet been observed in any theoretical works[11]. Similarly, Chadwick *et al.* recently published sharply defined state-to-state diffraction probabilities at a surface temperature of 130 K, using their molecular interferometry setup[12, 27].

For this chapter we have chosen to make use of the SCM approach to describe the effect of surface temperature on the H_2/Cu(111) system, as it has been shown to be accurate at both a QC and a QD level for not only dissociation but also rovibrationally elastic scattering probabilities[15, 18]. Our ideal lattice 6D potential energy surface (PES) of choice was fitted by Nattino *et al.* using the corrugation reducing procedure (CRP)[28], with a dataset obtained using density functional theory (DFT) and the SRP48 functional[29]. SRP48 has already shown to reproduce experimental results to within chemical accuracy with the Born-Oppenheimer static surface (BOSS) approach, where the electron and nuclear dynamics are assumed to be fully separable and the surface atoms are kept static at their ideal lattice positions[30]. The SCM then expands on this potential through the addition of a coupling potential, also fit to SRP48 DFT data, which describes the effect of distorting the surface due to thermal effects[20]. Surface configurations are obtained using an embedded

atom method (EAM) potential, which has been shown to accurately reproduce various observables for the copper surface[31]. Electronic friction due to electron-hole pair excitations has been shown to not be relevant for this system, and is thus not included in this model[32].

One of the main assumptions of this EAM-SCM approach is that the Cu(111) surface dynamics can be treated at a sudden approximation level, where the surface atoms are not allowed to move. However, the EAM potential can also be used to describe surface motion during dynamics, as the EAM-SCM could be further expanded to the dynamic corrugation model (DCM). Previous work comparing the results obtained with the EAM-SCM and EAM-DCM [for D_2 on Cu(111)] validated the sudden approximation that lies at the base of the SCM, and proved the limited effect energy exchange with the surface has on this system[15]. Recent work has also shown the SCM to hold well when applied to 6D QD simulations with a statically distorted surface, when treating the incoming H_2 at its rovibrational ground state, although there were some clear differences found between the QC and QD results for the rovibrationally elastic scattering probabilities[18].

While we will only treat the H_2/Cu(111) system, the EAM-SCM approach is expected to be general enough to be used for the reaction of other diatomic molecules reacting on a transition metal surface. In particular, the model is expected to perform well when energy exchange with the surface plays only a minimal effect, either due to a large mass mismatch between the surface atoms and the reactant, and/or due to short interaction times with the surface. It also relies on the availability of (a dataset of) accurate DFT results that can be used to both construct the BOSS PES, and fit the required SCM potential to statically include the surface temperature effects. For Cu, in particular, previous work has already shown that the SRP48 functional is transferable to other Cu facets, and thus would be an excellent target for future work[33, 34]. The thermally distorted surface configurations needed for the SCM can be obtained from a variety of sources, such as simple force-fields methods, or constructed using, for example, the Debye-Waller factor[20]. For those systems where energy exchange with the surface is important the DCM would be required, which would then also require a potential to accurate describe the motion of the surface atoms. This has, however, only been tested for the H_2 and D_2 on Cu systems so far, and is only computationally viable at a (quasi-)classical level due to the large number of surface DoF involved[15]. Similarly, we expect electronic frictions models to be able to expand the EAM-SCM, although this is currently also only possible at a classical dynamics level[35–37].

In this chapter I present dissociation and elastic scattering probabilities of H_2 on a (thermally distorted) Cu(111) surface slab, obtained using the BOSS

approach and EAM-SCM approach at a modeled surface temperature of 925 K, both using QD and QCD simulations. To complement the results of the previously published rovibrational ground state (of H_2), we now also investigate several initial rovibrationally excited states. Static surface EAM-SCM results are compared to EAM-DCM results where the surface is allowed to move, to further verify the quality of the sudden approximation for this system [which had so far only been shown for the D_2/Cu(111) system]. Several rovibrational binning methods are applied to the final classical state of the QCD results, and compared to the exact quantised 6D simulations to verify the quality of these binning methods when applied to the H_2/Cu(111) system. Finally, the QD- and QCD-EAM-SCM dissociation probability curves are compared to those obtained from the direct inversion of desorption experiments at the same surface temperature, both at higher incidence energies and at very low reaction probabilities near the curve onset.

5.2 Method

In this chapter, we will continue on the results of Chapter 4, now including QD and QCD results for (ro)vibrationally excited initial states. For the QD and QCD results we once again make use of the TDWP approach and the quasi-classical dynamics approach as discussed in respectively sections 2.1.3 and 2.2.1 of Chapter 2. We will also compare to dissociation and scattering probabilities obtained using the moving surface EAM-DCM approach.

The same SRP48 CRP PES as used in the previous chapters is again applied, as well as the effective three-body SCM coupling potential as described by Spiering *et al.*[25]. Similarly, the database of thermally distorted surface slabs, constructed as described in Chapter 3, is used to obtain the EAM-SCM (and -DCM) surface configurations, with the same 16 bohrs ($\sim$ 8.47 Å) cutoff distance.

5.2.1 Quantum dyanmics

To obtain a single representative dissociation or scattering curve for H_2 reacting with thermally distorted Cu(111) at a QD level, we average the probabilities obtained for a total of 104 unique thermally distorted surface slabs. By averaging over the results obtained from these thermally distorted surface slabs, the quantum dynamics of the surface atom degrees of freedom is effectively done on a sudden approximation level using Monte-Carlo sampling. Thus we essentially perform QD implicitly even for the surface degrees of freedom, but with the approximation that energy exchange between H_2 and the surface is not possible.

Furthermore, there is also no energy exchange possible between the vibrations within the solid during the individual QD TDWP runs, making sure that any classical redistribution or leaking of zero point energy is not possible at all. This is where we think the SCM shines compared to other models, employing thermostats and/or other RPMD assumptions (i.e. using Boltzmann statistics and harmonic potentials) especially relevant for $T_s < 300$ K for Cu.

For each individual surface configuration, the QD reaction or elastic scattering curve is obtained via three different WPs, one with an energy range 0.10 to 0.30 eV, another 0.25–0.70 eV, and a third 0.65–1.00 eV, as already used in the previous chapter on the rovibrational ground state. For the initial rotationally excited states only those states with $mJ \geq 0$ were considered, with the results for $mJ \neq 0$ counted twice in the total average per rotational state, to account for the $mJ < 0$ states. Details regarding the computational parameters for each of these wave packets can be found in the appendix (6.A) of Chapter 6.

5.2.2 Final state binning

There will also be a bigger focus on different methods of binning the final rovibrational state of the QCD calculations, as also outlined in 2.2.4 of Chapter 2. Here first the modulus of the classical angular momentum ($|L_f|$) is calculated

$$|L_f|^2 = p_\theta{}^2 + \frac{p_\phi{}^2}{\sin^2\theta} \tag{5.1}$$

where p_θ and p_ϕ describe the conjugate momenta along the two molecular angles. This angular momentum is then used to determine a classical "rotational state"

$$J_f = \frac{\sqrt{1 + 4|L_f|^2} - 1}{2} \tag{5.2}$$

which is found by equating $|L_f|^2$ to $J(J+1)$.

Next this classical state is binned using one of three methods. Using the standard binning method, which is how we have performed the binning in previous studies, the rotational state is binned to the closest allowed J state, keeping in mind the selection rule for the rotational state of our diatomic molecule: $\Delta J = \pm 2$. With the weighted binning method, the integer rotational state closest to J_f is chosen, and given a weight of $W_i = 2$ when it is allowed, or $W_i = 0$ when it is not allowed, with i for the ith trajectory performed, effectively ignoring any trajectory with a disallowed transition[38]. Assuming an equal distribution over all possible classical rotational energies, this would yield an average total weight equal to the number of trajectories performed. Finally,

with the floor binning method the classical rotational state J_f is rounded downward towards the first allowed J state, keeping in mind the selection rule. For both the standard and floor binning, $W_i = 1$ is always chosen for every trajectory.

With the rotational state (J) determined, the vibrational state (v) is chosen by finding the rovibrational state that is closest in total rovibrational energy to the states allowed by the binned rotational state. Trajectories are considered rovibrationally elastically scattered when the final rovibrational state of H_2 is binned to the same state as its initial state, and rovibrationally inelastically scattered when the binned final state is not the same as the initial rovibrational state. The m_J state is not taken into account at all for the final state, as it is degenerate with the other possible m_J states.

Reaction and (state-to-state) scattering probabilities are then determined by dividing the weight of each by the weight of all trajectories. For the standard and floor binning methods, these probabilities are equal to dividing the number of reacted or scattered trajectories by the total number of trajectories performed.

5.2.3   Comparisons to experiment

We will also compare our theoretical dissociation curves to those reported in several experimental studies[7, 8, 11]. The experimental results we discuss are all obtained from direct inversion of time of flight (ToF) results obtained from desorption experiments. These inverted data are then fitted to a functional form, which range from very simplistic to quite advanced. Here we will only concern ourselves with the very simple error function

$$S(v, J, T_s, E_{kin}) = \frac{A(v, J)}{2}\Big[1 + \text{erf}\Big(\frac{E_{kin} - E_0(v, J)}{W(v, J)}\Big)\Big] \qquad (5.3)$$

where the three fitted variables A, E_0, and W are the saturation value, inflection point and width respectively. While absolute E_0 and W parameters can be directly obtained from these inverted ToF spectra, the same cannot be said for the saturation value, for which only relative values can be found directly. Thus experimental studies often fit their curves under the assumption of a saturation value of $A = 1$, while both experimental and theoretical adsorption studies rarely ever find such a value. Furthermore, care should be taken when scaling the curves to different saturation values, as some previous studies have found these three parameters to be not entirely independent[20]. Both references [7] and [11] have also used beam adsorption experiments to determine absolute saturation values for their surfaces. It is, however, unclear if these can be

directly applied to their experimental desorption data, due to differences in experimental setup, including surface temperature.

Finally, Kaufmann *et al.* also identified a slow reaction channel, which was fit separately using

$$S_{slow}(v, J, E_{kin}) = A_{slow}(v, J) \exp\left(\frac{-E_{kin}}{\gamma(v, J)}\right) \tag{5.4}$$

where A_{slow} defines the amplitude, and γ a decay parameter[11]. The older works by Rettner *et al.*[7] and Hodgson *et al.*[8] we compare to, as well as all theoretical works to date, did not find this separate channel.

5.3   Results and discussion

5.3.1   Rovibrationally excited states and a dynamic surface

First we will compare the reaction probability curves obtained for both the EAM-SCM and EAM-DCM at a QC level to those obtained using QD-EAM-SCM. Chapter 4 has already shown that the QD- and QCD-EAM-SCM results show excellent agreement for the rovibrational ground state of H_2. However, this has not yet been verified for the rovibrationally excited states or when also considering the moving surface of the EAM-DCM, as previous comparisons between QCD-EAM-SCM and -DCM were only performed for the D_2 scattering reaction[15]. In Figure 5.1, we show some of the reaction probabilities previously obtained for the rovibrational ground state (a), as well as a rotationally excited initial state [(c); v, J = 0, 2]. Similarly for panels (b) and (d) we show the results obtained for the vibrationally excited (v = 1) state, with J = 0 and J = 2, respectively. Next to the QCD- and QD-EAM-SCM results, we also included the QCD- and QD-BOSS results, as well as the QCD-EAM-DCM results.

As expected, the agreement between QCD and QD, both for the BOSS and EAM-SCM results, is very good, with some minor differences in curve width more prominently visible for the vibrationally excited states. The small fluctuations in the SRP48 CRP PES are much more clearly visible for the QD-BOSS results, compared to the QD-EAM-SCM. This is primarily attributed to the averaging over many surfaces we perform to obtain accurate surface temperature effects, as this will smooth out these smaller inconsistencies in the results. The agreement between the QCD-EAM-SCM and -DCM (and thus also with the QD-EAM-SCM) results is again excellent, as was already shown for the D_2/Cu(111) system. This observation is perhaps not too surprising, as the mass mismatch between H_2 and the Cu surface is even bigger than that of
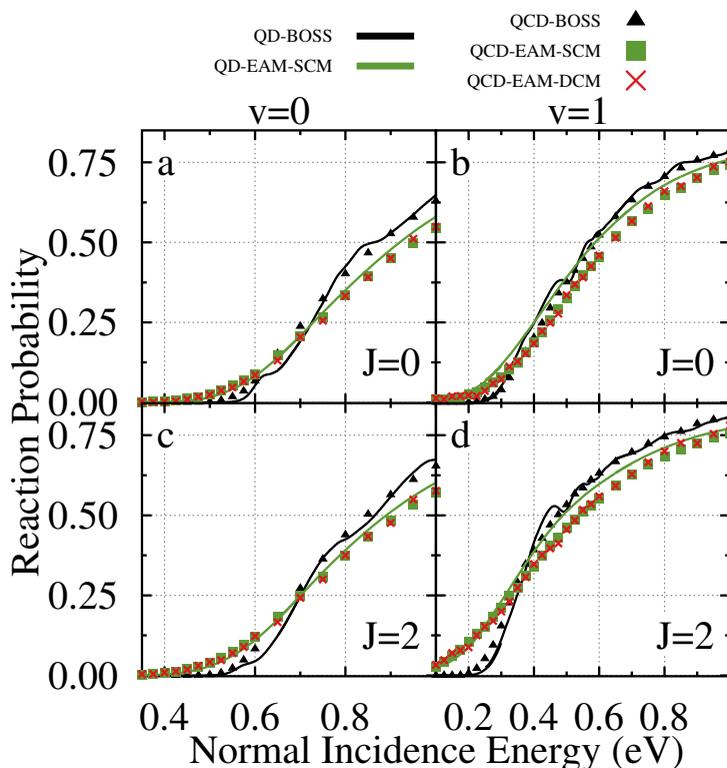
FIGURE 5.1:   Reaction probabilities obtained for four initial rovibrational states of
H_2 on Cu(111): (a) v = 0, J = 0; (b) v = 1, J = 0; (c) v = 0, J = 2; (d) v = 1, J = 2.
Included are the QD- and QCD-EAM-SCM results as a green curve and green squares
respectively, QCD-EAM-DCM results as red crosses, and QD- and QCD-BOSS results
as a black curve and black triangles respectively. A modeled surface temperature of
925 K was used for the SCM and DCM.

D_2 and Cu, but it once again confirms the validity of the sudden approximation for this system, and demonstrates the (lack of) effect of energy exchange for the dissociation reaction.

5.3.2 Binning methods explored

To achieve the best agreement between QCD and QD results, we also compare three (relatively simple) binning methods to obtain the final rovibrational state of our QCD simulations. This is especially valuable not just for this work, but also for future studies. Finding which QCD binning method compares best compared to rigorous QD simulations will be very important when comparing rovibrationally (in)elastic scattering probabilities. We show the effects of these binning methods on the final dissociation probabilities we compute in Figure 5.2., again for panels (a) the rovibrational ground state, (b) a vibrationally excited state, (c) a rotationally excited state, (d) and a rovibrationally excited state. As only the weighted binning will have an effect on the final reaction probabilities compared to the standard and floor binning, we have not included the floor binning in this figure. We include binned QCD results obtained with both the BOSS and EAM-SCM PES, as well as QD results from those PESs as a comparison.

We find the same trend for all four rovibrational states, with the standard binning method resulting in slightly higher reaction probabilities compared to the weighted binning. This effect is most noticeable for the $J = 0$ states, where the reaction is up to 3 percentpoint higher when using the standard binning method, which could be explained by the lack of lower energy rovibrational states to scatter into compared to the $J = 2$ states. In general, these slightly higher probabilities found using standard binning improves agreement with the QD results, both for BOSS and for EAM-SCM, although this effect is small enough that it will not significantly affect any conclusions made using either method.

The same cannot really be said when considering the rovibrationally elastic scattering curves for the three binning methods we have included. Figure 5.3 and 5.4 present these scattering probabilities for the vibrational ground and first excited state respectively, split for the standard [(a), (d), and (g)], weighted [(b), (e), and (h)], and floor [(c), (f), and (j)] binning methods. Again we take into account the rotational ground state [(a)-(c)]; $J = 0$, but now two additional excited states: [(d)-(f)] $J = 1$, and [(g)-(j)] $J = 2$. Next to the binned QCD-EAM-SCM and QCD-BOSS results, we also included the binned QCD-EAM-DCM results. QD-BOSS and -EAM-SCM results are again included as a comparison.

5
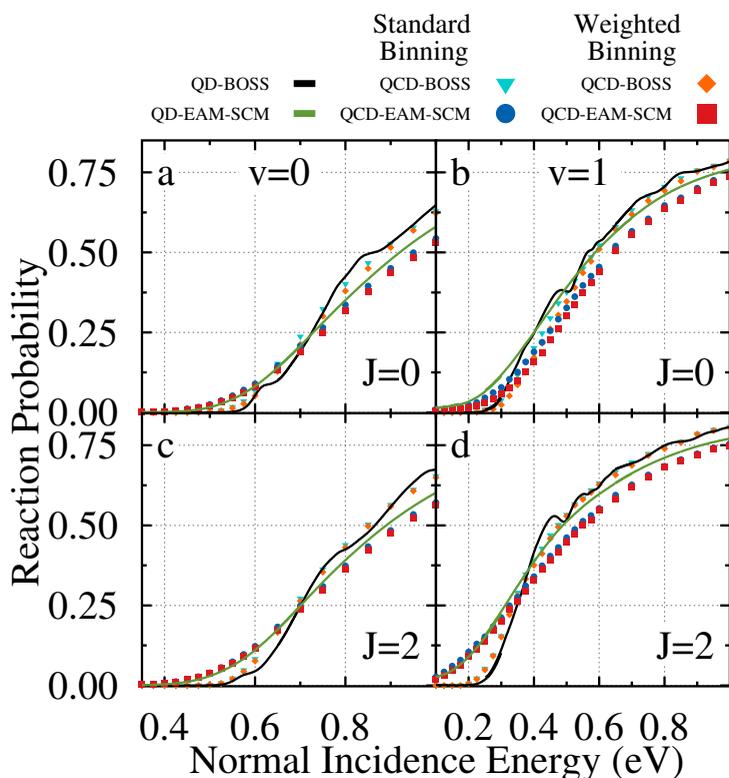
FIGURE 5.2:   Reaction probabilities obtained for four initial rovibrational states of H_2 on Cu(111): (a) $v = 0$, $J = 0$; (b) $v = 1$, $J = 0$; (c) $v = 0$, $J = 2$; (d) $v = 1$, $J = 2$. The QD results for the BOSS and EAM-SCM results are shown as black and green curves respectively, while the QCD-BOSS results are displayed as cyan triangles for the standard binning and orange diamonds for weighted binning. The QCD-EAM-SCM results show as blue circles for standard binning, and red squares for weighted binning.
    A modeled surface temperature of 925 K was used for the SCM and DCM.
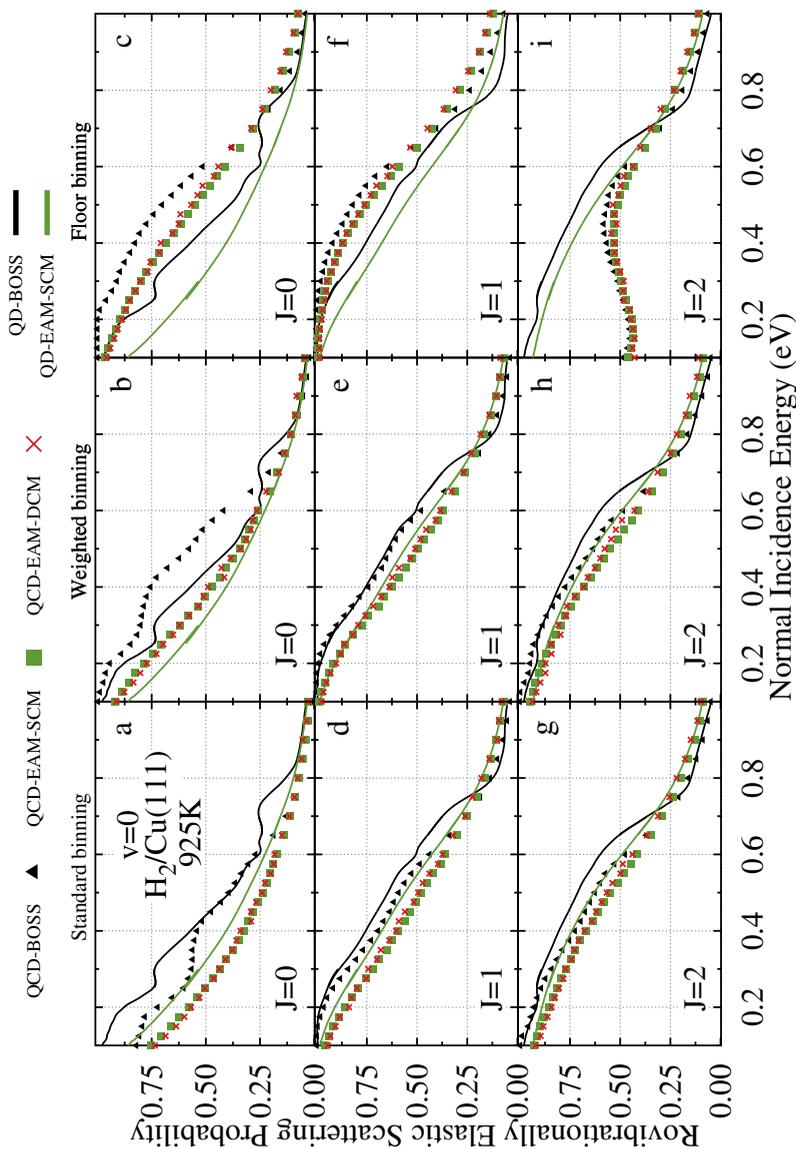
FIGURE 5.3: Rovibrationally elastic scattering probabilities of H_2 on a Cu(111) surface, obtained for the vibrational ground state ($v = 0$), and three rotational states: [(a)-(c)] $J = 0$; [(d)-(f)] $J = 1$; and [(g)-(i)] $J = 2$. Results are shown for the [(a), (d), and (g)] standard, [(b), (e), and (h)] weighted, and [(c), (f), and (i)] floor binning methods. Included are QD- and QCD- EAM-SCM results as a green curve and green squares respectively, QD- and QCD-BOSS results as a black curve and black triangles respectively, and finally the QCD-EAM-DCM results as red crosses. A modeled surface temperature of 925 K was used for the SCM and DCM.
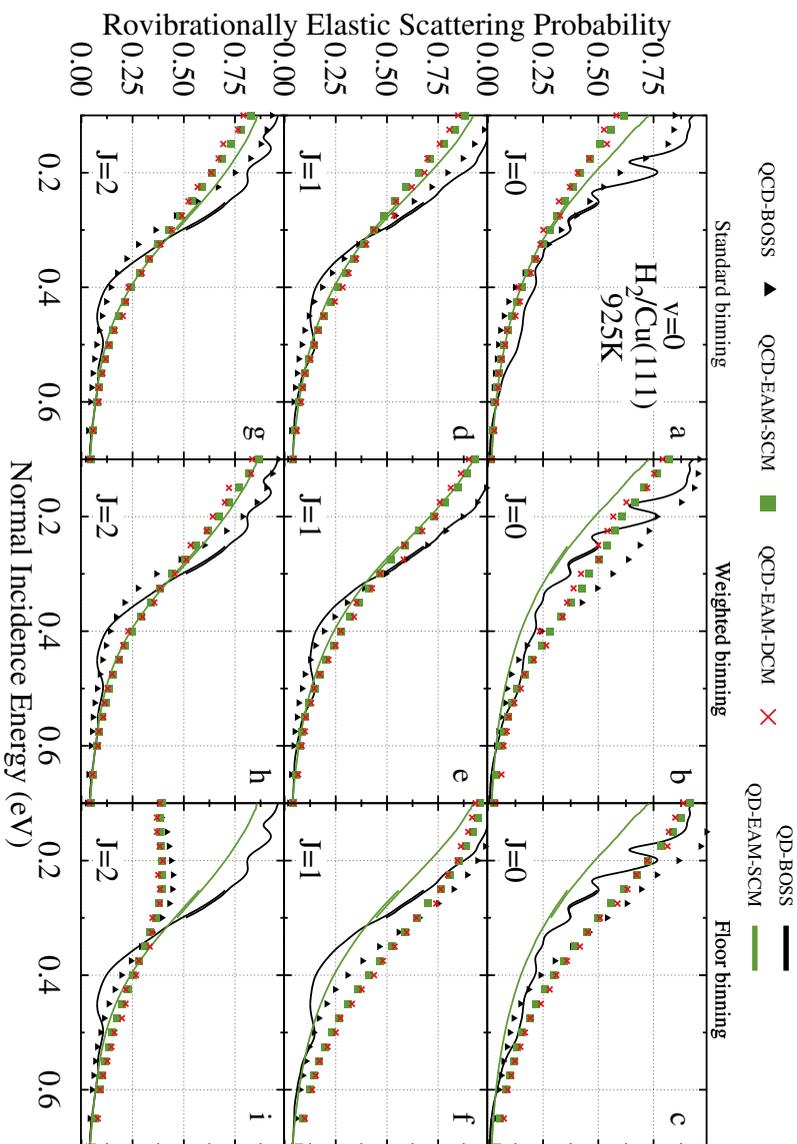
FIGURE 5.4: Rovibrationally elastic scattering probabilities of H_2 on a Cu(111) surface, obtained for the first vibrationally excited state (v = 1), and three rotational states: [(a)-(c)] J = 0; [(d)-(f)] J = 1; and [(g)-(i)] J = 2. Results are shown for the binning methods. Included are QD- and QCD- [(a), (d), and (g)] standard, [(b), (e), and (h)] weighted, and [(c), (f), and (i)] floor EAM-SCM results as a green curve and green squares respectively, QD- and QCD-BOSS results as a black curve and black triangles respectively, and finally the QCD-EAM-DCM results as red crosses. A modeled surface temperature of 925 K was used for the SCM and DCM.

As noted before, the agreement between the QCD-EAM-DCM and QCD-EAM-SCM results is again excellent regardless of the binning method chosen. This matches the findings of earlier work for D_2 on Cu(111), and further shows its independence of the binning method used.

The floor binning method heavily overestimates the elastic scattering probabilities at lower incidence energies compared to the QD results, or underestimates when the initial state is not the lowest allowed rotational state available. Interestingly, this also applies for the vibrationally excited states, suggesting that there is little conversion of vibrational to rotational energy, at least at the QCD level. At high incidence energies the agreement with the QD results does appear to be relatively good, although we do not think this binning method is in general a good choice for comparisons to QD results.

We find that the standard binning method generally predicts lower scattering probabilities compared to the weighted binning, which can be partially explained by the slightly higher reaction probabilities found for standard binning. Furthermore, those trajectories that are found with a "classical rotational state" slightly above the first rotational state of the incoming molecule ($\Delta J = +1$) are often binned "upward" to the first allowed state when using standard binning, while these states are completely disregarded for weighted binning. This effect would results in higher probabilities for the lower rotational states when dealing with lower incidence energies, as their energy would not be high enough to "push" the scattered molecules all the way to the next allowed state. We expect this effect to be especially strong for those states where the lowest allowed rotational state is also the initial state, in our results $J = 0$ and $J = 1$, and to be much more important for the scattering results, compared to the dissociation probabilities. However, it appears to be clearly noticeable only for the rovibrational ground state, where there is no vibrational energy to convert to higher rotational states, and to be somewhat important for the $v = 1$, $J = 0$ state. Neither of the $J = 1$ states show any significant difference that we can ascribe to this binning effect.

In general, the QCD binning method that leads to the best agreement with the QD results appears to heavily depend on the initial rovibrational state of the H_2. The standard binning performs somewhat better than the weighted binning for the $v = 0$ states and the $v = 1$, $J = 0$ state, while the weighted binning method performs a bit better for the $v = 1$, $J = 1, 2$ states, although not by much. The standard binning method underestimates the elastic scattering probabilities for the $v = 1$ states primarily at the lower incidence energies, where reaction is also lower. The weighted binning instead overestimates the $v=1$, $J=0$ probabilities much more over the entire energy range, but shows almost perfect agreement for the rotationally excited states.

For further comparisons to experimental work, the QCD results we present will be obtained using the standard binning method, as it is the method used in our previous studies. However, future work could focus on applying more complicated Gaussian binning methods, which have shown to improve agreement with QD results when properly used[38, 39].

5.3.3   Comparisons to experiment

Having chosen a binning method that yields QCD results that accurately reproduce our QD curves, we next aim to further validate the (QD-)EAM-SCM approach by comparing our reaction probability curves to those obtained in experimental studies. The three studies we compare to - published by Rettner *et al.*[7], Hodgson *et al.*[8] and Kaufmann *et al.*[11] - all obtained their results from desorption experiments, from direct inversion of their ToF results under the assumption of detailed balance.

As we discuss in section 5.2.3, this allows these studies to fit absolute values of the width parameter (W) and the inflection point (E_0) as described in equation 5.3. However, only relative saturation values (A) can be obtained from these experiments. Several approaches were suggested to obtain saturation values that allow for an accurate comparison to our theoretical results.

First, both Rettner *et al.* and Kaufmann *et al.* have performed beam adsorption experiments on their surfaces, which would yield accurate absolute saturation values of $A^{Rett} = 0.25$ eV and $A^{Kauf} = 0.35$ eV respectively. However, due to differences in experimental conditions it is unclear if this can directly apply[11]. Primarily the much lower surface temperature of 120 K (vs 925 K here), the use of an incidence angle to vary the normal incidence energy of the molecular beam and the final rovibrational composition of this beam could all have an effect on the final results of the adsorption measurements when compared to the desorption experiments. Additional discussion on these differences can be found in Ref. [11]. Next, it is suggested to use the theoretical curves to estimate an appropriate saturation value, by setting the saturation value to be equal to the theoretical sticking probability at the incidence energy to which the experiment is sensitive[11]. This will generally yield values in the range 0.50–0.60 eV. Finally, Wijzenbroek and Somers also found very good agreement between the experimental results of Hodgson *et al.* and Rettner *et al.* when the saturation for the Hodgson results is chosen as two times that of the Rettner curve ($A^{Hodg} = 0.50$ eV)[20].

In Figure 5.5 we present these fitted experimental S-curves and compare them to our QD- and QCD-EAM-SCM results. We have again included the initial rovibrational states of $(v, J) = (0, 0), (0, 1), (0, 2), (1, 0), (1, 1)$, and $(1, 2)$
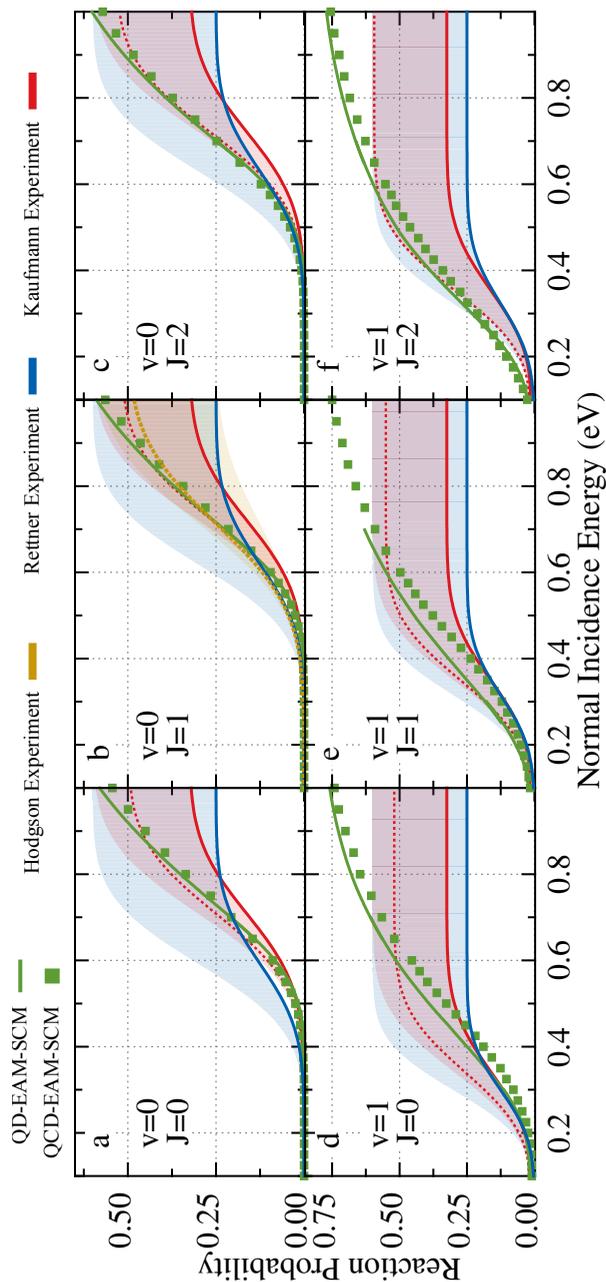
FIGURE 5.5: Reaction probabilities obtained for six initial rovibrational states of H_2 on Cu(111): (a) $v = 0$, $J = 0$; (b) $v = 0$, $J = 1$; (c) $v = 0$, $J = 2$; (d) $v = 1$, $J = 0$; (e) $v = 1$, $J = 1$; (f) $v = 1$, $J = 2$. Theoretical QD- and QCD-EAM-SCM results are shown as a green curve and green squares respectively. The experimental curves by Hodgson *et al.*[8], Rettner *et al.*[7] and Kaufmann *et al.*[11] are included in orange, blue and red respectively, with the uncertainty in the saturation value parameters of the experimental fits shown as shaded areas. Specific experimental curves are highlighted as: (solid red / solid blue) $A_0 = 0.5$ and 0.25 eV respectively from adsorption experiments; (dashed red) saturation parameter set equal to experimental QCD-EAM-SCM value at 0.95 eV; (dashed orange) estimated $A_0 = 0.25$ value based on agreement with Rettner experiment. A (modeled) surface temperature of 925 K was used for all these results.

for (a)-(f), respectively. The uncertainty in the saturation values are shown as shaded areas for each of the curves, choosing as a minimum the results from the beam adsorption experiments when available, or $A_{Min}^{Hodg} = 0.25$ for the curve where these data are not available. As a maximum a value of $A = 0.60$ eV is chosen, as no experimental works to our knowledge have reported values higher than this. Thus the shaded areas of each color reflect the range of A parameters [see (5.3)] each of the experimental curves could have, and visualises the uncertainty in the experimental absolute saturation values. Also included as solid lines are those curves where experimental beam adsorption results were used to obtain saturation values, when available for the experimental study, however these did not use exactly the same conditions as the desorption experiments that were fitted originally.

Finally, the estimated saturation values for the work by Hodgson *et al.*, based on the experimental work by Rettner *et al.*, and those estimated based on the theoretical sticking probabilities are included as dashed lines in orange and red respectively. The theoretically estimated saturation values of the Kaufmann experimental fit are set to be equal to our QCD-EAM-SCM results at the highest available energy of the experimental results, as has been done in previous studies[11, 21].

Comparing the experimental results to each other, keeping in mind especially the uncertainty in saturation values, we find good agreement. Only for the rovibrational ground state do we find some disagreement for the curve onset, which cannot be directly explained by this uncertainty. Interestingly, the experimentally obtained curves with saturation values predicted based on the desorption experiments (shown as solid lines in blue and red) show much better agreement for the vibrationally excited states compared to the vibrational ground state. Kaufmann *et al.* make a similar observation when directly comparing experimentally obtained E_0 and W parameters. They believe this disagreement to be primarily caused by errors in the calibration of the older works by Rettner *et al.*, which primarily affected accurate analysis of the faster (less rovibrationally excited) molecules[11].

We had already previously noted the generally good agreement between the QCD- and QCD-EAM-SCM results for some of these rovibrational states, although the differences for the vibrationally excited states is also clearly present for the v = 0, J = 1 state, with the QD results predicting a slightly higher dissociation probability across the entire energy range investigated.

Choosing the experimental saturation values based on the theoretical sticking values, in particular, leads to great agreement, as can be seen when comparing the red dashed line to our theoretical results in green for every state except v = 1, J = 0. For this state in particular we do see excellent overlap between

the QD-EAM-SCM results and the results presented by Kaufmann *et al.*, with a saturation value based on their beam adsorption experiments. Overall agreement between the theoretical work and the experimental work is good, with the theoretical results falling well within the range of experimental saturation values we expect.

5.3.4 Logscale results

To more carefully inspect the curve onset of our dissociation results, we have plotted them again on a logarithmic scale. In Figure 5.6. we again present our QD- and QCD-EAM-SCM, QD- and QCD-BOSS results, as well as the QCD-EAM-DCM results, where a moving surface is included. The rovibrational states are the same as presented in Figure 5.1., also using the same curves and symbols.

One of the first things that can be clearly noticed is the unexpected noise, or unexpected curvature, found in the QD results of both the BOSS and EAM-SCM results. As the reaction probabilities reach very low values, noise from our QD implementation starts becoming a much more important factor of the final results. This noise can clearly be seen in the unphysical behaviour in the BOSS curves, when considering the vibrational ground state (a) and (c) results at low incidence energies. One of the main contributions of this noise, we believe, is the error inherent to the SPO method in Eq. 6.1, which is inherent to the step-wise integration method of the SPO and scales with Δt^3. Thus smaller and smaller time steps are needed to accurately describe reaction probabilities ($P \approx 10^{-3}$), much lower than those we have used for our calculations (see 6.A). Reducing the time step by a factor 10 should reduce the expected noise due to the SPO propagation by as much as a factor of 10^3 while only increasing the computational load by a factor of 10. However, other factors and parameters of the WPs would also start to play a more dominant role in the final error that we observe. We consider the additional computational time needed to properly sample enough distorted surfaces for the SCM while also reducing this time step to be unfeasible for this study, although we believe it could be an important topic for later work.

Those results that we expect to be either partially, or perhaps fully, dominated by this noise we have included using a different curve color, with a lighter shade of either black for BOSS or green for the EAM-SCM results. However, an upturn of the reaction probability does seem to appear for very low incidence energies which is not visible at all for our QCD results. Recent work by Dutta *et al.* report a similar upturn for the D_2/Cu(111) system, investigated with the same SRP48 BOSS PES and QD implementation, but using the effective
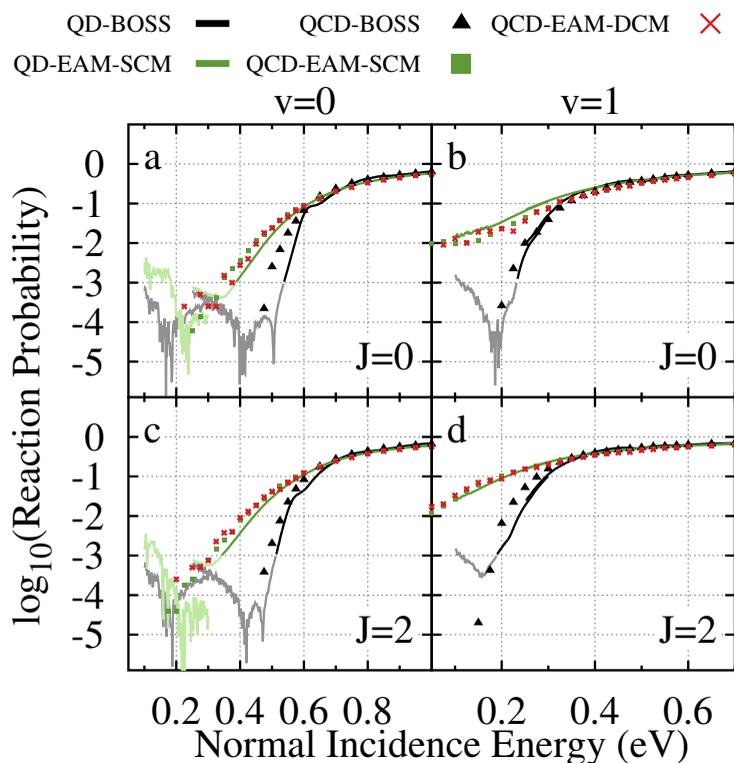
FIGURE 5.6: Reaction probabilities obtained for four initial rovibrational states of H_2 on Cu(111): (a) v = 0, J = 0; (b) v = 1, J = 0; (c) v = 0, J = 2; (d) v = 1, J = 2, with the reaction probabilities on a logarithmic scale. Theoretical QD- and QCD-EAM-SCM results are shown as a green curve and green squares respectively, and QD- and QCD-BOSS results as a black curve and black triangles, respectively. QD results where noise is expected to play a major role are shown as a lighter shade curve. QCD-EAM-DCM results are included as red crosses. A modeled surface temperature of 925 K was used for all the SCM and DCM results.

Hartree potential method, to include surface temperature effects[40]. They believe this could be attributed to the vibrational degrees of freedom, due to a modeled elevated surface temperature, which could match the slow channel as reported by Kaufmann *et al.*[11]. This EfHP work, however, uses the same SPO propagation method and is thus also expected to exhibit errors of a similar magnitude as our work, which is covered in both works. Furthermore, we also observe an upturn for the ideal lattice BOSS model, which suggests something more than purely attributing this to surface vibrational DoF. Thus, this would be a prime target for further studies, using more carefully crafted WPs and employing much smaller time steps in the SPO to investigate the very low incidence energy regions of our H_2 on the Cu(111) system, because at the moment we also do not yet have theoretical explanations of why such an upturn should be present in our BOSS results.

For the higher incidence energies, where the error in our QD results is expected to be small, we do still see great agreement with the QCD results, both for the BOSS and EAM-SCM results. The much more rapid drop in reactivity as the incidence energy decreases seen in the BOSS results, when compared to the EAM-SCM results, matches the observation of increased curve broadness when higher surface temperatures are taken into account[20, 21, 41]. For both PESs and every initial rovibrational state, the QCD calculations yield slightly higher reaction probabilities, except for the EAM-SCM results of the $v = 1$, $J = 0$ state, where this relation is inverted. This confirms again the quality of the EAM-SCM implementation at a QD level, and shows that we can accurately include the thermal surface effects into our QD simulations, even at lower energies. Furthermore, the EAM-DCM results almost perfectly match those of the EAM-SCM. This again shows the validity of a static surface approximation for our specific system, and the minimal effect energy exchange has for this dissociation reaction.

Finally, in Figure 5.7 we will compare the curve onset of our theoretical dissociation curves to those found in the experimental studies that we considered. The same states and results are presented as we had shown in Figure 5.5., but now we also included the QD- and QCD-BOSS results. Again we have used shaded areas to mark the uncertainty in the absolute experimental A values, which appears as a small static shift on the logarithmic scale. Furthermore, the contribution of the slow reaction channel reported by Kaufmann *et al.* now also becomes much more apparent at low incidence energies. Neither the work by Rettner *et al.* nor the work by Hodgson *et al.* reported observing this channel in their work.

Overlap between our QD- and QCD-EAM-SCM curves and the experimental results of Kaufmann *et al.* is, in general, excellent even for very low reaction
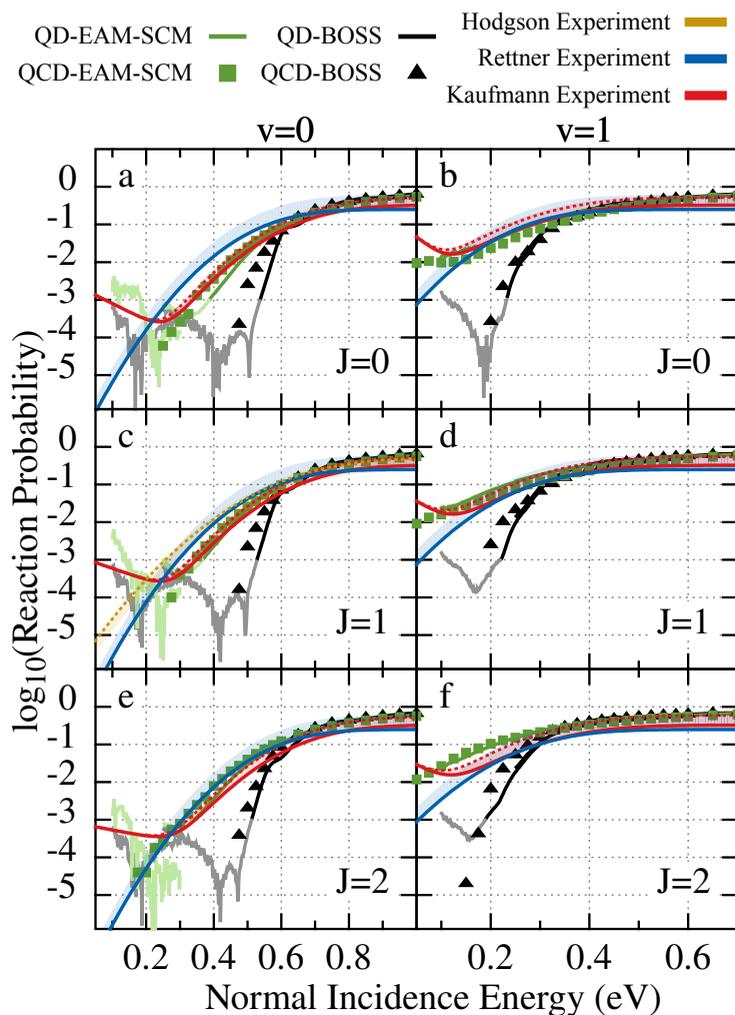
FIGURE 5.7:   Reaction probabilities obtained for six initial rovibrational states of H_2 on Cu(111): (a) v = 0, J = 0; (b) v = 1, J = 0; (c) v = 0, J = 1; (d) v = 1, J = 1; (e) v = 0, J = 2; (f) v = 1, J = 2, with the reaction probabilities on a logarithmic scale. Theoretical QD- and QCD-EAM-SCM results are shown as a green curve and green squares respectively, and QD- and QCD-BOSS results as a black curve and black triangles, respectively. QD results where noise is expected to play a major role are shown as a lighter shade. The experimental curves by Hodgson *et al.*[8], Rettner *et al.*[7] and Kaufmann *et al.*[11] are included in orange, blue and red respectively, with the uncertainty in the saturation value parameters of the experimental fits shown as shaded areas. Additional curves are shown the same as in Figure 5.5. A (modeled) surface temperature of 925 K was used for all these results.

probabilities. The biggest differences are found for the rovibrational ground state and the highest excited state that we included (v = 1, J = 2). However, a clear difference is found for the QCD-EAM-SCM results at very low incidence energies, as they do not predict any kind of slow channel. While the QD-EAM-SCM, and even the QD-BOSS, results do appear to predict an increase in reactivity at these very low energies, it is at the moment still unclear if this is an actual physical effect or an artifact introduced by our QD approach (or the CRP BOSS PES). Nevertheless, an upturn has been observed both in this study, and by Dutta *et al.* using a similar QD approach, but with a different method for including surface temperature effects, but also using the same BOSS PES and the same V_{coup} of the SCM to construct the effective time-dependent Hartree potential[40]. Again it should be emphasised that this work, as well as the work of Dutta *et al.*, is still as of yet inconclusive given the expected magnitude of errors in the QD simulations for these low probabilities. Fascinating though is the suggested presence of the apparent signal, even in our older BOSS calculations, and as of yet we lack an explanation for it (predominantly because of the errors in the approximations that we have to make in the QD). Thus, a more thorough theoretical investigation of this upturn, both with the SCM and the EfHP method, would be a very important topic for further studies. However, these computations will be computationally challenging, as reducing the time step by a factor of 10 will increase the computational costs by a factor of 10. Especially when also considering this for $T_s = 925$ K. One then has to perform these ten times more expensive calculations for at least 100 individual surface configurations, making such a study truly state-of-the-art and currently out of the scope for this paper.

5.4   Conclusion

We investigated the quality of the EAM-SCM approach, including all relevant surface temperature effects, at both a quantum dynamical and quasi-classical level, using the dissociative chemisorption of H_2 on Cu(111) (at a surface temperature of 925 K) as a model system. We computed both reaction and rovibrationally elastic scattering probabilities, and compared those to values obtained from the dynamic surface EAM-DCM and to H_2 sticking curves from experimental studies. We also investigated several simple binning methods, to validate the agreement between the QCD probabilities, and those obtained using rigorous quantum dynamics simulations. Our BOSS PES was constructed by Nattino *et al.*[29] using the CRP, with datapoints obtained from DFT using the SRP48 functional, while the SCM distorted surface corrections were described by the effective three-body SCM coupling potential as published by Spiering

et al.[25]. The thermally distorted surface configurations for the SCM were obtained from a highly accurate EAM potential using molecular dynamics, as described in Chapter 3.

While previous work had already shown that the QCD- and QD-EAM-SCM dissociation probabilities agreed well for the rovibrational ground state, we that demonstrated this also holds true for several initially rovibrationally excited states. The three different binnings methods that we investigated did not appear to significantly affect these probabilities, although weighted binning did slightly reduce the predicted QCD reaction probabilities, which reduced agreement with the QD curves.

Larger effects were found for the rovibrational elastic scattering, where either this weighted binning or our standard binning demonstrated better agreement with the curves obtained from QD simulations, for both the EAM-SCM and the BOSS approach. The final method of binning - floor binning - was found to greatly overestimate rovibrationally elastic scattering probabilities for the lower energy rovibrational states, but then greatly underestimated the same probabilities for those states that had more rovibrational energy available and had allowed scattering states with similar energies. As it only affected the determination of the final state of scattered molecules, the floor binning did not change the reaction probabilities compared to our standard binning method. Overall, we believe both the standard and weighted binning methods performed equally well, and as such could both be of interest for further studies.

Taking into account the uncertainty in absolute experimental saturation values, due to the nature of the direct inversion of desorption results used in the experimental method, we also found excellent agreement between our (QD-)EAM-SCM results and the experimental curves published by Rettner *et al.*[7], Hodgson *et al.*[8] and Kaufmann *et al.*[11]. Even for the curve onset, where reaction is best plotted on a logarithmic scale, we see good overlap with our theoretical results. At very low incidence energies, our QD results even indicate a small upturn in reaction similar to those found by Kaufmann *et al.*, also found by Dutta *et al.* using their EfHP method and the same QD code[40], but not been reported before in any other theoretical works. However, great care should be taken when interpreting our QD results in this regime, as the very low probabilities involved enables the noise inherent to the SPO method to become an important contribution to our final results. More carefully constructed wave packets, using a much smaller time step to minimise the error when propagating, would allow for a more thorough analysis of this slow channel using QD simulations.

In general, this work has shown that the EAM-SCM approach, which included surface temperature effects into quasi-classical and quantum dynamical

simulations works well for the H_2 on the Cu(111) system, at least at a surface temperature of 925 K. Comparisons to the dynamic surface EAM-DCM results further validate the sudden approximation made in the model, while comparisons to experimental results show that the model holds both for the rovibrational ground state, as well as several rovibrationally excited states. However, several other observables found in the literature, such as rotational/vibrational efficacies and rovibrationally inelastic scattering probabilities, have not yet been verified and thus are an interesting subject for further study. Equally, the noise introduced by the SPO method made it difficult to convincingly show that the slow channel of the H_2/Cu(111) system can be observed at a theoretical level using the EAM-SCM and thus would be an excellent target for further work, both using our SCM and the EfHP method by Dutta *et al.*

5

References

(1)   Chorkendorff, I., *Concepts of Modern Catalysis and Kinetics*; Wiley-VCH: Weinheim, 2003.

(2)   Smith, C.; Hill, A. K.; Torrente-Murciano, L. Current and future role of Haber–Bosch ammonia in a carbon-free energy landscape. *Energy & Environmental Science* **2020**, *13*, 331–344, DOI: 10.1039/C9EE02873K.

(3)   Campbell, C. T. The Degree of Rate Control: A Powerful Tool for Catalysis Research. *ACS Catalysis* **2017**, *7*, 2770–2779, DOI: 10.1021/acscatal.7b00115.

(4)   Kroes, G.-J. Computational approaches to dissociative chemisorption on metals: towards chemical accuracy. *Physical Chemistry Chemical Physics* **2021**, *23*, 8962–9048, DOI: 10.1039/D1CP00044F.

(5)   Berger, H. F.; Leisch, M.; Winkler, A.; Rendulic, K. D. A Search for Vibrational Contributions to the Activated Adsorption of H_2 on Copper. *Chemical Physics Letters* **1990**, *175*, 425–428, DOI: 10.1016/0009-2614(90)85558-T.

(6)   Michelsen, H. A.; Rettner, C. T.; Auerbach, D. J.; Zare, R. N. Effect of rotation on the translational and vibrational energy dependence of the dissociative adsorption of D_2 on Cu(111). *The Journal of Chemical Physics* **1993**, *98*, 8294–8307, DOI: 10.1063/1.464535.

(7)   Rettner, C. T.; Michelsen, H. A.; Auerbach, D. J. Quantum-state-specific dynamics of the dissociative adsorption and associative desorption of H_2 at a Cu(111) surface. *The Journal of Chemical Physics* **1995**, *102*, 4625–4641, DOI: 10.1063/1.469511.

(8)   Hodgson, A.; Samson, P.; Wight, A.; Cottrell, C. Rotational Excitation and Vibrational Relaxation of H_2 Scattered from Cu(111). *Physical Review Letters* **1997**, *78*, 963–966, DOI: 10.1103/PhysRevLett.78.963.

(9)   Hou, H.; Gulding, S. J.; Rettner, C. T.; Wodtke, A. M.; Auerbach, D. J. The Stereodynamics of a Gas-Surface Reaction. *Science* **1997**, *277*, 80–82, DOI: 10.1126/science.277.5322.80.

(10)   Murphy, M. J.; Hodgson, A. Adsorption and desorption dynamics of H_2 and D_2 on Cu(111): The role of surface temperature and evidence for corrugation of the dissociation barrier. *The Journal of Chemical Physics* **1998**, *108*, 4199–4211, DOI: 10.1063/1.475818.

(11) Kaufmann, S.; Shuai, Q.; Auerbach, D. J.; Schwarzer, D.; Wodtke, A. M. Associative desorption of hydrogen isotopologues from copper surfaces: Characterization of two reaction mechanisms. *The Journal of Chemical Physics* **2018**, *148*, 194703, DOI: 10.1063/1.5025666.

(12) Chadwick, H.; Somers, M. F.; Stewart, A. C.; Alkoby, Y.; Carter, T. J. D.; Butkovicova, D.; Alexandrowicz, G. Stopping Molecular Rotation Using Coherent Ultra-Low-Energy Magnetic Manipulations. *Nature Communications* **2022**, *13*, 2287, DOI: 10.1038/s41467-022-29830-3.

(13) Díaz, C.; Pijper, E.; Olsen, R. A.; Busnengo, H. F.; Auerbach, D. J.; Kroes, G. J. Chemically accurate simulation of a prototypical surface reaction: H_2 dissociation on Cu(111). *Science (New York, N.Y.)* **2009**, *326*, 832–834, DOI: 10.1126/science.1178722.

(14) Galparsoro, O.; Kaufmann, S.; Auerbach, D. J.; Kandratsenka, A.; Wodtke, A. M. First Principles Rates for Surface Chemistry Employing Exact Transition State Theory: Application to Recombinative Desorption of Hydrogen from Cu(111). *Physical Chemistry Chemical Physics* **2020**, *22*, 17532–17539, DOI: 10.1039/D0CP02858D.

(15) Smits, B.; Somers, M. F. Beyond the static corrugation model: Dynamic surfaces with the embedded atom method. *The Journal of Chemical Physics* **2021**, *154*, 074710, DOI: 10.1063/5.0036611.

(16) Smeets, E. W. F.; Kroes, G.-J. Designing New SRP Density Functionals Including Non-Local vdW-DF2 Correlation for H_2 + Cu(111) and Their Transferability to H_2 + Ag(111), Au(111) and Pt(111). *Physical Chemistry Chemical Physics* **2021**, *23*, 7875–7901, DOI: 10.1039/D0CP05173J.

(17) Smeets, E. W. F.; Kroes, G.-J. Performance of Made Simple Meta-GGA Functionals with rVV10 Nonlocal Correlation for H_2 + Cu(111), D_2 + Ag(111), H_2 + Au(111), and D_2 + Pt(111). *The Journal of Physical Chemistry C* **2021**, *125*, 8993–9010, DOI: 10.1021/acs.jpcc.0c11034.

(18) Smits, B.; Litjens, L. G. B.; Somers, M. F. Accurate Description of the Quantum Dynamical Surface Temperature Effects on the Dissociative Chemisorption of H_2 from Cu(111). *The Journal of Chemical Physics* **2022**, *156*, 214706, DOI: 10.1063/5.0094985.

(19) Díaz, C.; Olsen, R. A.; Auerbach, D. J.; Kroes, G. J. Six-Dimensional Dynamics Study of Reactive and Non Reactive Scattering of H_2 from Cu(111) Using a Chemically Accurate Potential Energy Surface. *Physical Chemistry Chemical Physics* **2010**, *12*, 6499–6519, DOI: 10.1039/C0019 56A.

5

(20)   Wijzenbroek, M.; Somers, M. F. Static surface temperature effects on the dissociation of H$_2$ and D$_2$ on Cu(111). *The Journal of Chemical Physics* **2012**, *137*, 054703, DOI: 10.1063/1.4738956.

(21)   Nattino, F.; Genova, A.; Guijt, M.; Muzas, A. S.; Díaz, C.; Auerbach, D. J.; Kroes, G.-J. Dissociation and recombination of D$_2$ on Cu(111): ab initio molecular dynamics calculations and improved analysis of desorption experiments. *The Journal of Chemical Physics* **2014**, *141*, 124705, DOI: 10.1063/1.4896058.

(22)   Bonfanti, M.; Somers, M. F.; Díaz, C.; Busnengo, H. F.; Kroes, G.-J. 7D Quantum Dynamics of H$_2$ Scattering from Cu(111): The Accuracy of the Phonon Sudden Approximation. *Zeitschrift für Physikalische Chemie* **2013**, 130617035227002, DOI: 10.1524/zpch.2013.0405.

(23)   Mondal, A.; Wijzenbroek, M.; Bonfanti, M.; Díaz, C.; Kroes, G.-J. Thermal Lattice Expansion Effect on Reactive Scattering of H$_2$ from Cu(111) at T$_s$ = 925 K. *The Journal of Physical Chemistry A* **2013**, *117*, 8770–8781, DOI: 10.1021/jp4042183.

(24)   Kroes, G.-J.; Juaristi, J. I.; Alducin, M. Vibrational Excitation of H$_2$ Scattering from Cu(111): Effects of Surface Temperature and of Allowing Energy Exchange with the Surface. *The Journal of Physical Chemistry C* **2017**, *121*, 13617–13633, DOI: 10.1021/acs.jpcc.7b01096.

(25)   Spiering, P.; Wijzenbroek, M.; Somers, M. F. An improved static corrugation model. *The Journal of Chemical Physics* **2018**, *149*, 234702, DOI: 10.1063/1.5058271.

(26)   Zhu, L.; Zhang, Y.; Zhang, L.; Zhou, X.; Jiang, B. Unified and transferable description of dynamics of H$_2$ dissociative adsorption on multiple copper surfaces *via* machine learning. *Physical Chemistry Chemical Physics* **2020**, *22*, 13958–13964, DOI: 10.1039/D0CP02291H.

(27)   Chadwick, H.; Alkoby, Y.; Cantin, J. T.; Lindebaum, D.; Godsi, O.; Maniv, T.; Alexandrowicz, G. Molecular spin echoes; multiple magnetic coherences in molecule surface scattering experiments. *Physical Chemistry Chemical Physics* **2021**, *23*, 7673–7681, DOI: 10.1039/D0CP05399F.

(28)   Busnengo, H. F.; Salin, A.; Dong, W. Representation of the 6D potential energy surface for a diatomic molecule near a solid surface. *The Journal of Chemical Physics* **2000**, *112*, 7641–7651, DOI: 10.1063/1.481377.

(29) Nattino, F.; Díaz, C.; Jackson, B.; Kroes, G.-J. Effect of Surface Motion on the Rotational Quadrupole Alignment Parameter of D_2 Reacting on Cu(111). *Physical Review Letters* **2012**, *108*, 236104, DOI: 10.1103/PhysRevLett.108.236104.

(30) Kroes, G.-J.; Díaz, C. Quantum and classical dynamics of reactive scattering of H_2 from metal surfaces. *Chemical Society Reviews* **2016**, *45*, 3658–3700, DOI: 10.1039/c5cs00336a.

(31) Sheng, H. W.; Kramer, M. J.; Cadien, A.; Fujita, T.; Chen, M. W. Highly optimized embedded-atom-method potentials for fourteen fcc metals. *Physical Review B* **2011**, *83*, 134118, DOI: 10.1103/PhysRevB.83.134118.

(32) Spiering, P.; Meyer, J. Testing Electronic Friction Models: Vibrational De-excitation in Scattering of H_2 and D_2 from Cu(111). *The Journal of Physical Chemistry Letters* **2018**, *9*, 1803–1808, DOI: 10.1021/acs.jpclett.7b03182.

(33) Sementa, L.; Wijzenbroek, M.; van Kolck, B. J.; Somers, M. F.; Al-Halabi, A.; Busnengo, H. F.; Olsen, R. A.; Kroes, G. J.; Rutkowski, M.; Thewes, C.; Kleimeier, N. F.; Zacharias, H. Reactive scattering of H_2 from Cu(100): Comparison of dynamics calculations based on the specific reaction parameter approach to density functional theory with experiment. *The Journal of Chemical Physics* **2013**, *138*, 044708, DOI: 10.1063/1.4776224.

(34) Smeets, E. W. F.; Füchsel, G.; Kroes, G.-J. Quantum Dynamics of Dissociative Chemisorption of H_2 on the Stepped Cu(211) Surface. *The Journal of Physical Chemistry C* **2019**, *123*, 23049–23063, DOI: 10.1021/acs.jpcc.9b06539.

(35) Füchsel, G.; Klamroth, T.; Monturet, S.; Saalfrank, P. Dissipative Dynamics within the Electronic Friction Approach: The Femtosecond Laser Desorption of H_2/D_2 from Ru(0001). *Physical Chemistry Chemical Physics* **2011**, *13*, 8659, DOI: 10.1039/c0cp02086a.

(36) Maurer, R. J.; Jiang, B.; Guo, H.; Tully, J. C. Mode Specific Electronic Friction in Dissociative Chemisorption on Metal Surfaces: H_2 on Ag(111). *Physical Review Letters* **2017**, *118*, 256001, DOI: 10.1103/PhysRevLett.118.256001.

(37) Spiering, P.; Shakouri, K.; Behler, J.; Kroes, G.-J.; Meyer, J. Orbital-Dependent Electronic Friction Significantly Affects the Description of Reactive Scattering of N_2 from Ru(0001). *The Journal of Physical Chemistry Letters* **2019**, *10*, 2957–2962, DOI: 10.1021/acs.jpclett.9b00523.

5

(38) Rodríguez-Fernández, A.; Bonnet, L.; Crespos, C.; Larrégaray, P.; Díez Muiño, R. When Classical Trajectories Get to Quantum Accuracy: The Scattering of H₂ on Pd(111). *The Journal of Physical Chemistry Letters* **2019**, *10*, 7629–7635, DOI: 10.1021/acs.jpclett.9b02742.

(39) Rodríguez-Fernández, A.; Bonnet, L.; Crespos, C.; Larrégaray, P.; Díez Muiño, R. When Classical Trajectories Get to Quantum Accuracy: II. The Scattering of Rotationally Excited H₂ on Pd(111). *Physical Chemistry Chemical Physics* **2020**, *22*, 22805–22814, DOI: 10.1039/D0CP02655G.

(40) Dutta, J.; Naskar, K.; Adhikari, S.; Spiering, P.; Meyer, J.; Somers, M. F. Effect of surface temperature on quantum dynamics of D₂ on Cu(111) using a chemically accurate potential energy surface, To Be Submitted, 2022, submitted.

(41) *Dynamics of Gas-Surface Interactions: Atomic-level Understanding of Scattering Processes at Surfaces*; Muino, R. D., Busnengo, H. F., Eds.; Springer Series in Surface Sciences; Springer-Verlag: Berlin Heidelberg, 2013, DOI: 10.1007/978-3-642-32955-5.

The quantum dynamics of H_2 on Cu(111) at a surface temperature of 925 K: Comparing theory to experiments 2

Abstract

State-of-the-art 6D quantum dynamics simulations for the dissociative chemisorption of H_2 on a thermally distorted Cu(111) surface, using the static corrugation model, were analysed to produce several (experimentally available) observables. The expected error, especially important for lower reaction probabilities, was quantified using wavepackets on several different grids as well as two different analysis approaches. This allowed for more accurate results in the region where a slow reaction channel was experimentally shown to be dominant. The lowest reaction barrier sites for different thermally distorted surface slabs are shown to not just be energetically, but also geometrically, different between surface configurations. This can be used to explain several dynamical effects found when including surface temperature effects. Direct comparison of simulated time-of-flight spectra to those obtained from state-of-the-art desorption experiments showed much improved agreement compared to

the perfect lattice BOSS approach. Agreement with experimental rotational and vibrational efficacies also somewhat improved when thermally excited surfaces were included in the theoretical model. Finally, we present clear quantum effects in the rotational quadrupole alignment parameters found for the lower rotationally excited states, which underlines the importance of careful quantum dynamical analysis of this system.

6.1　Introduction

The dissociative chemisorption of hydrogen on a Cu(111) surface has, over the years, become a model system for the field of hetergeneous gas-surface catalysis, with a wide array of available experimental[1–8] and theoretical[9–24] data. In these studies the focus is on describing the elementary reaction step of the dissociation of a small molecule on a (metal) surface. These reaction steps are considered the chemically rate-limiting step in many industrial processes such as the Haber-Bosch process[25] (N_2 on Fe) or methane steam reforming[26] (CH_4 on Ni). However one of the aspects not always well described by previous studies is the effects the thermal distortion of and energy exchange with the surface have on these dissociation reactions[27, 28].

In the previous chapters, we have demonstrated that the static corrugation model (SCM) is able to accurately include all the relevant surface temperature effects for the H_2/Cu(111) system using thermally distorted, but static, surface configurations. Over the years, several other models with varying ranges of computational costs and degrees of overall accuracy have also been proposed to include surface temperature effects. For CH_4 reacting on metal surfaces Busnengo *et al.* and Jackson *et al.* reported a wide range of methods to include surface temperature effects, including sudden approximations, moving surfaces and phonon bath approaches[29–35]. Other approaches include the use of a static disorder parameter by Manson and co-workers[36], the effective Hartree potential method by Dutta *et al.*[37, 38], as well as the more general ring polymer molecular dynamics[39, 40] and high-dimensional neural network potential approaches[10, 41–43]. However, to our knowledge, the SCM is the first to have been applied in rigorous 6D quantum dynamics simulations, as introduced in Chapters 4 and 5. Nevertheless, reduced dimensionality studies have been performed in the past[44].

The SCM relies on a sudden approximation to describe the surface temperature effects of the H_2 dissociation reaction. It was designed to modify 6D perfect lattice potential energy surfaces (PESs) with an additional term that describes the change in potential energy of the surface due to thermally distorted configurations. The previous chapters have already shown that such

a static surface treatment reproduces both experiment and moving surface (quasi-)classical dynamics well, which has also been observed for methane[30]. Furthermore, the relative simplicity of the expressions used in the SCM also allow it to be used for full 6D quantum simulations of the H_2 dissociation reaction. Here we Monte-Carlo sample different (thermally distorted) surface configurations to treat the surface degrees of freedom at a quantum dynamical sudden approximation level, which has been shown to agree very well with (quasi-)classical approaches[45]. In doing so, the associated computational cost of directly adding additional surface degrees of freedom can successfully be avoided, and the possibility arises to perform (still challenging) accurate diffractive scattering calculations at low surface temperatures. These calculations can then, in the future, be directly compared to many experiments, such as the recent state-of-the-art experiments published by Chadwick *et al.* obtained using their molecular interferometry setup[8, 46]. Currently the SCM combined with surface configurations from molecular dynamics has only been used for surface temperatures of 925 K, well within the classical limit (Debye temperature) where standard molecular dynamics can be used. For low surface temperatures relevant to diffraction experiments (120 K or lower), another approach will be needed to generate the correct surface configurations adhering to Bose-Einstein statistics while avoiding the possibility of zero-point energy leaking due to the thermostat used.

Although the SCM has so far only been applied to the H_2 on Cu(111) system, its approach is expected to be general enough to be applied to other (diatomic) molecules reacting on transition metal surfaces. It is expected to perform especially well for those systems where the sudden approximation holds, i.e., where a relatively large mass mismatch between reactant and surface and short interaction times with the surface minimise energy exchange. While the effective three-body expression for the SCM coupling potential will work for any diatomic molecule interacting with a surface, new expressions would be required as the number of atoms are increased. This would be an interesting topic for future research, but is out of the scope of this thesis. The availability of a data set from for example density functional theory (DFT) calculations, which can be used to fit both the perfect lattice PES as well as the SCM coupling potential, would further reduce the workload needed to apply the SCM to other systems. Thermally distorted surface configurations can be obtained for cases well within the classical limit using a variety of force-field methods, such as the embedded atom method that we employ for this thesis. These surface configurations can also be approximated using, for example, the Debye-Waller factor as was done in the earlier SCM studies[19, 24].

Chapter 5 demonstrated that the SCM reproduces experimental dissociation

probabilities well for the lower energy ranges at both the quantum and the quasi-classical level. Nevertheless, it also shows that direct comparisons to experimentally fitted dissociation curves is difficult across the entire energy range, due to the uncertainties in the available experimental data[16]. Therefore this chapter will focus on several observables which can be derived from earlier results, supplemented with some additional calculations where needed. We will discuss the effect of the time step on our QD simulations, especially at very low reaction probabilities, and the accuracy that is expected from the methods employed. These results can then be used to investigate the presence or absence of an experimentally observed slow reaction channel in more depth, which was previously left an open question due to the compromise between accuracy and computational cost that had been made. We present several 2D cuts of the PES for different thermally distorted surfaces, and show how the thermal displacement of surface atoms changes not only the lowest barrier heights, but also their geometry on the 2D cut. Next we discuss several fits to the dissociation probability curves that were obtained, comparing fit parameters to those obtained from the experiments. We also use these fits to obtain simulated time-of-flight spectra, which should allow for a more direct comparison of experimental associative desorption results. Finally, we present results on the effect of the internal energies of the H_2 on the dissociation reaction, using both rotational and vibrational efficacies and the rotational quadrupole alignment parameter. Overall, we hope the results presented here will provide a solid data set for future comparative experimental and theoretical work.

6.2 Methods

Previous chapters focused on dissociation and (rovibrationally elastic) scattering probabilities obtained using either the EAM-SCM or the BOSS PESs, both at a QD and a QCD level. Here we will instead compare other variables and/or observables that can be obtained from these probability curves. Thus the results presented in this chapter will be almost directly based on those presented in Chapters 4 and 5, with some additional data added where needed.

6.2.1 Quantum dynamics

We expand on the available QD results of the previous chapters by adding a WP in the 0.95-1.50 eV energy range for the results in the initial vibrational ground state. Also included is the WP in the 0.65-1.00 eV range for the v=1, J=1 states. For the initially rotationally excited states, only those states with $m_J \geq 0$ were considered, with the results for $m_J \neq 0$ counted twice in the total

average per rotational (J) state. This double counting accounts for the $m_J < 0$ states (as R_{v,J,m_J} should equal $R_{v,J,-m_J}$).

We propagate our WPs using the split operator (SPO) method,

$$\Psi(\overrightarrow{Q};t_0 + \Delta t) = \quad \exp(-\frac{i}{2}K\Delta t) \cdot \exp(-iV(\overrightarrow{Q})\Delta t) \quad (6.1)$$
$$\exp(-\frac{i}{2}K\Delta t) \cdot \Psi(\overrightarrow{Q};t_0) + O[(\Delta t)^3],$$

with K being the kinetic energy part of our Hamiltonian, as implemented in our in-house code[45], and further discussed in section 2.1.3 of Chapter 2. Here the WPs are propagated in a stepwise fashion, first taking a half-step for the free particle propagation, then a full time step action of the potential is applied, followed by another half-step as a free particle. This stepwise propagation method inherently results in an error $O[(\Delta t)^3]$ that scales with the size of the time step used.

We use a quadratic form of the optical potentials in the scattering and reactive channel regions[47]. The scattered fraction is analyzed through the scattering matrix formalism[48], which yields the scattering probabilities for each rovibrational state and diffraction channel separately. The sticking probability is subsequently calculated by subtracting the sum of all these scattering probabilities from one. For some simulations, these sticking probabilities are also compared to those obtained from a flux analysis in r[49, 50]. This approach directly measures the flux through a plane for a specific large enough value of r, but does not yield any information on the scattered states. For a more in-depth discussion of the basis of these quantum mechanical methods, we direct the reader to section 2.1 of Chapter 2.

Only those thermally distorted surface atoms in the top two layers of the surface slab, and within the SCM cutoff distance of 16 bohrs (~ 8.47 Å) of the 1×1 unit cell corner, are included in the SCM, as this is where the coupling potential is available[24]. To obtain a single representative dissociation curve for H_2 reacting with thermally distorted Cu(111) at a QD level, we average the probabilities obtained for a total of 104 unique thermally distorted surface slabs. Chapter 4 showed 104 surfaces was enough to reproduce the results of including the full dataset of 25000 surface configurations with only a small error.

6.2.2 Rotational quadrupole alignment parameter

The rotational quadrupole alignment parameter $[A_0^{(2)}(J)]$ is a measure of preference for the H_2 to dissociate in particular m_J states. When it is positive,

dissociating molecules prefer to react rotating parallel to the surface ($|m_J| =$ J; "helicopter"), while negative values indicate a preference for reaction of molecules with a rotation perpendicular to the surface ($|m_J| = 0$; "cartwheel"). A value of zero indicates no preference for either.

The rotational quadrupole alignment parameter (RQAP) is defined as

$$A_0^{(2)} \equiv \langle 3\cos^2\theta_L - 1\rangle \tag{6.2}$$

with θ_L the angle between the angular momentum vector and the surface normal. The RQAP can also be computed through

$$A_0^{(2)}(J;v) = \frac{\sum_{m_J} P_{stick}(v, J, m_J)\left(\frac{3m_J^2}{J(J+1)} - 1\right)}{\sum_{m_J} P_{stick}(v, J, m_J)}, \tag{6.3}$$

with $P_{stick}(v, J, m_J)$ the sticking probabilities for the specific rovibrational state. Assuming using associative desorption detailed balance the RQAP can also be measured experimentally, although there are no studies available for the H$_2$ on Cu(111) system to our knowledge. However, some data for D$_2$ is available[5, 51, 52].

6.2.3   Simulating time-of-flight spectra

To more directly compare to the time-of-flight (ToF) spectra obtained from the state-selective desorption experiments, we can also directly simulate ToF spectra from our dissociation curves, as described in section 2.4.2 of Chapter 2. In short, the experimental approach of Ref. [2] is mirrored, making use of direct inversion under the assumption of detailed balance to directly relate the dissociative adsorption results to the ToF spectra obtained from associative desorption. The intensity of the ToF spectrum is related to the sticking probability function multiplied by a flux-weighted velocity distribution expressed in the time domain,

$$I(t')dt' = K \cdot C(t') \cdot \exp\left(\frac{-E_{kin}[t']}{2k_bT_s}\right)\left(\frac{x_0}{t'}\right)^4 \cdot P_{stick}(E_{kin}[t'])\, dt' \tag{6.4}$$

with k_b the Boltzmann constant, T_s the surface temperature, K a proportionality constant, $E_{kin} = m\left(\frac{x_0}{t'}\right)^2$, and $t' = t - t_{shift}$. t and t_{shift} describe the travel time in and after leaving the field-free region, respectively, and x_0 describes the length of this field-free region in the detector of the experimental setup that is being simulated.

The cutoff function we used was of an exponential form

$$C(E_{kin}) = 1 - e^{-E_{slope}(E_{kin}-E_{min})} \text{ for } E_{kin} > E_{min},$$ (6.5)

based on the kinetic energy of the molecule, as was obtained in the experimental study[7]. The cutoff parameters E_{slope}, which governs how fast the signal decays, and E_{min}, which determines the minimal energy the molecule needed to be experimentally detectable, were obtained from the same experimental study.

The dissociation curves were fitted to the error function (ERF), Gompertz function (GMP), and the five-parameter function (FPC) forms to obtain a continuous representation of $[P_{stick}(E_n)]$. These continuous representations are required to accurately apply (6.4) over the entire time range. Both the QD and QCD results were fitted to these functional forms using a Levenberg-Marquardt routine, minimising the residual difference between the available data-points and the model. For those QD results where there is overlap between the different WPs at the same energy, the WP reaching up to higher energy was always chosen to prevent double counting during the fitting procedure. Using the lower energy WP, however, should work equally well.

6.2.4 Threshold offset and efficacies

Using the state-selective results, rotational and vibrational efficacies can also be obtained. These in particular indicate the ability of the rotational and the vibrational energy of H_2 to promote reaction with the surface, which is an often available from experiments. In this chapter the method by Shuai *et al.* is used[53], which relies on first finding the energy offset between the rotational or vibrational ground state and each specific curve. This approach also gives another observable, in the form of the threshold offset itself, to compare to, as described in section 2.4.3 of Chapter 2.

For this chapter, the difference between the logarithms of the two reaction curves was also minimised to obtain the threshold offset, similar to the procedure in Ref. [7]. Although using the logarithm of the results should put a focus on the curve onset of the dissociation curves, it did not appear to change the final results significantly.

6.3 Results and Discussion

6.3.1 Effect of QD time step

In Chapter 5, we discuss an unphysical "upturn" present for the QD results at very low reaction and energy, which appears within the same range as the

140

Chapter 6. The quantum dynamics of H_2 on Cu(111) at a surface temperature of 925 K: Comparing theory to experiments 2

6
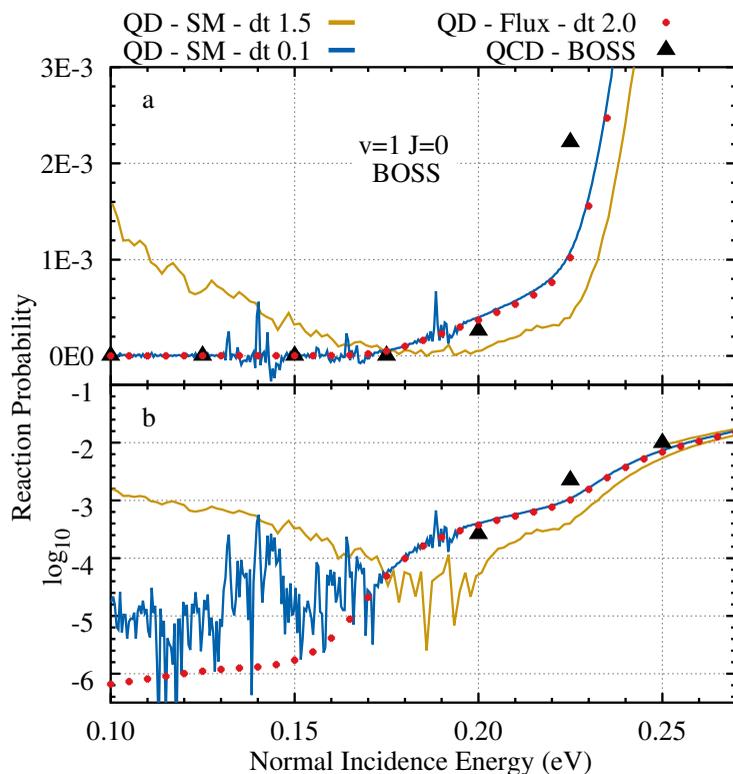
FIGURE 6.1: Dissociative chemisorption probabilities of H_2 on Cu(111) for the first vibrationally excited state, obtained using the BOSS approach and several different time steps. Included are: (orange) QD results for a time step of 1.5 au using the scattering amplitude formalism, (blue) QD results for a time step of 0.1 au using the scattering amplitude formalism, (red circles) QD results for a time step of 2.0 au using flux analysis method, and (black triangle) QCD results. Both a regular (a) and a logarithmic (b) scale are used for the reaction probabilities.

experimental "slow" channel fitted by Kaufmann *et al.*[7]. However, its shape led us to believe it was more likely to be noise due to the split-operator method (Eq. 2.31) being used with a too large time step, this method having an inherent error scaling with $O(\Delta t^3)$. Other parameters of the QD calculation, such the size of the specular and scattering grid, the distance of the analysis plane from the optical potential, and the parameters governing the optimal absorption of these optical potentials, were found to have little to no effect on the magnitude of this noise.

To verify the upturn found in the previous study and investigate the influence of the propagation time step, we now compare our previous results to new QD results obtained with a time step of 0.1 au (vs. 1.5 au for our original calculations), as is shown in Figure 6.1. Next to these small time step (blue) and larger time step (orange) curves, we also include the QCD-BOSS results in black and the results of the flux analysis method on the same system and a time step for propagation of 2.0 au.

Comparing the computed reaction probabilities on the regular [Fig. 6.1(a)] and the logarithmic [Fig. 6.1(b)] scale, we clearly see this "upturn" for the larger time step results obtained with the scattering amplitude formalism (SAF), resulting in an error in the range of 10^{-3}. In contrast, the flux analysis method appears to converge to much smaller probabilities in the 10^{-6} range, even with a larger time step for propagation. It should, however, be noted that this analysis method only yields reaction probabilities, and is thus not suitable to obtain rotationally and vibrationally (in)elastic scattering probabilities. Finally, by much reducing the time step, we are able to reduce our error in the results of the SAF to the range of 10^{-5}, as can be seen by the blue curve. Interestingly, this smaller time step also has some effect on the higher energy ranges just above the threshold for reaction, slightly reducing the reaction probabilities we find similarly to how they are increased at low energy. The good agreement between flux analysis and SAF results does appear to indicate we obtain accurate reaction probabilities to as low as $10^{-4.5}$ (around 0.17 eV of incidence energy), where the flux analysis and SAF results diverge.

Different noise-like peaks, most notable around 0.140, 0.165, and 0.190 eV, have also become more apparent for the QD results obtained with the smaller time step. These peaks are attributed to entrance channel resonances, i.e., trapping of the molecule due to an excitation of the molecular bond as it is weakened near the surface. Due to the use of the SAF this trapping results in a small increase in reaction probability, as has also been observed with much earlier implementations of this analysis method[54, 55]. While we do not expect these resonances to become much more important as the time step is decreased, we do expect the error they introduce to become more relevant as other sources

of noise are reduced. As the flux analysis method only analyses the reactive flux it is insensitive to this trapping.

Overall, these results once again underline the importance of carefully crafted wavepackets when using the SPO method, but also give us a range of error we can expect when further analysing the results for this, and previous, studies. Clearly, as in every computational study, one always needs to balance accuracy and computational cost as reducing the time step from 1.5 to 0.1 au makes every single WP calculation, of the 104 we need to perform per energy range when including the SCM, 15 times more expensive. Such a study would thus be more than 1500 times more expensive than a traditional 6D BOSS QD WP calculation, which nowadays takes roughly 24h on a modern 32 core CPU.

Although the balance between accuracy and computational speed of the SPO method is very favourable for most of the calculations we performed in this work, for these curve onsets (and perhaps for other systems in general) the method scales poorly for lower time steps. Therefore another approach could be to instead implement another propagation method, which might not perform as computationally efficient for higher reaction probabilities but does yield significantly lower propagation errors[56]. Comparisons between the different propagation methods when applied to our system would also allow for a clearer estimate of the error we find for the SPO propagation, regardless of the final analysis method used. Nonetheless, it is noted that for probabilities at the threshold and beyond, the usual accuracy of 10^{-3} using dt = 1.5 au is quite sufficient.

6.3.2   Barrier shape and location

Next we will first discuss several cuts of the PES and the location of the transition state found there, both for thermally distorted surfaces and the perfect crystal. These cuts will shed some light not only on the changes in lowest barrier heights brought about by including the SCM but also demonstrate how the location of the barrier can change as the surface atoms are shifted from their ideal lattice positions. These slabs were obtained from the dataset of surfaces generated in Chapter 3 through molecular dynamics at a surface temperature of 925 K, applying a highly accurate EAM potential[59]. In Fig. 6.2 and Fig. 6.3, we present a collection of two sets of contour plots (or elbow plots) of the PES at the (lowest barrier) bridge-to-hollow (bth), and the top-to-fcc (ttf) reaction sites, respectively. Generally, these lowest barrier sites will have major effects on the shape of the dissociation curves, as they provide a predictive tool for the onset of the reaction. In panels (b), (c), and (d) of Figs. 6.2 and 6.3, we show the potential for a specific less reactive, a very
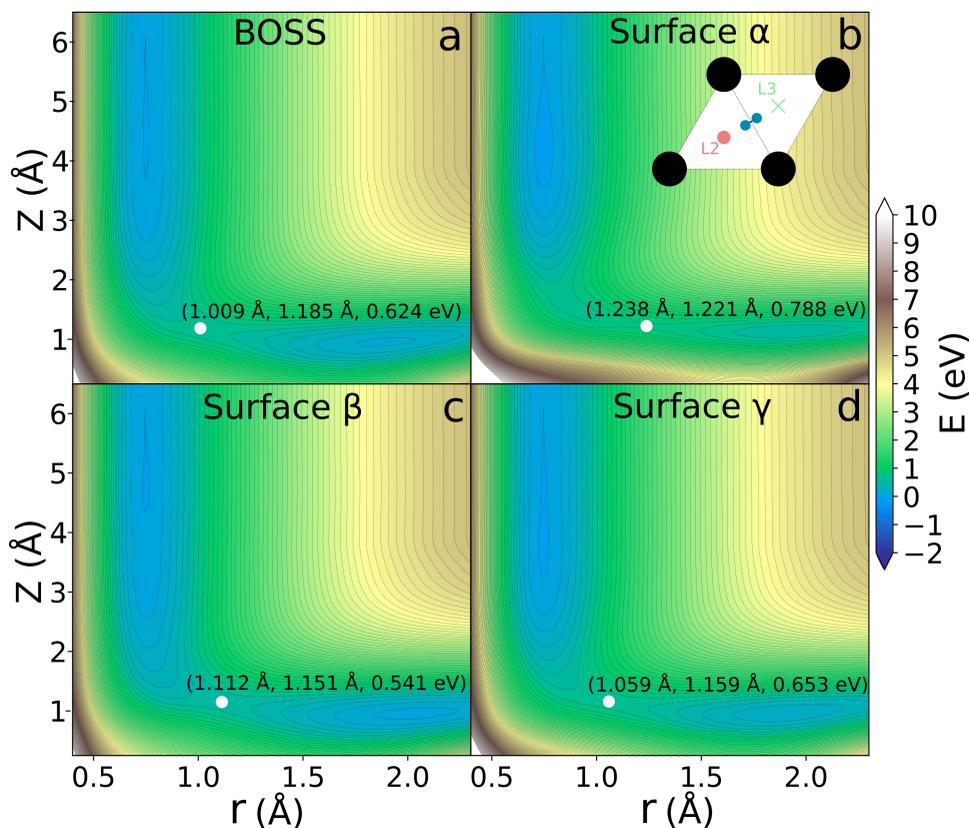
FIGURE 6.2: Potential energy contour plot for the bridge-to-hollow (bth) reaction site, as depicted in panel b. The PES was interpolated using the CRP[57] using DFT obtained with the SRP48 functional[22, 58]. Included are the potential for the (a) BOSS approach, as well as three different SCM distorted surfaces: (b) less reactive α, (c) very reactive β, and (d) typical reactivity γ, which have also been discussed in Chapter 4. The transition state for each 2D PES is marked with a white circle, including the location of the barrier in the (r, Z, V) format. The distorted surface slabs for the SCM, at a modelled surface temperature of 925 K, were obtained from Chapter 3.
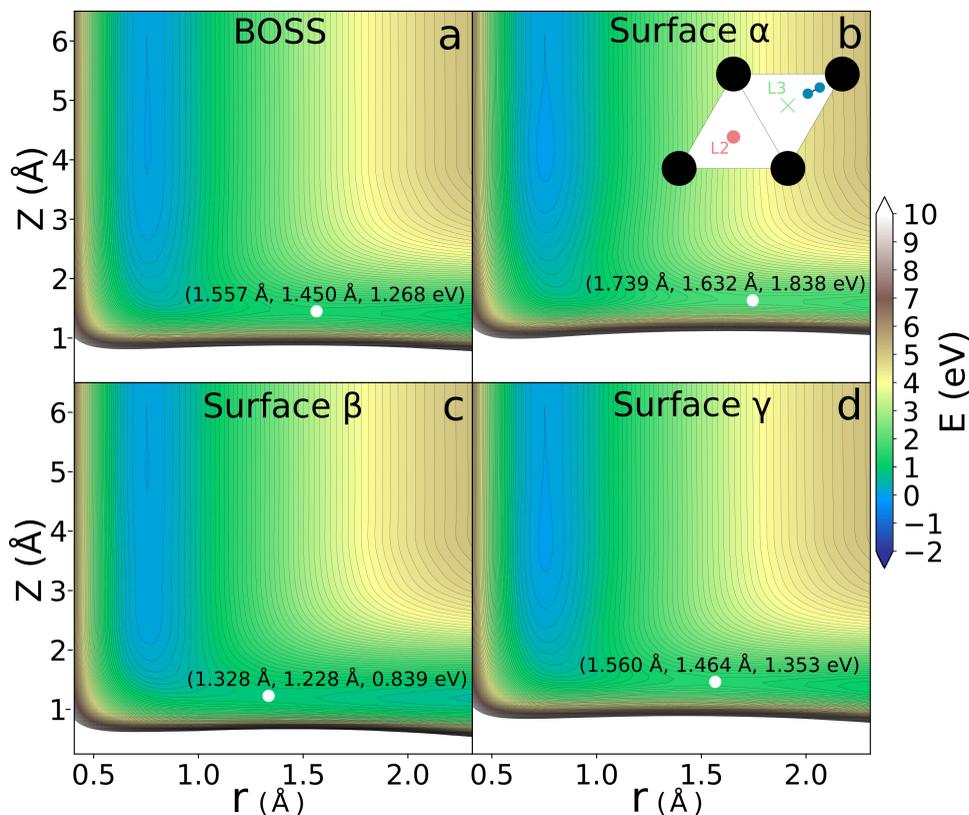
FIGURE 6.3: Potential energy contour plot for the top-to-fcc (ttf) reaction site, as depicted in panel b. The PES was interpolated using the CRP[57] using DFT obtained with the SRP48 functional[22, 58]. Included are the potential for the (a) BOSS approach, as well as three different SCM distorted surfaces: (b) less reactive α, (c) very reactive β, and (d) typical reactivity γ, which have also been discussed in Chapter 4. The transition state for each 2D PES is marked with a white circle, including the location of the barrier in the (r, Z, V) format. The distorted surface slabs for the SCM, at a modelled surface temperature of 925 K, were obtained from Chapter 3.

reactive, and a typically reactive surface slab respectively, while the transition state location is also marked in the (r, Z, V) format for each of these cuts. The ttf reaction site was included specifically due to the large differences in barrier height between the surface slabs we discuss. These same three surface slabs have also previously been discussed in Chapter 4, where their associated reaction and (rovibrationally elastic) scattering probabilities are shown.

Of particular note is the shift of the lowest reaction barrier, both in r and in Z, when the surface is thermally displaced. This shift can have further dynamical effects also on the contribution of rovibrational energies to the dissociation reaction, as we will show in the next sections. Previous studies have already carefully characterised the effect of individual surface atom displacements, both parallel and normal to the surface, on the barrier height and location[18, 21]. Now we also show how all these effects work together to form a very different potential energy landscape between different thermally distorted surfaces. For the (lowest barrier) bth PES cuts (Fig. 6.2) we find that the inclusion of surface temperature effects shifts the location of the reaction barrier toward higher H−H distances, while also slightly moving this barrier closer towards the surface. In contrast, for the lowest reaction barriers of the ttf PES cuts (Fig. 6.3) we find barriers with much lower (higher) r and Z values for the very reactive (non-reactive) surface slab we included. However, even the most reactive barrier here is much higher than the barriers found for the bth site, and is thus more important for higher ends of the dissociation curves. We would, however, also note that this is only a very small part of the dataset of 25.000 distorted surface configurations used in this work, as each distorted surface slab will have a uniquely shaped potential energy landscape.

6.3.3 Time-of-flight spectra and fitted parameters

To get a more direct comparison to the available results of associative desorption experiments, we have simulated time-of-flight spectra for each of our dissociation curves. Here, we rely on detailed balance and several parameters of the experimenal setup by Kaufmann *et al.* to allow for the best possible comparisons to their results. As the experimental setup was recalibrated every day between measurements, we chose a constant time offset ($t_{shift} = 3.2$ μs) and the length of the field-free region ($x_0 = 29.25$ mm) for Eq. 6.4 as was reported in Ref. [7]. For the continuous expression of the dissociation curve, we use the GMP for the v = 0 QD-BOSS and all QD-SCM results, and the FPC for the v = 1 QD-BOSS and all QCD results.

As advised by the experimentalists in private communication, it was also decided to simulate the experimental ToF spectra using their published ERF
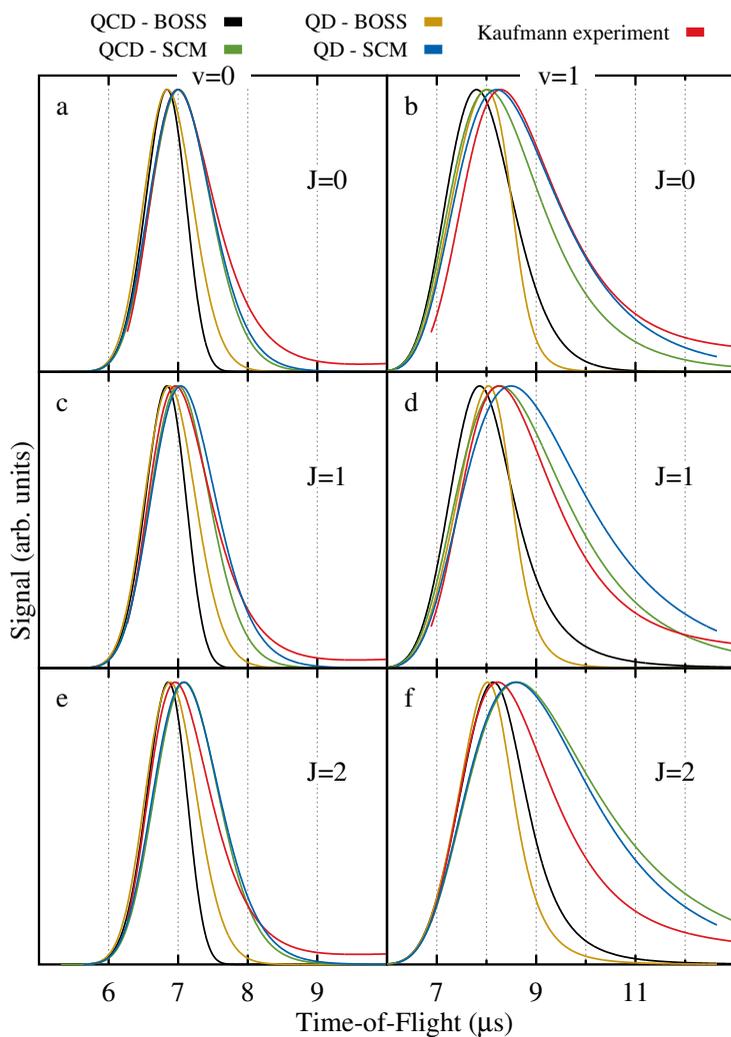
FIGURE 6.4: Simulated time-of-flight spectra for six rovibrational states: v = 0, [(a), (c), and (e)] J = 0, 1, 2 and v = 1, [(b), (d), and (f)] J = 0, 1, 2. Spectra are generated using fits to the QD-SCM (blue), QCD-SCM (green), QD-BOSS (orange), and QCD-BOSS (black) dissociation curves, and fit to the GMP or FPC functional forms. Parts of these dissociation curves are also shown in Chapter 5, Also included are the experimental results by Kaufmann *et al.*[7], simulated using the published ERF function fits including the slow channel. A surface temperature of 925 and 923 K was used for the theoretical and experimental simulation, respectively.

paramters. This should allow for a more direct comparison of the theoretical results to the experimental curves. The cutoff function of equation 6.5 was used for the simulation of both the experimental and the theoretical spectra, with $E_{slope} = 22.8$ eV^{-1} and $E_{min} = 7.2$ meV, using values typically reported by Kaufmann *et al.*[7] Finally, we used a modeled surface temperature of 923 and 925 K for the experimental and theoretical results respectively. Although using only an average of the ToF simulation parameters reduces our ability to directly compare to the experimental results as they were recorded, we believe it will also reduce the error we can expect due to the needed daily calibrations. Similarly, we expect little data to be lost by simulating the experimental spectra from the ERF fits, as they have been shown to be very accurate by the experimentalists[7].

In Fig. 6.4 we present the simulated ToF spectra for several rovibrational states, both for QD- and QCD-SCM and -BOSS results, compared to the simulated experimental results of Kaufmann *et al.* Of note is the broadening of the SCM results when compared to the BOSS spectra, which we attribute to the characteristic curve broadening effect due to surface temperature[60]. Here the lower reaction barrier of some surface configurations improves dissociation, while unfavourable configurations (as well as a recoil effect[61]) reduce reactivity at higher energies. Peak locations found for the SCM are similarly found at a slightly longer ToF compared to the BOSS. We also find good agreement between the QD and QCD results, although some differences are found for the vibrationally excited states, similar to what is observed for the dissociation curves themselves (Chapter 6). In general, the SCM does increase agreement with the experimental spectra for all states, although it appears to perform much better for the vibrational ground states. For the rovibrationally excited states, the SCM appears to somewhat overestimate the widths of the curves.

The theoretical dissociation curves were also fitted to the ERF functional form, described in more detail in section 2.4.2 of Chapter 2. The three fitting parameters obtained for the QD- and QCD-SCM and -BOSS fits are presented in Fig. 6.5 and compared to those obtained from experiment.

While these fits are commonly used to efficiently compare dissociation curves, we also find the ERF functional form performs the worst, of the functional forms we tried, in accurately describing our obtained results from the QD and QCD. Furthermore, studies have shown that the three fitting parameters E_0, W, and A are not fully independent of each other[3, 19]. Nevertheless, some information can be gained by comparing these fitted parameters directly. Experimental saturation values (A) were not included, as they cannot be directly obtained from the desorption experiments, while the experimental width parameters (W) were only reported as a constant value per vibrational state.
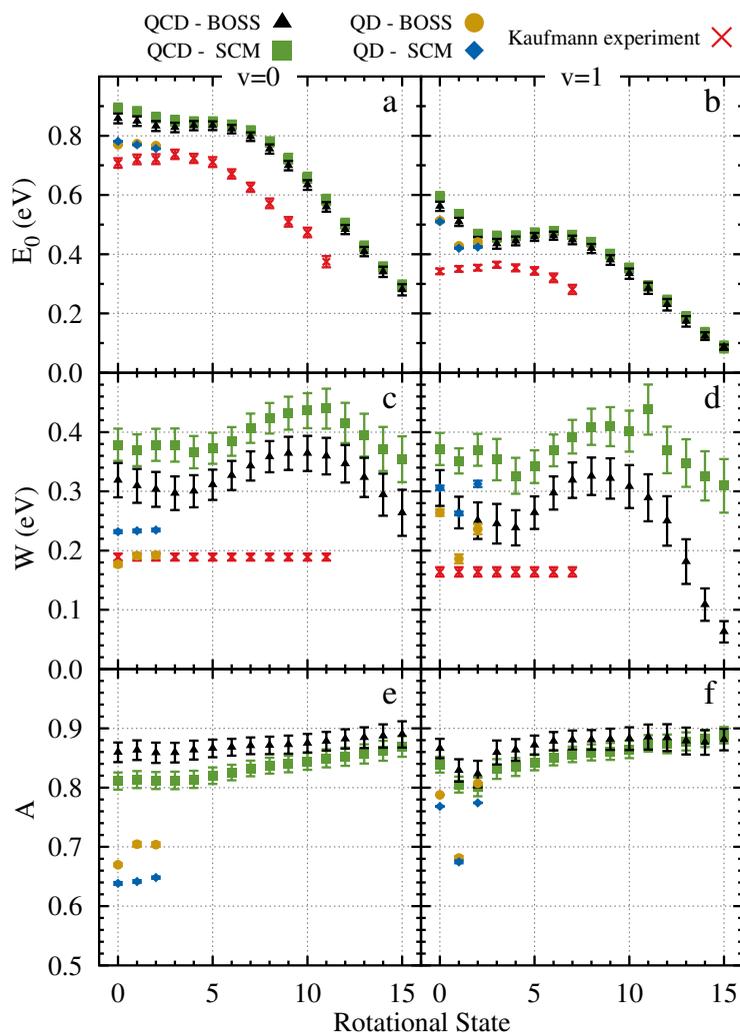
FIGURE 6.5:   Fitted ERF parameters for the fits to the QD-SCM (blue), QCD-SCM (green), QD-BOSS (orange), and QCD-BOSS (black) dissociation curves, for the [(a), (c), and (e)] v = 0 and [(b), (d), and (f)] v = 1 vibrational states, plotted against the rotational (J) state. Included are the: [(a) and (b)] E_0, [(c) and (d)] W, and [(e) and (f)] A parameters, as shown in (2.70) of Chapter 2. Where available, the experimental results of Kaufmann *et al.*[7] are also included. Error bars represent a standard deviation of 2σ, obtained from the fitting procedure.

We observe a slight difference between the E_0 parameters [Fig. 6.5(a),(b)] of the BOSS and SCM approaches, both at the QD and the QCD level. Those parameters found when fitting the QD results are however somewhat lower in energy, more so for the vibrational ground state (a) than the vibrationally excited state (b). The experimental fits yielded even lower values, although qualitatively theory appears to generally predict the right shape as the rotational state increases, where reaction occurs earlier as the rotational energy increases. Only at the lowest rotational states do we see small qualitative differences, where the experiment predicts a small increase in E_0, which theory only finds later around $J = 5$.

For the curve widths (W) [Fig. 6.5(c) and (d)], we see a similar split between experiment and theory, where both the SCM and BOSS predict higher widths than found for the experimental fits. Both the QD- and QCD-SCM results show a higher curve width than the matching QD- and QCD-BOSS results, as is characteristic for surface temperature effects. Focusing on the QCD widths, we see that they generally very slowly decrease as the rotational state increases, which we can attribute to the additional rotational energy helping the molecule pass the barrier without opening up new reaction paths at higher barriers. At higher rotation, the new increase in width could indicate the opening up of later (in r) reaction pathways, which are more efficiently surpassed for molecules with a higher rotational state. This can be understood by the scaling of $\frac{1}{r^2}$ as found in Eq. 2.9. As r increases, the rotational energy of the molecule must decrease to ensure conservation of angular momentum as it approaches the barrier and does not change state. This rotational energy can thus assist in surpassing the dissociation barrier[62]. Finally, at very high J-states even these later barriers are easily passed by the very high (rotational) energy of the molecule, and widths rapidly decrease again. Especially for the vibrationally excited states, this decrease is likely due to the internal energy of the molecule being high enough to allow for the dissociation to occur, even without any significant kinetic energy towards the surface.

It is known that for H_2 on Cu, the vibrational energy can assist in promoting the reaction, which we also discuss in section 6.3.4. Somewhat similar effects were observed in one of the earliest studies using the SCM, however here the decrease in width for the higher (rotational) states was much less apparent[19]. Unfortunately, not enough rotational states have been calculated to attempt a similar analysis for the QD results, and the experimental results were only fitted to a single width per vibrational state.

For the saturation values (A) [Fig. 6.5(e) and (f)] we find that the BOSS approach generally predicts slightly higher values than the SCM, although this difference decreases as the internal energy of the molecule increases. This can

be well explained by a change in barrier heights, locations, and/or the potential energy landscape surrounding these barriers, when considering different surface configurations, which we show to have a major effect (see section 6.3.2). Here, some non-reactive configurations will simply have no clear reaction path on some higher barrier regions of the full potential. These specific surface slabs would then be much less reactive, decreasing the maximum reaction probabilities that are obtained when sampling many configurations.

A also increases very slowly as the internal energy goes up, which can be explained easily by even the highest reaction barriers being more easily overcome in the incidence energy ranges we investigated. The values for the (QCD-)SCM approach increase slightly faster, likely due to the much larger collection of different barriers available due to all the different surface configurations. It is not exactly clear what causes the dip in saturation value around the J = 1 for the vibrationally excited states. Perhaps the low rotational energy combined with the excited vibrational state prevents the molecule from easily surpassing the reaction barrier due to unfavourable rotational angles. In contrast, for the rotational ground state there would be no (significant) rotation to have any effect, while for higher states the much higher rotational energy can more easily facilitate reaction purely energetically.

QD results predict a lower saturation than those obtained with QCD, slightly closer to those predicted by some experimental studies, although it is unclear what could cause this difference. It could be simply related to the fact that energy can be far more easily converted between degrees of freedom in QCD when compared to QD. For QD the molecule cannot as easily convert its quantised internal energy into degrees of freedom related to the reaction path, at least when compared to the classical nature of the QCD.

6.3.4   Rotational and vibrational efficacies

The "threshold offset" parameter (ΔS) will give us an indication of the increase in reaction probability due to the additional internal energy of higher rovibrational states. It is represented by the energy shift that gives the optimal overlap between the results of the rovibrational ground state and the rovibrationally excited states (see Eq. 2.74 of Chapter 2). As was suggested by previous studies, we can use ΔS to determine how efficiently the internal rotational (Eq. 2.75) and vibrational (Eq. 2.76) energies promote the dissociation reaction in a way that is more independent from the functional form chosen when fitting the dissociation curves. Indeed, we find negligible differences in ΔS when obtained from fits to different sigmoid functions (ERF, GMP, and FPC) or even using the raw results directly.
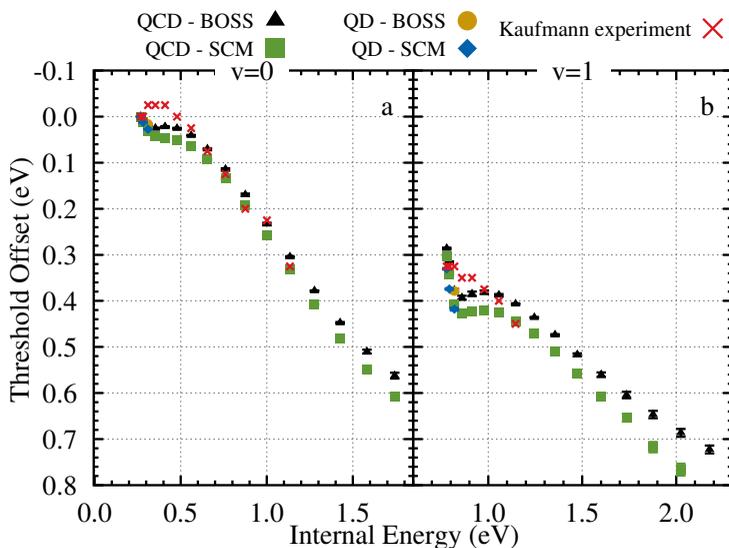
FIGURE 6.6: Threshold offset parameters for the QD-SCM (blue), QCD-SCM (green), QD-BOSS (orange), and QCD-BOSS (black) dissociation curves, for the (a) v = 0 and (b) v = 1 vibrational states, plotted against the total internal (rovibrational) energy of the H_2 molecule. Internal energies are obtained from the FGH method for the SRP48 PES. Where available, the experimental results of Kaufmann *et al.*[7] are also included. Errorbars represent a standard deviation of 2σ, obtained from the fitting procedure.

In Fig. 6.6, we compare the obtained threshold offsets for the vibrational ground state (a) and vibrational excited state (b), plotted for each rovibrational internal energy (obtained from the FGH method). In contrast to experiment, we do not find small negative ΔS values for very low rotational states of the vibrational ground state. Instead, we see a rapid increase in offset value, followed by a small region of constant shift around J = 5, which is especially noticeable for the v = 1 results. This observation is also reflected in the similar behaviour of the E_0 parameters presented in Fig. 6.5. For the higher internal energies, at higher rotational states, we see both theory and experiment move towards a linear section. Interestingly the QCD-SCM results appear to increase slightly more rapidly compared to the QCD-BOSS results, which is more obvious for the v=1 states in Fig. 6.6(b). This more rapid increase, combined with the generally higher values found for the SCM results, would indicate that the internal energy of the H_2 molecule can be more easily used to surpass the dissociation barrier of the thermally distorted surfaces compared to the perfect crystal lattice. This observation could be explained by the much more varied number of barriers encountered on the distorted surfaces, and their sensitivity to different rovibrational energies. The agreement between the QCD and QD results appears to be excellent, although little can be concluded of the shape of the full range of internal energy due to the limited amount of QD data available.

The rotational efficacies in Fig. 6.7. show the expected trends based on these threshold offsets. The differences between the theory and experiment, however, are much more pronounced as the rotational energies are in the same order of magnitude as the threshold offsets when considering the lower rotational states. Due to these smaller energies, we also expect there to be larger errors present both in the theoretical and experimental results. Nevertheless, we do expect the basic trends we describe, and the comparisons between the purely theoretically obtained results below, to be accurate enough. For the low rotational states, experiments predict a negative rotational efficacy, where rotation actually hinders the dissociation reaction, known as "rotational cooling"[3] In contrast, our theoretical results fail to predict this cooling, instead showing a very efficient use of rotational energy to pass the reaction barrier. For the vibrationally excited states in panel (b), we even find efficacies above 1, which would indicate 1 meV of rotational energy would help passing over more than 1 meV of reaction barrier. This then would be well explained by very late reaction barriers, where rotational energy can greatly contribute to the dissociation reaction. QD- and QCD-SCM efficacies appear to be slightly higher than those found for the BOSS results, which again indicates the rotational energy can be more efficiently used to pass the barrier at low J-states. This observation matches well with the later barriers (in r) we find in Fig. 6.2. Nevertheless, the SCM, BOSS, as
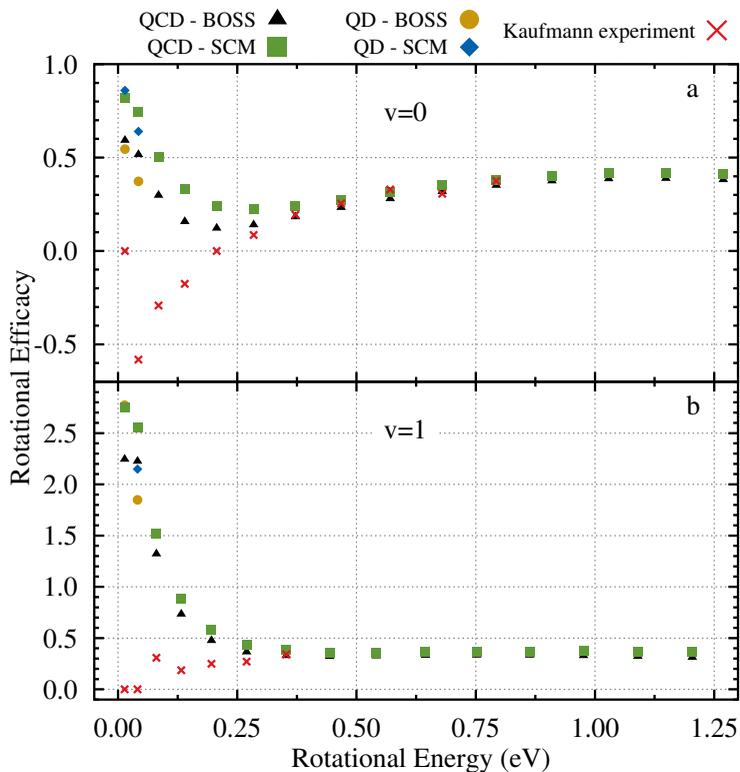
FIGURE 6.7: Rotational efficacies obtained for the QD-SCM (blue), QCD-SCM (green), QD-BOSS (orange), and QCD-BOSS (black) dissociation curves. Data are included for the (a) v=0 and (b) v=1 vibrational states, plotted against the rotational energy of the H_2 molecule. Rotational energies are obtained from the FGH method for the SRP48 PES, calculated using Eq. 2.75. Where available, the experimental results of Kaufmann *et al.*[7] are also included.

TABLE 6.1: Vibrational efficacies for the QD-SCM, QCD-SCM, QD-BOSS, and QCD-BOSS approaches, as well as the experimental results of Kaufmann *et al.*[7], calculated using Eq. 2.76.

	QD		QCD		Experiment
	BOSS	SCM	BOSS	SCM	
μ_{vib}	0.593	0.645	0.560	0.595	0.636

well as experimental results all show a rotational efficacy of around 0.40 at higher rotational states, with the SCM efficacies perhaps ever so slightly higher. Again, we do see a good agreement between the QD and QCD results, but the limited amount of QD states sampled makes it difficult to draw any definitive conclusions.

The vibrational efficacies we find, as presented in Table 6.1, agree well with each other and the experimental results. The QD results are generally slightly higher than those of the QCD, opposite to what we find for μ_{rot}. However, we do again find slightly higher efficacies for the SCM results, compared to BOSS. Thus our model predicts that the surface distortions allow for a more efficient use of vibrational, as well as rotational, energy to pass the dissociation barrier of the surface. This can, at least partially, be explained by the large number of different potential energy landscapes we investigate when applying the SCM and its large number of different surface configurations. Nevertheless, it is likely that energetic effects also play a role.

6.3.5 Rotational quadrupole alignment parameter

Finally, we will discuss another way of looking at the effect of the internal orientation of the molecule on the reaction: the rotational quadrupole alignment parameter (RQAP). This parameter describes the molecule's "preference" of reacting either initially rotating normal to the surface (cartwheel) for negative values, or parallel to the surface (helicopter) for positive values. At exactly 0 we find no preference for either. Previous studies have also calculated this parameter using QD methods for H_2/D_2 on perfect crystal Cu(111)[22, 58, 63, 64], Cu(100)[65] and Cu(211)[66] surfaces. Similarly, a previous study has already shown that the SCM can predict these RQAPs for the D_2/Cu(111) system, although this was only checked at a QC level[19]. However, to our knowledge, RQAPs computed using both QCD and QD including surface temperature effects have never been compared to each other directly, especially obtained using the same potential and based on the same underlying (SRP-DFT) functional. Yet they are of special interest for our methods, as surface
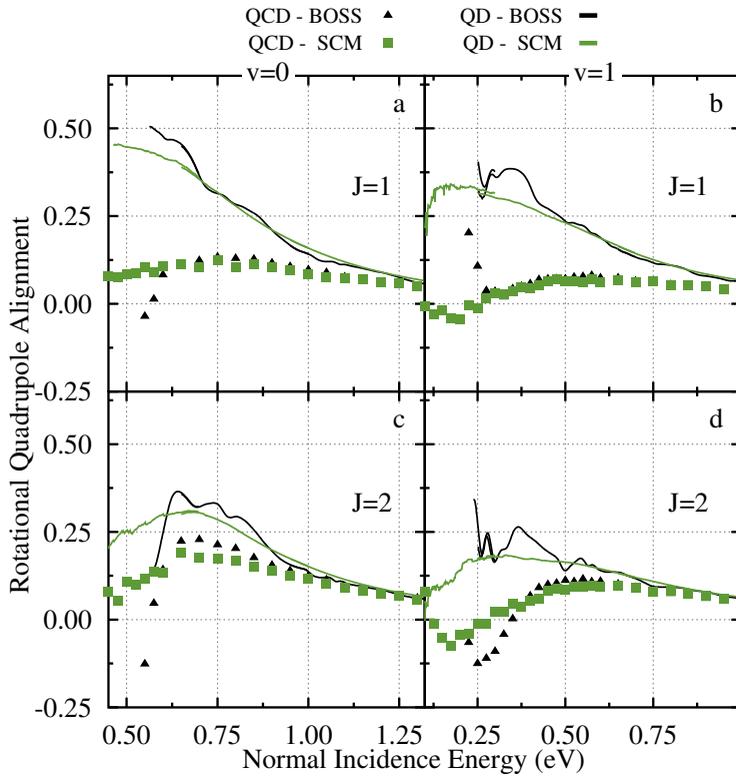
FIGURE 6.8: Rotational quadrupole alignment parameters obtained for the SCM (green curves and squares) and the BOSS (black curves and triangles) approaches for the v = 0; J = 1, J = 2 [(a) and (c)] and the v = 1; J = 1, J = 2 [(b) and (d)] rovibrational states. QD results are shown as curves, while QCD results are included as symbols (squares and triangles), calculated using Eq. 6.3.
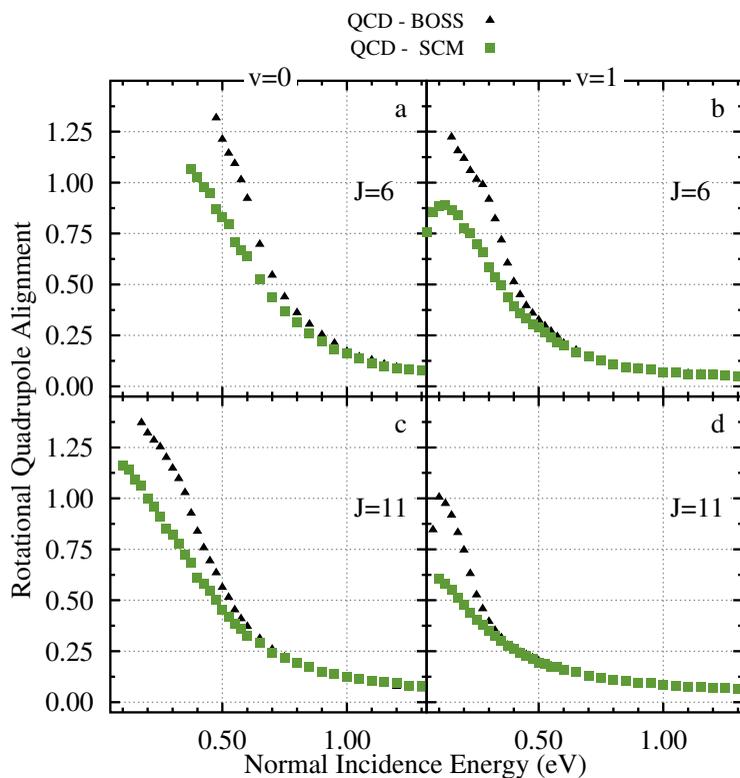
FIGURE 6.9:   Rotational quadrupole alignment parameters obtained for the SCM (green squares) and the BOSS (black triangles) approaches for the $v = 0$; $J = 6$, $J = 11$ [(a) and (c)] and the $v = 1$; $J = 6$, $J = 11$ [(b) and (d)] rovibrational states. The parameters are calculated using Eq. 6.3.

temperature effects have previously been shown to clearly affect their values[19, 58]. RQAPs, as shown in figures 6.8 and 6.9, were only computed for those incidence energies with a reaction probability higher than 1%, with the QD-SCM results per surface only included in the average above this same value. Especially for the QD-SCM this greatly reduced the noise at very low energy, but did not affect the qualitative shape of the curves.

In general, we find that the QD simulations predict much higher RQAPs than the QCD results, both for the BOSS and the SCM approaches. A smaller effect was previously also observed for these states [64]. It is not immediately clear why these QD alignment parameters are much higher. One could argue that QCD allows for a much simpler redistribution of the internal rovibrational energies during dynamics, when compared to the QD simulations, which makes it easier to promote reaction even when the initial state is not favourable. Interestingly, in the case of higher rotational states, where there are a lot more states available, this effect appears to be mostly gone (Fig. 6.9) For these higher rotational states, no QD simulations were available for comparison.

For almost every curve, the highest alignments are not found at the lowest energy we include, instead only slightly behind these lowest barriers. This would then imply at least some of the lowest reaction barriers show less of a preference for rotation parallel to the surface. However, lower incidence energies also allow the molecule more time to favourably align itself to more easily surpass the reaction barriers, as the RQAPs are only determined using the initial rovibrational state in the gas phase. Furthermore, the location of the (energetically) available barriers could equally affect the amount of dynamical effects, such as rotational enhancement, that dominate for the different incidence energies. Indeed, for some rovibrational states we even find negative RQAPs at low energy, implying a preference for more "cartwheel"-like rotation. No clear difference is found between the BOSS and SCM results at these lower rotational states, although especially the QD curves do show the BOSS to predict somewhat higher alignment parameters near the peak of the curves. This difference becomes much more apparent at higher J-states, as was observed in previous work[19]. This effect can be well explained by the distorted surface configurations modifying the reaction barriers to be less ideal for the "helicopter"-like rotation, as the surface atoms are displaced in Z towards (or away) from the incoming reactant[58].

6.4 Conclusion

We have presented our deeper analysis of the previously published 6D quantum dynamical and quasi-classical results of H_2 dissociating on a thermally distorted

Cu(111) surface using the static corrugation model. As was suggested in the previous study, we show that the upturn in reaction probability we find at very low incidence energies, both for QD-BOSS and -SCM, can be entirely removed by propagating the 6D WPs with a smaller time step. Additional analysis with the flux analysis method similarly showed the upturn to not be explained by parts of the wavepackets passing past the reaction barrier in large r (H↔H) ranges.

We show how the thermal distortion of the Cu(111) surface also leads to changes in not only the barrier height, but also the barrier location and the shape of the reaction channel, when considering the H_2 dissociation, with the lowest reaction barrier moving toward slightly higher r and lower Z values.

Expanding the available QD results with several higher energy WPs, the dissociation curves obtained from theory were fitted to several sigmoidal functions, which were used to simulate time-of-flight spectra. We found improved agreement between the spectra available from the state-of-the-art desorption experiments and our (QD-)SCM approach when describing the H_2 dissociation reaction. The fitted parameters of the ERF sigmoidal function also showed a clear effect of curve broadening when surface temperature is included in the model, as well as small surface temperature effects. These smaller effects could be well explained by changes in both barrier height and location, due to the thermal surface distortions.

Next we calculated a threshold offset parameter for our results, which describes the energy shift required for a curve at a higher internal energy to match that of the rovibrational ground state. These parameters were used to calculate the rotational and vibrational efficacies of our models, which were compared those to the values found in experiments. As expected, our theoretical results reproduced experiment well for these parameters, although the overall effect of surface temperature on these parameters appeared to be very minor. Only for very low rotational energies did we find differences compared to experiment, where the rotational efficacy is predicted to be negative, which is not reproduced by any of our theoretical approaches.

Finally, we also computed rotational quadrupole alignment parameters to analyse the impact of the different rotational states on the reaction from another angle. Here we found a much larger preference for the incoming H_2 to react with a rotation parallel to the surface when using our QD methods, compared to the QCD methods.

Overall, this work present a wide database of experimentally obtainable parameters that can be used to validate the quality of our current and other theoretical and experimental works, when looking at the H_2 on Cu(111) dissociation reaction.

6.A Appendix: Additional computational details

TABLE 6.A.1: Computational details for the TDWP quantum dynamics simulations of H_2 dissociation on a Cu(111) surface.

	0.10-0.30 eV	0.25-0.70 eV
Z_{start} (a_0)	-1.0	-1.0
$N_{Z_{spec}}$	180	256
N_Z	128	180
ΔZ (a_0)	0.15	0.15
Z_{ana} (a_0)	9.20	12.05
R_{start} (a_0)	0.60	0.60
N_r	64	64
ΔR (a_0)	0.15	0.15
N_x	24	24
N_y	24	24
Max. J in basis set	18	18
Max. m_J in basis set	12	12
SCM cutoff (a_0)	16.0	16.0
Complex absorbing potentials		
Z^{CAP} start (a_0)	9.35	12.20
Z^{CAP} end (a_0)	18.05	25.85
Z^{CAP} optimum (eV)	0.05	0.125
Z_{spec}^{CAP} start (a_0)	17.00	31.95
Z_{spec}^{CAP} end (a_0)	25.85	37.25
Z_{spec}^{CAP} optimum (eV)	0.05	0.125
R^{CAP} start (a_0)	4.20	4.20
R^{CAP} end (a_0)	10.05	10.05
R^{CAP} optimum (eV)	0.10	0.10
Propagation		
Δt ($\hbar/E_h$)	1.5	2.5
t_f ($\hbar/E_h$)	60000	45000
Initial wave packet		
E_{min} (eV)	0.10	0.25
E_{max} (eV)	0.30	0.70
Z_0 (a_0)	13.10	21.95

6

6

TABLE 6.A.2: Additional computational details for the TDWP quantum dynamics simulations of H$_2$ dissociation on a Cu(111) surface.

	0.65-1.00 eV	0.95-1.50 eV
Z$_{start}$ (a$_0$)	-1.0	-1.0
N$_{Z_{spec}}$	256	256
N$_Z$	180	180
ΔZ (a$_0$)	0.15	0.12
Z$_{ana}$ (a$_0$)	12.05	12.08
R$_{start}$ (a$_0$)	0.60	0.60
N$_r$	64	64
ΔR (a$_0$)	0.15	0.15
N$_x$	24	24
N$_y$	24	24
Max. J in basis set	18	18
Max. m$_J$ in basis set	12	12
SCM cutoff (a$_0$)	16.0	16.0
Complex absorbing potentials		
Z^{CAP} start (a$_0$)	12.20	12.20
Z^{CAP} end (a$_0$)	25.85	20.48
Z^{CAP} optimum (eV)	0.325	0.475
Z$^{CAP}_{spec}$ start (a$_0$)	31.95	21.68
Z$^{CAP}_{spec}$ end (a$_0$)	37.25	29.60
Z$^{CAP}_{spec}$ optimum (eV)	0.325	0.475
R^{CAP} start (a$_0$)	4.20	4.20
R^{CAP} end (a$_0$)	10.05	10.05
R^{CAP} optimum (eV)	0.10	0.10
Propagation		
Δt ($\hbar$/E$_h$)	2.5	2.5
t$_f$ ($\hbar$/E$_h$)	45000	45000
Initial wave packet		
E$_{min}$ (eV)	0.65	0.95
E$_{max}$ (eV)	1.00	1.50
Z$_0$ (a$_0$)	21.95	16.88

TABLE 6.A.3: Additional computational details for the TDWP quantum dynamics simulations of H_2 dissociation on a Cu(111) surface.

	Low time step	Flux analysis
Z_{start} (a_0)	-1.0	-1.0
$N_{Z_{spec}}$	512	512
N_Z	180	180
ΔZ (a_0)	0.15	0.15
Z_{ana} (a_0)	15.20	15.20
R_{flux} (a_0)	3.85	3.85
R_{start} (a_0)	0.40	0.40
N_r	64	64
ΔR (a_0)	0.15	0.15
N_x	16	16
N_y	16	16
Max. J in basis set	12	12
Max. m_J in basis set	8	8
Complex absorbing potentials		
Z^{CAP} start (a_0)	15.20	12.20
Z^{CAP} end (a_0)	25.85	25.85
Z^{CAP} optimum (eV)	0.05	0.05
Z^{CAP}_{spec} start (a_0)	36.80	36.80
Z^{CAP}_{spec} end (a_0)	75.65	75.65
Z^{CAP}_{spec} optimum (eV)	0.05	0.05
R^{CAP} start (a_0)	4.30	4.30
R^{CAP} end (a_0)	8.20	8.20
R^{CAP} optimum (eV)	0.10	0.10
Propagation		
Δt ($\hbar/E_h$)	0.1	2.0
t_f ($\hbar/E_h$)	180000	180000
Initial wave packet		
E_{min} (eV)	0.10	0.10
E_{max} (eV)	0.30	0.30
Z_0 (a_0)	26.0	26.0

6

References

(1)   Berger, H. F.; Leisch, M.; Winkler, A.; Rendulic, K. D. A Search for Vibrational Contributions to the Activated Adsorption of H_2 on Copper. *Chemical Physics Letters* **1990**, *175*, 425–428, DOI: 10.1016/0009-2614(90)85558-T.

(2)   Michelsen, H. A.; Rettner, C. T.; Auerbach, D. J.; Zare, R. N. Effect of rotation on the translational and vibrational energy dependence of the dissociative adsorption of D_2 on Cu(111). *The Journal of Chemical Physics* **1993**, *98*, 8294–8307, DOI: 10.1063/1.464535.

(3)   Rettner, C. T.; Michelsen, H. A.; Auerbach, D. J. Quantum-state-specific dynamics of the dissociative adsorption and associative desorption of H_2 at a Cu(111) surface. *The Journal of Chemical Physics* **1995**, *102*, 4625–4641, DOI: 10.1063/1.469511.

(4)   Hodgson, A.; Samson, P.; Wight, A.; Cottrell, C. Rotational Excitation and Vibrational Relaxation of H_2 Scattered from Cu(111). *Physical Review Letters* **1997**, *78*, 963–966, DOI: 10.1103/PhysRevLett.78.963.

(5)   Hou, H.; Gulding, S. J.; Rettner, C. T.; Wodtke, A. M.; Auerbach, D. J. The Stereodynamics of a Gas-Surface Reaction. *Science* **1997**, *277*, 80–82, DOI: 10.1126/science.277.5322.80.

(6)   Murphy, M. J.; Hodgson, A. Adsorption and desorption dynamics of H_2 and D_2 on Cu(111): The role of surface temperature and evidence for corrugation of the dissociation barrier. *The Journal of Chemical Physics* **1998**, *108*, 4199–4211, DOI: 10.1063/1.475818.

(7)   Kaufmann, S.; Shuai, Q.; Auerbach, D. J.; Schwarzer, D.; Wodtke, A. M. Associative desorption of hydrogen isotopologues from copper surfaces: Characterization of two reaction mechanisms. *The Journal of Chemical Physics* **2018**, *148*, 194703, DOI: 10.1063/1.5025666.

(8)   Chadwick, H.; Somers, M. F.; Stewart, A. C.; Alkoby, Y.; Carter, T. J. D.; Butkovicova, D.; Alexandrowicz, G. Stopping Molecular Rotation Using Coherent Ultra-Low-Energy Magnetic Manipulations. *Nature Communications* **2022**, *13*, 2287, DOI: 10.1038/s41467-022-29830-3.

(9)   Díaz, C.; Pijper, E.; Olsen, R. A.; Busnengo, H. F.; Auerbach, D. J.; Kroes, G. J. Chemically accurate simulation of a prototypical surface reaction: H_2 dissociation on Cu(111). *Science (New York, N.Y.)* **2009**, *326*, 832–834, DOI: 10.1126/science.1178722.

(10) Zhu, L.; Zhang, Y.; Zhang, L.; Zhou, X.; Jiang, B. Unified and transferable description of dynamics of H_2 dissociative adsorption on multiple copper surfaces *via* machine learning. *Physical Chemistry Chemical Physics* **2020**, *22*, 13958–13964, DOI: 10.1039/D0CP02291H.

(11) Galparsoro, O.; Kaufmann, S.; Auerbach, D. J.; Kandratsenka, A.; Wodtke, A. M. First Principles Rates for Surface Chemistry Employing Exact Transition State Theory: Application to Recombinative Desorption of Hydrogen from Cu(111). *Physical Chemistry Chemical Physics* **2020**, *22*, 17532–17539, DOI: 10.1039/D0CP02858D.

(12) Smits, B.; Somers, M. F. Beyond the static corrugation model: Dynamic surfaces with the embedded atom method. *The Journal of Chemical Physics* **2021**, *154*, 074710, DOI: 10.1063/5.0036611.

(13) Smeets, E. W. F.; Kroes, G.-J. Designing New SRP Density Functionals Including Non-Local vdW-DF2 Correlation for H_2 + Cu(111) and Their Transferability to H_2 + Ag(111), Au(111) and Pt(111). *Physical Chemistry Chemical Physics* **2021**, *23*, 7875–7901, DOI: 10.1039/D0CP05173J.

(14) Smeets, E. W. F.; Kroes, G.-J. Performance of Made Simple Meta-GGA Functionals with rVV10 Nonlocal Correlation for H_2 + Cu(111), D_2 + Ag(111), H_2 + Au(111), and D_2 + Pt(111). *The Journal of Physical Chemistry C* **2021**, *125*, 8993–9010, DOI: 10.1021/acs.jpcc.0c11034.

(15) Smits, B.; Litjens, L. G. B.; Somers, M. F. Accurate Description of the Quantum Dynamical Surface Temperature Effects on the Dissociative Chemisorption of H_2 from Cu(111). *The Journal of Chemical Physics* **2022**, *156*, 214706, DOI: 10.1063/5.0094985.

(16) Smits, B.; Somers, M. F. The Quantum Dynamics of H_2 on Cu(111) at a Surface Temperature of 925 K: Comparing State-of-the-Art Theory to State-of-the-Art Experiments. *The Journal of Chemical Physics* **2022**, *157*, 134704, DOI: 10.1063/5.0112036.

(17) Díaz, C.; Olsen, R. A.; Auerbach, D. J.; Kroes, G. J. Six-Dimensional Dynamics Study of Reactive and Non Reactive Scattering of H_2 from Cu(111) Using a Chemically Accurate Potential Energy Surface. *Physical Chemistry Chemical Physics* **2010**, *12*, 6499–6519, DOI: 10.1039/C0019 56A.

(18) Bonfanti, M.; Díaz, C.; Somers, M. F.; Kroes, G.-J. Hydrogen Dissociation on Cu(111): The Influence of Lattice Motion. Part I. *Physical Chemistry Chemical Physics* **2011**, *13*, 4552, DOI: 10.1039/c0cp01746a.

6

(19) Wijzenbroek, M.; Somers, M. F. Static surface temperature effects on the dissociation of H_2 and D_2 on Cu(111). *The Journal of Chemical Physics* **2012**, *137*, 054703, DOI: 10.1063/1.4738956.

(20) Nattino, F.; Genova, A.; Guijt, M.; Muzas, A. S.; Díaz, C.; Auerbach, D. J.; Kroes, G.-J. Dissociation and recombination of D_2 on Cu(111): ab initio molecular dynamics calculations and improved analysis of desorption experiments. *The Journal of Chemical Physics* **2014**, *141*, 124705, DOI: 10.1063/1.4896058.

(21) Bonfanti, M.; Somers, M. F.; Díaz, C.; Busnengo, H. F.; Kroes, G.-J. 7D Quantum Dynamics of H_2 Scattering from Cu(111): The Accuracy of the Phonon Sudden Approximation. *Zeitschrift für Physikalische Chemie* **2013**, 130617035227002, DOI: 10.1524/zpch.2013.0405.

(22) Mondal, A.; Wijzenbroek, M.; Bonfanti, M.; Díaz, C.; Kroes, G.-J. Thermal Lattice Expansion Effect on Reactive Scattering of H_2 from Cu(111) at T_s = 925 K. *The Journal of Physical Chemistry A* **2013**, *117*, 8770–8781, DOI: 10.1021/jp4042183.

(23) Kroes, G.-J.; Juaristi, J. I.; Alducin, M. Vibrational Excitation of H_2 Scattering from Cu(111): Effects of Surface Temperature and of Allowing Energy Exchange with the Surface. *The Journal of Physical Chemistry C* **2017**, *121*, 13617–13633, DOI: 10.1021/acs.jpcc.7b01096.

(24) Spiering, P.; Wijzenbroek, M.; Somers, M. F. An improved static corrugation model. *The Journal of Chemical Physics* **2018**, *149*, 234702, DOI: 10.1063/1.5058271.

(25) Smith, C.; Hill, A. K.; Torrente-Murciano, L. Current and future role of Haber–Bosch ammonia in a carbon-free energy landscape. *Energy & Environmental Science* **2020**, *13*, 331–344, DOI: 10.1039/C9EE02873K.

(26) Chorkendorff, I., *Concepts of Modern Catalysis and Kinetics*; Wiley-VCH: Weinheim, 2003.

(27) Kroes, G.-J.; Díaz, C. Quantum and classical dynamics of reactive scattering of H_2 from metal surfaces. *Chemical Society Reviews* **2016**, *45*, 3658–3700, DOI: 10.1039/c5cs00336a.

(28) Kroes, G.-J. Computational approaches to dissociative chemisorption on metals: towards chemical accuracy. *Physical Chemistry Chemical Physics* **2021**, *23*, 8962–9048, DOI: 10.1039/D1CP00044F.

(29) Xiao, Y.; Dong, W.; Busnengo, H. F. Reactive force fields for surface chemical reactions: A case study with hydrogen dissociation on Pd surfaces. *The Journal of Chemical Physics* **2010**, *132*, 014704, DOI: 10.1063/1.3265854.

(30) Lozano, A.; Shen, X. J.; Moiraghi, R.; Dong, W.; Busnengo, H. F. Cutting a chemical bond with demon's scissors: Mode- and bond-selective reactivity of methane on metal surfaces. *Surface Science* **2015**, *640*, 25–35, DOI: 10.1016/j.susc.2015.04.002.

(31) Seminara, G. N.; Peludhero, I. F.; Dong, W.; Martínez, A. E.; Busnengo, H. F. Molecular Dynamics Study of Molecular and Dissociative Adsorption Using System-Specific Force Fields Based on Ab Initio Calculations: $CO/Cu(110)$ and $CH_4/Pt(110)$. *Topics in Catalysis* **2019**, *62*, 1044–1052, DOI: 10.1007/s11244-019-01196-9.

(32) Tiwari, A. K.; Nave, S.; Jackson, B. The temperature dependence of methane dissociation on Ni(111) and Pt(111): Mixed quantum-classical studies of the lattice response. *The Journal of Chemical Physics* **2010**, *132*, 134702, DOI: 10.1063/1.3357415.

(33) Guo, H.; Farjamnia, A.; Jackson, B. Effects of Lattice Motion on Dissociative Chemisorption: Toward a Rigorous Comparison of Theory with Molecular Beam Experiments. *The Journal of Physical Chemistry Letters* **2016**, *7*, 4576–4584, DOI: 10.1021/acs.jpclett.6b01948.

(34) Jackson, B. The Trapping of Methane on Ir(111): A First-Principles Quantum Study. *The Journal of Chemical Physics* **2021**, *155*, 044705, DOI: 10.1063/5.0058672.

(35) Jackson, B. Quantum studies of methane-metal inelastic diffraction and trapping: The variation with molecular orientation and phonon coupling. *Chemical Physics* **2022**, *559*, 111516, DOI: 10.1016/j.chemphys.2022.111516.

(36) Kroes, G. J.; Wijzenbroek, M.; Manson, J. R. Possible effect of static surface disorder on diffractive scattering of H_2 from Ru(0001): Comparison between theory and experiment. *The Journal of Chemical Physics* **2017**, *147*, 244705, DOI: 10.1063/1.5011741.

(37) Dutta, J.; Mandal, S.; Adhikari, S.; Spiering, P.; Meyer, J.; Somers, M. F. Effect of surface temperature on quantum dynamics of H_2 on Cu(111) using a chemically accurate potential energy surface. *The Journal of Chemical Physics* **2021**, *154*, 104103, DOI: 10.1063/5.0035830.

6

(38) Dutta, J.; Naskar, K.; Adhikari, S.; Spiering, P.; Meyer, J.; Somers, M. F. Effect of surface temperature on quantum dynamics of D_2 on Cu(111) using a chemically accurate potential energy surface, To Be Submitted, 2022, submitted.

(39) Craig, I. R.; Manolopoulos, D. E. Quantum Statistics and Classical Mechanics: Real Time Correlation Functions from Ring Polymer Molecular Dynamics. *The Journal of Chemical Physics* **2004**, *121*, 3368–3373, DOI: 10.1063/1.1777575.

(40) Suleimanov, Y. V.; Aoiz, F. J.; Guo, H. Chemical Reaction Rate Coefficients from Ring Polymer Molecular Dynamics: Theory and Practical Applications. *The Journal of Physical Chemistry A* **2016**, *120*, 8488–8502, DOI: 10.1021/acs.jpca.6b07140.

(41) Behler, J. First Principles Neural Network Potentials for Reactive Simulations of Large Molecular and Condensed Systems. *Angewandte Chemie International Edition* **2017**, *56*, 12828–12840, DOI: https://doi.org/10.1002/anie.201703114.

(42) Artrith, N.; Behler, J. High-dimensional neural network potentials for metal surfaces: A prototype study for copper. *Physical Review B* **2012**, *85*, 045439, DOI: 10.1103/PhysRevB.85.045439.

(43) Lin, Q.; Zhang, L.; Zhang, Y.; Jiang, B. Searching Configurations in Uncertainty Space: Active Learning of High-Dimensional Neural Network Reactive Potentials. *Journal of Chemical Theory and Computation* **2021**, *17*, 2691–2701, DOI: 10.1021/acs.jctc.1c00166.

(44) Olsen, R. A.; Kroes, G. J.; Lo/vvik, O. M.; Baerends, E. J. The Influence of Surface Motion on the Direct Subsurface Absorption of H_2 on Pd(111). *The Journal of Chemical Physics* **1997**, *107*, 10652–10661, DOI: 10.1063/1.474181.

(45) Kroes, G.-J.; Somers, M. F. Six-dimensional dynamics of dissociative chemisorption of H_2 on metal surfaces. *Journal of Theoretical and Computational Chemistry* **2005**, *04*, 493–581, DOI: 10.1142/S0219633605001647.

(46) Chadwick, H.; Alkoby, Y.; Cantin, J. T.; Lindebaum, D.; Godsi, O.; Maniv, T.; Alexandrowicz, G. Molecular spin echoes; multiple magnetic coherences in molecule surface scattering experiments. *Physical Chemistry Chemical Physics* **2021**, *23*, 7673–7681, DOI: 10.1039/D0CP05399F.

(47) Vibok, A.; Balint-Kurti, G. G. Parametrization of complex absorbing potentials for time-dependent quantum dynamics. *The Journal of Physical Chemistry* **1992**, *96*, 8712–8719, DOI: 10.1021/j100201a012.

(48) Balint-Kurti, G. G.; Dixon, R. N.; Marston, C. C. Grid methods for solving the Schrödinger equation and time dependent quantum dynamics of molecular photofragmentation and reactive scattering processes. *International Reviews in Physical Chemistry* **1992**, *11*, 317–344, DOI: 10.1080/01442359209353274.

(49) Neuhauser, D.; Baer, M.; Judson, R. S.; Kouri, D. J. The Application of Time-Dependent Wavepacket Methods to Reactive Scattering. *Computer Physics Communications* **1991**, *63*, 460–481, DOI: 10.1016/0010-4655(91)90270-U.

(50) Zhang, D. H.; Zhang, J. Z. H. Full-dimensional Time-dependent Treatment for Diatom–Diatom Reactions: The H_2+OH Reaction. *The Journal of Chemical Physics* **1994**, *101*, 1146–1156, DOI: 10.1063/1.467808.

(51) Gulding, S. J.; Wodtke, A. M.; Hou, H.; Rettner, C. T.; Michelsen, H. A.; Auerbach, D. J. Alignment of $D_2(v, J)$ Desorbed from Cu(111): Low Sensitivity of Activated Dissociative Chemisorption to Approach Geometry. *The Journal of Chemical Physics* **1996**, *105*, 9702–9705, DOI: 10.1063/1.472979.

(52) Wetzig, D.; Rutkowski, M.; David, R.; Zacharias, H. Rotational Corrugation in Associative Desorption of D_2 from Cu(111). *Europhysics Letters* **1996**, *36*, 31, DOI: 10.1209/epl/i1996-00183-2.

(53) Shuai, Q.; Kaufmann, S.; Auerbach, D. J.; Schwarzer, D.; Wodtke, A. M. Evidence for Electron–Hole Pair Excitation in the Associative Desorption of H_2 and D_2 from Au(111). *The Journal of Physical Chemistry Letters* **2017**, *8*, 1657–1663, DOI: 10.1021/acs.jpclett.7b00265.

(54) Kroes, G. J.; Wiesenekker, G.; Baerends, E. J.; Mowrey, R. C.; Neuhauser, D. Dissociative Chemisorption of H_2 on Cu(100): A Four-dimensional Study of the Effect of Parallel Translational Motion on the Reaction Dynamics. *The Journal of Chemical Physics* **1996**, *105*, 5979–5998, DOI: 10.1063/1.472450.

(55) Kroes, G. J.; Baerends, E. J.; Mowrey, R. C. Six-Dimensional Quantum Dynamics of Dissociative Chemisorption of ($v = 0, j = 0$) H_2 on Cu(100). *Physical Review Letters* **1997**, *78*, 3583–3586, DOI: 10.1103/PhysRevLett.78.3583.

(56) Leforestier, C.; Bisseling, R. H.; Cerjan, C.; Feit, M. D.; Friesner, R.; Guldberg, A.; Hammerich, A.; Jolicard, G.; Karrlein, W.; Meyer, H. .-.; Lipkin, N.; Roncero, O.; Kosloff, R. A Comparison of Different Propagation Schemes for the Time Dependent Schrödinger Equation. *Journal of Computational Physics* **1991**, *94*, 59–80, DOI: 10.1016/0021-9991(91)90137-A.

(57) Busnengo, H. F.; Salin, A.; Dong, W. Representation of the 6D potential energy surface for a diatomic molecule near a solid surface. *The Journal of Chemical Physics* **2000**, *112*, 7641–7651, DOI: 10.1063/1.481377.

(58) Nattino, F.; Díaz, C.; Jackson, B.; Kroes, G.-J. Effect of Surface Motion on the Rotational Quadrupole Alignment Parameter of D_2 Reacting on Cu(111). *Physical Review Letters* **2012**, *108*, 236104, DOI: 10.1103/PhysRevLett.108.236104.

(59) Sheng, H. W.; Kramer, M. J.; Cadien, A.; Fujita, T.; Chen, M. W. Highly optimized embedded-atom-method potentials for fourteen fcc metals. *Physical Review B* **2011**, *83*, 134118, DOI: 10.1103/PhysRevB.83.134118.

(60) Michelsen, H. A.; Rettner, C. T.; Auerbach, D. J. On the Influence of Surface Temperature on Adsorption and Desorption in the D_2/Cu(111) System. *Surface Science* **1992**, *272*, 65–72, DOI: 10.1016/0039-6028(92)91422-8.

(61) Hand, M.; Harris, J. Recoil Effects in Surface Dissociation. *The Journal of Chemical Physics* **1990**, *92*, 7610–7617, DOI: 10.1063/1.458198.

(62) Darling, G. R.; Holloway, S. Rotational Motion and the Dissociation of H_2 on Cu(111). *The Journal of Chemical Physics* **1994**, *101*, 3268–3281, DOI: 10.1063/1.467574.

(63) Dai, J.; Light, J. C. The Steric Effect in a Full Dimensional Quantum Dynamics Simulation for the Dissociative Adsorption of H_2 on Cu(111). *The Journal of Chemical Physics* **1998**, *108*, 7816–7820, DOI: 10.1063/1.476217.

(64) Díaz, C.; Olsen, R. A.; Auerbach, D. J.; Kroes, G. J. Six-dimensional dynamics study of reactive and non reactive scattering of H_2 from Cu(111) using a chemically accurate potential energy surface. *Physical Chemistry Chemical Physics* **2010**, *12*, 6499–6519, DOI: 10.1039/C001956A.

(65)   Marashdeh, A.; Casolo, S.; Sementa, L.; Zacharias, H.; Kroes, G.-J. Surface Temperature Effects on Dissociative Chemisorption of H2 on Cu(100). *The Journal of Physical Chemistry C* **2013**, *117*, 8851–8863, DOI: 10.1021/jp401311k.

(66)   Smeets, E. W. F.; Füchsel, G.; Kroes, G.-J. Quantum Dynamics of Dissociative Chemisorption of H_2 on the Stepped Cu(211) Surface. *The Journal of Physical Chemistry C* **2019**, *123*, 23049–23063, DOI: 10.1021/acs.jpcc.9b06539.

6

Samenvatting

Katalyse is een van de alomtegenwoordige processen van het leven, niet alleen in de levende cel, maar ook in de origine van de organische materialen die aan de grondslag staan van het leven. Ook in industriële processen is katalyse onontkoombaar, met toepassingen van olieraffinage en kunstmestproductie tot de waterstof-brandstofcel. Bij het katalyse-proces speelt de katalysator de hoofdrol. Dit deeltje verlaagt de energiebarrière van een chemische reactie zonder zelf verbruikt te worden. Hierdoor kan de katalysator bijvoorbeeld de afbraak bevorderen van gevaarlijke gassen, of zeer efficiënt twee moleculen aan elkaar koppelen. Als tijdens dit proces de katalysator zich in een andere aggregatie-toestand bevindt dan reactanten en de producten spreekt men van heterogene katalyse, één van de hoofdonderwerpen van dit proefschrift. Hoewel gekatalyseerde chemische reacties bestaan uit meerdere elementaire reactie-stappen is er meestal één stap snelheidsbepalend, vaak vanwege sterische of energetische barrières. Hierdoor ligt de focus bij optimalisatie van een katalyse-reactie vaak bij deze specifieke reactie-stap, door verbeteringen aan de katalysator zelf of de directe omgeving hiervan.

Bij industriële toepassingen bestaat de katalysator vaak uit een complex systeem van verschillende (metallische) oppervlakken en nanodeeltjes, geïntegreerd in een systeem van andere materialen. In het veld van de theoretische oppervlaktewetenschap, specifiek het veld van heterogene katalyse, probeert men deze reacties zo goed mogelijk te beschrijven met behulp van nauwkeurige modellen. Hierom moeten er veel simplificaties gebruikt worden om het systeem theoretisch te kunnen beschrijven, zoals statische oppervlakken en goed gedefinieerde facetten van de kristalstructuur van het metaal. Ook in dit proefschrift worden sommigen van deze simplificaties toegepast, door de dissociatie van individuele waterstof (H_2 of D_2) moleculen op een Cu(111) oppervlak te bestuderen. Het H_2/Cu(111) systeem wordt hier specifiek gekozen omdat het

een modelsysteem is voor de oppervlaktewetenschap, met een grote hoeveelheid experimentele en theoretische data beschikbaar.

Hoewel het algemene mechanisme van de dissociatie van H_2 op een (metaal)-oppervlak bekend is, zijn er ook nog veel open vragen omtrent selectiviteit, efficiëntie en optimale structuur van de katalysator. Om zo'n systeem computationeel efficiënt op te kunnen lossen wordt vaak gebruik gemaakt van de Born-Oppenheimer (BO) benadering. Bij deze benadering wordt aangenomen dat het elektronische en nucleaire deel van het systeem gescheiden opgelost kunnen worden, doordat de elektronen zich altijd onmiddellijk zullen aanpassen aan de bewegingen van de atoomkernen. Door eerst de elektronische energieën van het systeem te bepalen voor verschillende posities van de atoomkernen, kan het energielandschap, of het potentiële-energieoppervlak (PEO), dat de atoomkernen "voelen" in kaart gebracht worden. Hiermee kan men vervolgens, met behulp van klassieke of kwantumdynamica, de bewegingen van deze kernen over de tijd bestuderen. Door gebruik te maken van de BO benadering verwaarloost men niet-adiabatische effecten, waaronder de excitatie van elektronengatparen. Eerder onderzoek heeft aangetoond dat het effect van deze excitaties klein is voor het H_2/Cu(111) systeem, en dus zullen zij niet behandeld worden in dit proefschrift

In het veld van theoretische oppervlaktewetenschap wordt vaak gebruik gemaakt van dichtheidsfunctionaaltheorie (DFT) om de elektronische Schrödingervergelijking op te lossen, de eerste stap in de BO benadering. Bij DFT speelt de uitwisselingscorrelatiedichtsheidsfunctionaal (UC-DF) een belangrijke rol als het ontbrekende puzzelstuk in een verder exacte beschrijving van de elektronische energieën van het systeem. Hoewel er veel verschillende technieken zijn om de beste beschrijving te krijgen van deze onbekende, exacte DF, wil ik vooral aandacht besteden aan de specifieke-reactieparameter (SRP) benadering. Bij deze semi-empirische benadering wordt er een nieuwe UC-DF geconstrueerd uit een lineaire combinatie van twee verschillende UC-DFen, één die een gekozen experimentele waarde overschat en één die deze waarde onderschat, door de optimale fractie van elke DF te bepalen.

De BO benadering wordt in de praktijk vaak gecombineerd met de statische oppervlakte (SO) benadering, die samen bekend staan als de BOSO benadering. Door de oppervlakte-atoom posities vast te zetten in hun ideale kristalposities vermindert men significant de hoeveelheid vrijheidsgraden van het systeem. Daarentegen wordt de uitwisseling van energie tussen het (H_2) molecuul en het oppervlak ook verwaarloosd. Aangenomen wordt dus bij de SO benadering dat deze energie-uitwisseling minimaal is, door het grote verschil in massa tussen een waterstof- en een koperatoom, en door de de korte interactietijd tussen het molecuul en het oppervlak.

Het BOSO model kan verder verfijnd worden door de oppervlakte-atomen nog wel statisch te beschouwen maar niet meer in hun ideale posities te zetten. Deze verfijning ten opzichte van de SO benadering wordt ook wel de "abruptbenadering" genoemd, waar aangenomen wordt dat de interactie van het molecuul zo "abrupt" is dat de oppervlakte-atomen hier niet op kunnen reageren. Door te middelen over verschillende verstoorde, maar statische, oppervlakken kan men vervolgens toch nog het effect van een (relatief langzaam) bewegend, verstoord oppervlak bestuderen. Hierbij is het belangrijk dat de verdeling van oppervlakteverstoringen accuraat gekozen wordt, zodat het gemiddelde over de verzameling oppervlakken een goede representatie geeft van alle mogelijke situaties waarin het bewegende oppervlak zich zou kunnen bevinden. Deze verfijning ten opzichte van de reguliere BOSO benadering is in het verleden al meermaals succesvol toegepast, waaronder voor waterstof, koolmonoxide en methaan interacties met een (metaal)oppervlak.

Hoewel de oppervlakte-atomen altijd zullen bewegen door de nulpunts-energie, wordt de hoeveelheid kinetische energie in het oppervlak vooral hoger bij hogere oppervlaktetemperatuur. Daarnaast zal het oppervlak ook thermisch uitzetten bij een hogere temperatuur. Beide effecten verminderen de kwaliteit van de reguliere SO benadering, die aanneemt dat alle oppervlakte-atomen zich op hun ideale kristalposities bevinden. Eerder werk van Bonfanti *et al.* heeft al laten zien dat de verstoring van het oppervlak niet alleen invloed heeft op de hoogte van dissociatie-barrière van het waterstof, maar ook op de algemene vorm. Hierdoor zal oppervlaktetemperatuur dus niet alleen de reactiekans beïnvloeden, maar ook de verstrooiingskans en de rovibrationele eindtoestand na verstrooiing.

In dit proefschrift wordt de abruptbenadering gebruikt zoals geïmplementeerd in het statische corrugatie model (SCM). Met het SCM wordt het effect van de thermische verstoring van het metaaloppervlak beschreven door een additionele term in de potentiaal van het systeem, die gefit wordt aan DFT resultaten. Deze term beschrijft alléén de verandering van de potentiële energie van het systeem door deze oppervlakte-verstoringen en wordt beschreven door een simpele effectief drielichamenpotentiaal. Tot nu toe is het SCM alleen gebruikt om de dissociatie van waterstof op Cu(111) te beschrijven. Desalniettemin is de additionele koppelingsterm van het SCM generiek genoeg om ook gebruikt te worden voor de reactie van andere (twee-atomige) moleculen op een oppervlak, mits er nauwkeurige data beschikbaar is om de kromme naar te fitten. Als laatste heeft het SCM als invoer ook nauwkeurige beschrijvingen nodig van thermisch verstoorde oppervlakken.

In Hoofdstuk 3 worden twee verschillende methoden om deze thermisch verstoorde oppervlakken te genereren met elkaar vergeleken voor de dissociatie

van D_2 op Cu(111) op een quasi-klassiek dynamica (QKD) niveau. De ene methode maakt gebruikt van een willekeurige verdeling van de oppervlakte-atomen, gebaseerd op een temperatuur afhankelijke Debye-Waller factor, zoals in het originele SCM werd gebruikt. De andere methode maakt gebruik van klassieke dynamica en de ingebedde-atoom methode (IAM) om 25000 zeer nauwkeurige oppervlakken te genereren. Vervolgens worden QKD trajecten berekend op willekeurig geselecteerde of willekeurig gemaakte oppervlakten, afhanklijk van de gekozen methode. Beide methoden tonen duidelijke effecten van oppervlaktetemperatuur in de dissociatie- en verstrooiingskrommen vergeleken met de BOSO resultaten. Naast een klein verschil in de verzadigingswaarde, de maximale reactiekans die de reactiekromme voorspelt, tonen de twee methoden ook bijna identieke resultaten. Desalniettemin is er toch een significant verschil tussen de twee methoden als men naar de gemiddelde verplaatsing van de oppervlakte-atomen kijkt. Verder kan de IAM ook gebruikt worden om het oppervlak te laten bewegen tijdens de dissociatie-reactie, waardoor het effect van energie-uitwisseling met het oppervlak kan worden getoetst. Dit dynamische corrugatie model (DCM) toont weinig verschil met de resultaten verkregen met de statische oppervlakken van het SCM, wat suggereert dat de abruptbenadering van het SCM goed is.

Vervolgens wordt in Hoofdstuk 4 het IAM-SCM ook geïmplementeerd in een kwantumdynamica (KD) code gebaseerd op de tijdsafhankelijke golfpakketbenadering. Hierbij wordt het H_2/Cu(111) systeem bestudeerd, met de waterstof in de rovibrationele grondtoestand, waarbij de oppervlaktetemperatuur gesimuleerd wordt door te middelen over de resultaten van een verzameling van ongeveer 100 verstoorde oppervlakken. De dissociatie-kansen die verkregen worden met deze KD-IAM-SCM benadering komen goed overeen met QKD resultaten voor hetzelfde systeem. Daarentegen is er een duidelijk verschil tussen de twee methoden als men kijkt naar de rovibrationeel elastische verstrooiingskansen van het waterstof molecuul. Een meer zorgvuldige analyse laat zien dat vooral de niet-reactieve oppervlakken een significant verschil vertonen tussen de met KD en QKD verkregen verstrooiingskansen, terwijl er bij de zeer-reactieve oppervlakken weinig verschil is. Verder is het SCM ook toegepast door maar één, drie of vijf oppervlakte-atomen mee te nemen in het model (in plaats van de ∼70 van het volledige model). De goede overeenkomst tussen de dissociatiekansen verkegen met het volledige model, en met alleen de vijf dichtstbijzijnde oppervlakte-atomen toont hierbij dat het model al accuraat is met een kleine deelverzameling van oppervlakte-vrijheidsgraden.

Hoofdstuk 5 breidt deze KD resultaten uit door ook te kijken naar de initieel rovibrationeel aangeslagen toestanden. Verschillende manieren om de rovibrationele eindtoestand van de QKD resultaten te bepalen worden ook met

elkaar en met de KD resultaten vergeleken. Bij de ene methode worden alleen de toegestane rotationele transities meegenomen in het eindresultaat door de toepassing van gewichten voor elk traject. Daarentegen wordt bij het andere model altijd de dichtstbijzijnde toegestane eindtoestand gekozen. Allebei deze methoden, toegepast op de QKD simulaties, lijken ongeveer even goed de KD dissociatie- en verstrooiingskansen te voorspellen. Als laatste zijn ook de QKD en KD dissociatiekansen vergeleken met experimenteel verkregen waarden. Hier is vooral de overlap met de aanvang van de reactiekromme zeer goed, hoewel er ook significante ruis aanwezig is bij de zeer lage kansen van de KD resultaten.

Deze ruis in de KD resultaten is verder bestudeerd in Hoofdstuk 6, waar het effect met behulp van kortere propagatie-tijdstappen en door een alternatieve analyse methode sterk verminderd wordt. De dissociatie-krommen van het vorige hoofdstuk worden ook gefit aan verschillende functionele vormen. De parameters verkregen uit deze gefitte krommen vertonen over het algemeen een goede overeenkomst met die van dissociatieve adsorptie experimenten. Omdat deze experimentele resultaten origineel verkregen zijn als vluchttijdsspectra, worden de gefitte krommen van onze resultaten ook gebruikt om vluchttijdsspectra te simuleren. Dit staat een meer directe vergelijken met de experimenten toe, en laat zoals de eerdere analyses een goede overeenkomst zien met de experimenteel beschikbare resultaten. De doeltreffendheden van de rotationele en vibrationele moleculaire energieën voor het bevorderen van reactie in onze simulaties worden ook vergeleken met die verkregen uit experimenteel werk. Vooral voor de rotationele energie is hier een duidelijk verschil bij lage initiële toestanden, waar de theorie niet het experimenteel geobserveerde negatieve verband voorspelt tussen de rotationele energie en dissociatiekansen van het waterstof molecuul. Als laatste wordt er nog een vergelijking gemaakt tussen de rotationele quadrupooloriëntatieparameters (RQOPs) van de BOSO en SCM resultaten, verkregen met KD en QKD simulaties. Deze parameter geeft de voorkeur van het H_2 molecuul aan om te reageren met een orientatie parallel aan, of loodrecht op, het oppervlak. Voor de lage rotationele toestanden, waar KD resultaten beschikbaar zijn, lijken de KD resultaten hier een veel grotere voorkeur voor rotatie parallel aan het oppervlak aan te geven. Dit effect is geheel weg bij hogere rotationele toestanden, met een goede overlap tussen KD en QKD RQOPs. Wel voorspellen de SCM resultaten een iets kleinere voorkeur voor reactie met parallelle rotatie, die mogelijk verklaard kan worden door de verstoringen in het oppervlak.

In de toekomst zou verder werk met het SCM zich waarschijnlijk het best kunnen focussen op een uitbreiding naar andere systemen, beginnend met de reactie van waterstof op andere koperoppervlakken. Hiernaast zou verder onderzoek naar het genereren van correct verstoorde oppervlakken zeer nuttig

zijn om ook bij lage temperaturen, waar klassieke dynamica vaak faalt, het systeem goed te kunnen beschrijven. Dit zou dan toestaan om een betere directe vergelijking te maken met innoverende diffractie-experimenten waarbij de oppervlaktetemperatuur onder de "klassieke limiet" van 300 K valt. Ook zou de koppelingspotentiaal van het SCM gefit kunnen worden aan nauwkeurigere UC-DFen, waardoor het model hopelijk beter experimentele resultaten zal kunnen voorspellen.

Curriculum vitae

Bauke Smits is geboren op 2 februari 1994 te Zuidland. In 2012 heeft hij zijn gymnasiumdiploma behaald aan het Penta college Blaise Pascal te Spijkenisse.In ditzelfde jaar begon hij de bacheloropleiding "Molecular Science and Technology" aan de Universiteit Leiden en de Technische Universiteit Delft. Deze opleiding rondde hij af in 2015 met een onderzoeksproject onder begeleiding van dr. Mark Somers binnen de Theoretische Chemie groep van het "Leiden Institute of Chemistry", onderdeel van Leiden University. Hierbij is de invloed van de afkapafstand binnen het statische corrugatie model bestudeerd. Vervolgens ging hij verder met de masteropleiding "Chemistry" aan de Universiteit Leiden, waar hij onder begeleiding van dr. Hugo van Ingen zwakke koppeling tussen magnetisch inequivalente rotaties onderzocht. Na het behalen van zijn master-diploma in 2018, startte hij met zijn promotieonderzoek onder de promotor prof.dr. Geert-Jan Kroes met directe begeleiding van co-promotor dr. Mark Somers, wat uiteindelijk leidde tot dit proefschrift. Vanaf april 2023 zet hij zijn onderzoek naar temperatuurseffecten op de waterstof op koperreactie voort met een vervolgonderzoek onder begeleiding van dr. Jörg Meyer and dr. Mark Somers.

List of publications

- Wijzenbroek, M.; Klein, D. M.; Smits, B.; Somers, M. F.; Kroes, G.-J. Performance of a Non-Local van der Waals Density Functional on the Dissociation of H_2 on Metal Surfaces. *The Journal of Physical Chemistry A* **2015**, *119*, 12146–12158, DOI: 10.1021/acs.jpca.5b06008

- le Paige, U. B.; Smits, B.; 't Hart, P.; Lefeber, F.; Martin, N. I.; van Ingen, H. Weak Coupling between Magnetically Inequivalent Spins: The Deceptively Simple, Complicated Spectrum of a 13C-labeled Trimethylated Amine. *Journal of Magnetic Resonance* **2017**, *278*, 96–103, DOI: 10.1016/j.jmr.2017.03.016

- Smits, B.; Somers, M. F. Beyond the static corrugation model: Dynamic surfaces with the embedded atom method. *The Journal of Chemical Physics* **2021**, *154*, 074710, DOI: 10.1063/5.0036611

- Smits, B.; Litjens, L. G. B.; Somers, M. F. Accurate Description of the Quantum Dynamical Surface Temperature Effects on the Dissociative Chemisorption of H_2 from Cu(111). *The Journal of Chemical Physics* **2022**, *156*, 214706, DOI: 10.1063/5.0094985

- Smits, B.; Somers, M. F. The Quantum Dynamics of H_2 on Cu(111) at a Surface Temperature of 925 K: Comparing State-of-the-Art Theory to State-of-the-Art Experiments. *The Journal of Chemical Physics* **2022**, *157*, 134704, DOI: 10.1063/5.0112036

- Smits, B.; Somers, M. F. The Quantum Dynamics of H_2 on Cu(111) at a Surface Temperature of 925 K: Comparing State-of-the-Art Theory to State-of-the-Art Experiments 2. *The Journal of Chemical Physics* **2023**, *158*, 014704, DOI: 10.1063/5.0134817

Afterword

With this I now write the final parts of this thesis, which was most of all dominated by what the Dutch liked to call "lastige tijden". Nevertheless with some delay it formed into a full story about one very specific effect for one very specific system, which hopefully will at some point see an expansion to more general use. With the major risk of forgetting a lot of people, I will still try to at least say my thanks.

First of all, of course, to Mark Somers who snagged me from my Master's defence into this project. You provided the basis of this project with a clear goal and path to get there, yet left enough open for me to pursue my own approaches. Furthermore, under your guidance I got to learn the basics of both managing our HPC hardware and finding the best bars.

I am grateful for the scientific support and guidance of my promotor Geert-Jan Kroes. My thanks also to my desk-neighbour Marc van Hemert, who could always supply another point of view to any encountered problem, as well as Jörg Meyer, who has given me the opportunity to continue working on this system just a little longer.

Thanks also go out to Leandra Litjens and Ruard van Workum, the bachelor students I had the pleasure to supervise during this project. Not to be forgotten is then of course my only master student, and now colleague, Robert van Bree. Your master's project was a bit of a rocky journey, but that has never stopped you complaining about especially the little things.

I would be amiss to not also thank the PhD students who showed me the ropes: Paul Spiering, Guido Smeets, and Nick Gerrits. My thanks also go to Theophile Tchakoua, the fellow PhD student who might have started slightly before me, but taught me all about both unique types of food and paying at bars.

A further thanks for the people who are part of theoretical chemistry now, or in the past, who made the coffee breaks a lively place: Lukas Hückmann, Brian Ferrari, Floris van den Bosch, Marten Raaphorst, Tim Jansen, Justina Moss, Joan Enrique Romero, Jonathon Cottom, Andrew Powell, Seenivasan Hariharan, Khosrow Shakouri, Helen Chadwick, Katharina Doblhoff-Dier, Thanja Lamberts, Michelle van der Haar, Soroush Rasti, Sayan Seal, Hossein Tahmasbi, and Elham Nour Ghassemi.

Thanks to the boys from the Blaise Pascal, Floyd, Pepijn, Robert, and Laurens, we might have taken different routes in life but there will always be something that connects us. A thank you to my British friend "Pepi", for our love for a very specific news broadcast. And of course a thank you to Desiree, who allows me to try out many of the co-op games I find.

Finally, as always, the biggest of thanks to my family and grandparents, who would always try to understand my work, even if I myself didn't.